THESIS

ASSESSING THE IMPACTS OF MICROPHYSICAL AND ENVIRONMENTAL CONTROLS ON SIMULATED SUPERCELL STORMS

Submitted by

Sean William Freeman

Department of Atmospheric Science

In partial fulfillment of the requirements

For the Degree of Master of Science

Colorado State University

Fort Collins, Colorado

Fall 2018

Master's Committee:

Advisor: Susan C. van den Heever

Kristen L. Rasmussen
Richard Eykholt

ABSTRACT

ASSESSING THE IMPACTS OF MICROPHYSICAL AND ENVIRONMENTAL CONTROLS ON SIMULATED SUPERCELL STORMS

Supercell thunderstorms are some of the most dangerous single-cell storms on the planet. These storms produce many hazards to life and property, including tornadoes, floods, damaging straightline winds, strong updrafts and downdrafts, and lightning. Although these hazards are not unique to supercells, some of them are often at their strongest when supercell-produced. Because of the destructive power of supercell hazards, supercells have been the subject of scientific research for decades. In this thesis, two of these hazards will be examined: supercell rainfall and supercell tornadoes, with the overarching goal to improve both our process-level understanding and forecasts of these hazards.

The first part of this study focuses on supercell rainfall forecasts. Rainfall prediction by weather forecasting models, including supercell rainfall prediction, is strongly dependent on the microphysical parameterization being utilized in the model. As forecasting models have become more advanced, they are more commonly using double moment bulk microphysical parameterizations, which typically predict the hydrometeor number concentration and mass mixing ratio. While these double moment schemes are more sophisticated and require fewer *a priori* parameters than single moment parameterizations, a number of parameter values must still be fixed for quantities that are not prognosed or diagnosed. Two such parameters, the width of the drop size distribution and the choice of liquid collection efficiencies, are examined in Chapter 2. Simulations of a supercell were performed in which the collection efficiency dataset

and the *a priori* width of the rain drop size distribution (DSD) were independently and simultaneously modified. Analysis of the results show that the *a priori* width of the DSD was a larger control on the total accumulated precipitation (a change of up to 130%) than the choice of the collection efficiency dataset used (a change of up to 10%). While the total precipitation difference when changing collision efficiency is relatively small, it does have a larger control on the warm rain process rates (including autoconversion and liquid accretion) than changing the rain DSD width does. The decrease in rainfall as the DSD width narrows is due to a combination of three main factors: (a) decreased rain production due to increased evaporation, (b) decreased rain production due to decreased ice melting, and (c) slower raindrop fall speeds which leads to longer residency times and changes in rain self-collection. The decreasing precipitation rate and accumulated precipitation with narrower DSD is consistent with observations of continental convection. This part of the study emphasizes that, in order to improve rainfall and flooding forecasts, the number of *a priori* parameters required by microphysical parameterizations should be reduced. Improvements in rainfall forecasts can be made immediately through the further development and implementation of triple-moment microphysical schemes, which do not require an *a priori* specified DSD width.

The second part of this study focuses on supercell tornado forecasts. Supercell-produced tornadoes make up a majority of the most violent tornadoes and result in 90% of tornado-related deaths. Improving lead times and reducing false alarm rates is therefore critical. However, this requires an enhanced understanding of the controls that environmental conditions have on supercell tornadogenesis as well as improved observational platforms that are able to better detect environments that can produce tornadic supercells in advance. Therefore, the goals of the research presented in Chapter 3 are to (1): understand the storm processes that change as

environmental conditions of supercells are perturbed and (2): determine how sensitive platforms, especially space based platforms, would need to be in order to distinguish between environments that can produce tornadic supercells from those that will produce nontornadic supercells. To address the goals, a suite of experiments were performed with a numerical model where the Convective Available Potential Energy (CAPE), Lifted Condensation Level (LCL), and low level wind shear are independently perturbed. The presented research shows that a platform with high accuracy in temperature and wind shear measurements can add value to supercell tornado forecasting. Further, several processes that influenced tornadogenesis, including cold pool strength and the role of horizontal vorticity, are found to have an impact on tornadogenesis. This part of the study emphasizes the need for new observational platforms that can more accurately observe environmental conditions in order to improve supercell tornado forecasting.

Overall, the research presented here highlights supercell flooding and tornado forecast improvements that can be made with forecasting models and observational systems. Careful selection of *a priori* parameters, such as the width of the rain DSD, or reducing the number of those parameters required by microphysical parameterizations could improve supercell rainfall forecasts, therefore improving flooding forecasts. Supercell tornado forecasts can be improved by the addition of accurate space-based observational platforms which can help to distinguish between tornadic and nontornadic environmental conditions.

ACKNOWLEDGEMENTS

I owe a debt of gratitude to many people who have helped me in the completion of this work. First, I would like to thank my advisor Dr. Susan van den Heever who gave me the opportunity to create this research. Her guidance and patience have been critical to the success of the projects presented in this thesis. Her continuing dedication to her students, including me, is evident to all of those around her. She has made me a better scientist, a better writer, and a better person. I am grateful that I have her as an advisor and mentor.

I am also grateful to my other master's committee members, Dr. Kristen Rasmussen and Dr. Richard Eykholt for their time, flexibility, insights on this work, and edits to this thesis. Dr. Adele Igel serves as a co-author on the work presented in Chapter 2. I greatly appreciate Dr. Igel's guidance and patience throughout the process of producing that study both in the early stages and as we prepared it for publication. Dr. Igel has been an excellent mentor to me, especially as I begun the graduate program at CSU. Dr. Peter Kalmus and Dr. Brian Kahn at the Jet Propulsion Laboratory serve as co-authors and collaborators on the work presented in Chapter 3. I appreciate their thoughts throughout this process and appreciate their contributions to the perturbation levels tested in that chapter.

Although none of the data collected in the field are used in this thesis, my time working on the CSU Convective Cloud Outflows and Updrafts Experiment (C^3LOUD-Ex) helped to define my time so far at CSU. I would like to thank Dr. van den Heever once again for not only inviting me to participate in this project, but also for elevating me to a position of leadership and allowing me to experiment with novel technologies for atmospheric observations. I would like to thank the entire C^3LOUD-Ex team, who were all responsible for the success of the campaign. Dr.

Leah Grant and Peter Marinescu, who held leadership positions inside the campaign, were incredibly important in the success of the field program. I thank them for their hard work on the campaign and appreciate their efforts to keep me sane during the long days and nights.

I would especially like to thank the entire van den Heever group, both past and present, for their helpful discussions and unwaivering support during this process. Special thanks to Aryeh Drager, Dr. Leah Grant, Peter Marinescu, and Stephen Saleeby for thinking through problems with me and always being willing to discuss topics inside and outside science with me.

My friends and family have been integral in my success, both leading up to this point and throughout the entire Master's. Thanks to Justin Whitaker, Alissa Williams, Minnie Park, Jennie Bukowski, Stacey Kawecki, Michelle Sauer, and Matt Davey, who have laughed with me, ranted with me, and have been there for me no matter what. Thanks especially to Anna Walter who has been my rock of sanity and caring for a decade. Thanks to my parents, Will and Lynn Freeman, have put up with me as I have chosen to move away from home more than they-or I- would have liked. My parents have been endlessly supportive, loving, and encouraging and I could not have written this thesis without them.

The research presented in this thesis was funded by an American Meteorological Society Graduate Fellowship, NASA Grant NNN12AA01C: 1536989, and the NSF Graduate Research Fellowship Program DGE-1321845. High-performance computing support from Yellowstone (ark:/85065/d7wd3xhc) was provided by NCAR's Computational and Information Systems Laboratory, sponsored by the National Science Foundation. Resources supporting this work were provided by the NASA High-End Computing (HEC) Program through the NASA Advanced Supercomputing (NAS) Division at Ames Research Center.

TABLE OF CONTENTS

CHAPTER 1 INTRODUCTION

1.1. A brief history of supercell thunderstorms

Thunderstorms have been investigated since the start of atmospheric research due to their impacts on civilization through strong winds, heavy rainfall, and hazards such as lightning and tornadoes. In the modern era, thunderstorm research began with the Thunderstorm Project, which was initiated quickly after World War II in response to a series of thunderstorm-related aviation accidents (Byers and Braham 1948). In the Thunderstorm Project, instrumented aircraft, rudimentary weather radars, and atmospheric sounding systems were deployed across central Florida in 1946 and central Ohio in 1947 to observe both tropical and mid-latitude thunderstorms. This was the first major field campaign in the modern era to comprehensively observe thunderstorms and ushered in the modern era of thunderstorm research.

While thunderstorms were acknowledged as a major area of research with the Thunderstorm Project, supercell thunderstorms (hereafter supercells), which can cause significant hazardous weather including tornadoes, severe hail, flash flooding, and strong straight line winds, were not defined separately from ordinary thunderstorms until later. The first use of the word “supercell” in regards to thunderstorms did not appear until 17 years after the Thunderstorm Project concluded and was defined primarily from its strong appearance on weather radar (Browning 1964).

In the years since the Browning (1964) publication, the atmospheric science community has worked to advance our understanding of supercells from both operations/forecasting and research perspectives due to their power, which is more destructive than ordinary thunderstorms. Several major field campaigns and operational improvements have enhanced our understanding

of supercells and the hazardous weather associated with them. These improvements include the deployment of the NeXt generation RADar (NEXRAD) system deployed across the United States, which allowed for high resolution doppler wind observations and enabled earlier warnings of tornadoes. Field campaigns that strongly enhanced our understanding of supercells include the 1994-1995 Verifications of the Origins of Rotation in Tornadoes EXperiment (VORTEX), which focused on supercell-spawned tornadoes, which account for 90% of the tornado-related deaths in the US (Brotzge et al. 2013).

1.2. Supercell Characteristics

Supercells are typically characterized as large, strong, isolated storm systems that are organized around a large rotating updraft, called a mesocyclone (Browning 1964; Davies-Jones 2015). Due to their large, fast updraft, supercells generally appear with a tall cumulonimbus cloud base, referred to as the convective region, and a thin, wide region of cirrus clouds attached to the main base which develop as the upward moving air reaches the stable tropopause, referred to as the anvil region. Above the main updraft, there may be an area of convective clouds protruding out of the anvil region, called an overshooting top. Figure 1.1 is a photograph from an astronaut aboard the International Space Station of a supercell over Chile which has all of these characteristics. Most prominent in this image is a large, flat anvil region with an overshooting top over the main updraft, created when the updraft is strong enough to penetrate the stable tropopause region. Below the anvil region, the convective region can be seen extending from above the surface in Figure 1.1.

When examining the dynamics of supercells, there are three major features of note: the forward flank downdraft, the rear flank downdraft, and the updraft, each indicating a region of descending or ascending vertical motion. Figure 1.2 shows a schematic from Lemon and

Doswell (1979) that indicates the location and size of these regions within the storm and indicates the typical appearance of supercells on radar. The two downdraft regions are primarily driven by rainfall evaporating and cooling the air, leading to sinking motion. Supercells have stronger updraft and downdraft velocities than ordinary thunderstorms and it is this that can lead to various hazards that impact people on the ground.

1.3. Supercell Hazards

Supercells produce many hazards that impact humanity, including tornadoes, heavy rainfall including floods, damaging straightline winds, strong updrafts and downdrafts, and lightning. These destructive hazards are a major reason why so much effort has been put into examining supercells. In this thesis, two of these hazards will be examined: heavy rainfall prediction in Chapter 2, and tornadoes and the environmental conditions that distinguish tornadic and nontornadic supercells in Chapter 3.

Forecasting flood events requires contributions from many disciplines, but all flood predictions must start with accurately forecasting rainfall. Although supercell thunderstorms have been dismissed as major contributors to flooding and they are not widely regarded as large rainfall producers, supercells have been shown to be either sole causes or contributory factors in some flood events, primarily flash flood events (Smith et al. 2001). Given that supercells can be cause flood events and the rainfall forecasts for these events are critical, it is useful to examine how sensitive supercell rainfall predicted by weather models is to various parameters. With the more predominant use in forecasting models of double-moment bulk microphysical schemes, it is critical to examine how sensitive the rainfall forecasts are to two *a priori* parameters needed for the use of double-moment schemes: the width of the drop size distribution and the collision efficiencies utilized in the simulations. Chapter 2 examines these two parameters and their

relative effects on rainfall forecasts in supercells and has been submitted to the *Quarterly Journal of the Royal Meteorological Society*.

The most iconic and destructive hazard that is produced by supercells are tornadoes. In fact, most of the strongest tornadoes (EF3+) in the United States are spawned by supercells (Markowski and Richardson 2009; Brotzge et al. 2013). Improving lead times of tornado warnings is critical to reducing deaths from tornadoes and further increases in warning lead time will need to come from better understanding of the environmental conditions that cause tornadic supercells to form (Markowski and Richardson 2009; Brotzge et al. 2013). In Chapter 3, the sensitivity that an observational platform would need to contribute to tornadic supercell forecasting is examined using a numerical weather model. Further, the processes that distinguish nontornadic and tornadic supercells and the processes that can change tornado strength are investigated in this chapter. Chapter 3 is being prepared for submission to *Monthly Weather Review*.

The meteorological hazards generated by supercellular thunderstorms are deadly and destructive. Chapters 2 and 3 collectively serve to augment our existing knowledge about these storms with a view to both improving the state of the science on supercells and to improving forecasts of their hazards.

1.4. Figures

Figure 1.1. Astronaut photograph of a strong convective thunderstorm over Chile which has many of the same features as a supercell, taken from the International Space Station. Image (NASA photo ID ISS015-E-27038) courtesy of the Earth Science and Remote Sensing Unit, NASA Johnson Space Center (https://eol.jsc.nasa.gov/).

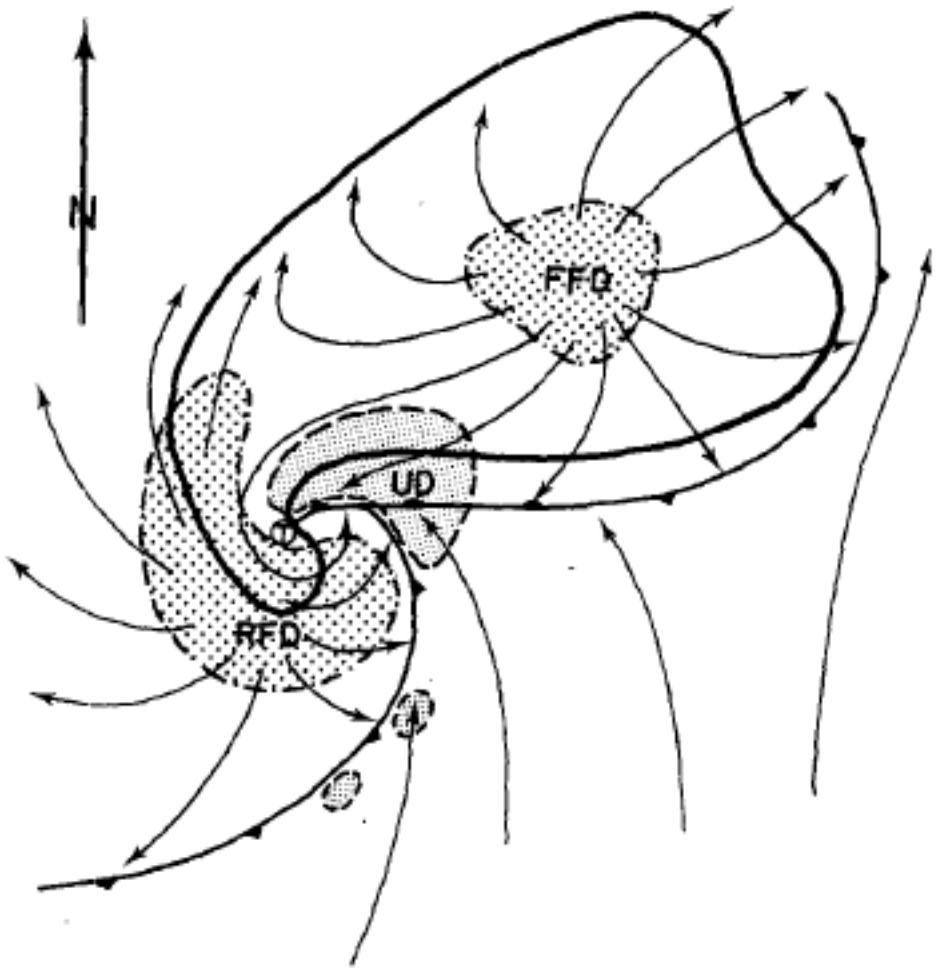

Figure 1.2. Schematic of a classic supercell thunderstorm from Lemon and Doswell (1979). The thick black line is emblematic of a radar echo, the two chevroned lines indicate outflow boundaries/gust fronts, the UD region is the updraft region, the FFD region denotes the forward flank downdraft, the RFD region indicates the rear flank downdraft, and the streamlines indicate surface wind direction.

CHAPTER 2: RELATIVE SENSITIVITIES OF RAINFALL PREDICTION IN SUPERCELL THUNDERSTORMS TO FIXED SHAPE PARAMETERS AND COLLECTION EFFICIENCIES

2.1. Introduction

Research and forecasting models cannot explicitly represent individual hydrometeors and their associated processes. Instead, they must use parameterizations to make bulk representations of hydrometeors and their effects on the dynamics and thermodynamics within each grid box of the model. Modeled precipitation has been shown to be highly sensitive to both the choice of microphysical parameterization and to the assumptions made within a single parameterization. Adams-Selin et al. (2012) found that changing the assumption about graupel and/or hail density within several microphysical parameterizations when simulating a mid-latitude squall line changed the peak storm total precipitation by up to 500%. Further, Igel et al. (2014) showed when examining single-moment microphysical parameterizations used to simulate both mid-latitude squall lines and within radiative convective equilibrium conditions, that total precipitation showed up to a 200% increase when changing the *a priori* parameters. This uncertainty in precipitation extends to tropical cyclones as well. For example, Brown et al. (2016) demonstrated that using different microphysics parameterizations in simulations of hurricanes changed total rainfall up to 110%. Many other studies have also found a strong variation in the precipitation predicted by models based on their broader choice of parameterization scheme (e.g. Grubišić et al. 2005; Morrison et al. 2009; Morrison and Milbrandt, 2010; Thompson et al. 2004; Varble et al. 2014) or to their more specific choice of parameters within a single scheme (e.g. Gilmore et al. 2004a; Thompson et al. 2004; van den

Heever and Cotton 2004; Morrison et al. 2009; Bryan and Morrison 2012). These results indicate that the sensitivity of rainfall to *a priori* specified parameters in the microphysical parameterization must be understood to improve forecasting of rainfall.

Within numerical models that are used for research and forecasting, the rate of change of the mass of cloud water and rain water (which are typically partitioned by drop size) can be generally represented using the following equations:

$$\frac{\partial q_c}{\partial t} = -ADV + \mathrm{DF} + \mathrm{CE} - \mathrm{AC} - \mathrm{LACR} + \mathrm{MLT} - \mathrm{IACR} - \mathrm{HFZ} \quad (2.1)$$

$$\frac{\partial q_r}{\partial t} = -ADV + \mathrm{DF} + \mathrm{CE} + \mathrm{AC} + \mathrm{LACR} + \mathrm{MLT} - \mathrm{IACR} - \mathrm{HFZ} \quad (2.2)$$

where q_c is the cloud water mixing ratio (g kg^{-1}), q_r is the rain water mixing ratio (g kg^{-1}), and the remaining terms represent the sources and sinks for liquid hydrometeors expressed as process rates (all g kg^{-1} s^{-1}): ADV is advection of drops from one grid cell to another, DF is diffusion of drops (source/sink), CE is condensation/evaporation (typically cloud source; rain sink), AC is autoconversion of cloud drops into rain drops (cloud sink; rain source), LACR is the accretion of cloud drops by rain drops (cloud sink; rain source), MLT is the melting of ice to liquid (source), IACR is accretion and riming of liquid by falling ice particles (sink), and HFZ is the loss of liquid hydrometeors due to homogenous or heterogeneous freezing (sink). Microphysical parameterizations need to make various assumptions in order calculate these processes. The sensitivity to two of these assumptions will be examined in this work: (1) the assumption about the width of the rain drop size distribution (DSD), which directly affects CE, LACR, and IACR; and (2) drop collision efficiencies which directly affects AC and LACR.

a. Rain drop size distribution

As described above, the assumptions made about the DSD of hydrometeors impacts many microphysics processes when modeling storms (e.g. van den Heever and Cotton 2004; Gilmore et al. 2004b; Milbrandt and Yau 2006; Ćurić et al. 2010; Igel and van den Heever 2017a). However, improvements and evaluations of hydrometeor DSDs, especially the representations of the rain DSD, have been restricted by the relatively infrequent and spatially limited nature of prior observational research. Most observational studies examining the rain DSD in a statistical sense have been conducted at the ground (e.g. Uijlenhoet et al. 2003; Niu et al. 2009; Friedrich et al. 2015), after raindrops have interacted with turbulent boundary layer air which may change the DSD through evaporation and droplet breakup. Some field campaigns have made in-cloud rain DSD observations with aircraft, but such observations have been limited in space and time and often only to particular cloud types (e.g. Yuter and Houze 1997; Freud et al. 2008; Heymsfield et al. 2015). Because of these limitations, it has been difficult to adequately constrain rain DSDs in microphysical parameterizations, in particular the rain DSD widths, to observations.

Although the observations of rain DSDs are spatially and temporally limited, we can still gain some insights into how best to represent their widths from those observations that are available. Niu et al. (2009) deployed a disdrometer in central China in summer 2007 to measure average precipitation rates and DSDs for both stratiform and convective liquid precipitation. They found that narrower rain DSDs were correlated with lower precipitation rates, and that DSD width was not fixed throughout storm lifetime. Cao et al. (2008) deployed three 2D Video Disdrometers (2DVDs) at the US Department of Energy Southern Great Plains site in northern Oklahoma from May 2005 to 2007 and derived a relationship between the slope of the rain DSD

and its width, but found that this relationship differs from a relationship observed in Florida by Zhang et al. (2001). Using a global dataset of disdrometer observations and principal component analysis, Dolan et al. (2018) found that rain DSD width varies with precipitation mode, including broader (narrower) distributions found in convective (stratiform) precipitation events. Further, Uijlenhoet et al. (2003), Bringi et al. (2009), and Friedrich et al. (2015) have all shown that rain DSD width can vary within a single storm. The observational evidence of rain DSD width, while limited mostly to near surface levels, suggests that fixing the rain DSD width *a priori* or using some empirical relationship to derive the rain DSD width when performing convective storm simulations (as all single and double-moment bulk microphysics parameterizations require) may produce results that do not compare favorably with observations either because the actual DSD width should vary with time or because the empirical function is not universal for all systems and locations.

The requirement that the rain DSD shape is fixed *a priori* exists partially because individual raindrops cannot be simulated using current cloud resolving models due to computational limits. Instead, either continuous probability distribution functions (PDFs) or binned DSDs, where drops are divided into discrete size bins (e.g. Khain et al. 2015), must be assumed to approximate the microphysical processes in the real atmosphere. One continuous distribution, the gamma PDF (the Marshall and Palmer (1948) exponential PDF is a special case of the gamma PDF), is widely used in bulk microphysical parameterizations to represent the size distributions of hydrometeor species (e.g. Walko et al. 1995; Milbrandt and Yau 2005a,b; Thompson et al. 2008; Morrison et al. 2009; Saleeby and van den Heever 2013). Its frequent use is due in part to the fact that this particular PDF has been shown to be a good approximation of

observed DSDs (Adirosi et al. 2015, 2016). Furthermore, moment-based characteristics are easily derived when using this size distribution function.

The complete gamma size distribution can be represented, within a single grid cell volume, as:

$$N(D) = N_T \frac{\lambda^{\nu}}{\Gamma(\nu)} D^{\nu-1} e^{-\lambda D} \tag{2.3}$$

where N is the number of drops at diameter D (# m^{-3} mm^{-1}), N_T is the total number concentration of drops in the grid volume (# m^{-3}), *f(D)* is the PDF (here defined as a gamma DSD; output of mm^{-1}), D is the droplet diameter (mm), Γ is the standard Euler gamma function (unitless), λ is the slope parameter (mm^{-1}), and ν is the size distribution shape parameter (unitless), which controls the DSD width when holding the slope parameter constant (which is equivalent to holding the mass mean diameter constant). When using this equation to represent a distribution of hydrometeors, there are three *a priori* unknown parameters: N_T, λ, and ν, where the latter parameter is one of the parameters of interest in this study. Expression 2.3 is just one form of the gamma distribution; however, it is equivalent to the other forms that appear in the literature. Figure 2.1 shows the impacts of changing ν while holding the mass mean diameter and total number concentration (and therefore the total mass) constant (at 1 mm and 10 cm^{-3}, respectively). Each DSD is labeled ν#, where # indicates the value of ν used in plotting each DSD. Higher values of ν result in a narrower DSD when holding the mass and number constant, and ν = 1 is equivalent to the Marshall and Palmer (1948) exponential PDF.

Bulk schemes are generally classified based on the number of moments of the continuous PDF that they predict. In single-moment microphysics schemes, the mixing ratio (third moment) is typically (although not necessarily) prognosed, with the total number, slope parameter, and shape parameter being either fixed or diagnosed using an empirical relationship from the mixing

ratio. As such, these schemes produce simulations whose solutions are sensitive to the method used to solve for the three unknowns for all hydrometeors (e.g. Gilmore et al. 2004b; van den Heever and Cotton 2004; Snook and Xue 2008). In contrast to single-moment parameterizations, double-moment parameterizations predict two moments of the distribution, typically the mixing ratio and number concentration, and use these moments to calculate the slope of the DSD and the total number concentration. However, these schemes still require a shape parameter to be specified *a priori*, and this parameter is then either kept constant throughout the simulation (e.g. Meyers et al., 1997), or alternatively may be diagnosed using thermodynamic properties or one of the other prognosed or diagnosed values of the PDF (Morrison et al. 2007; Thompson et al. 2008; Morrison and Milbrandt 2015).

Whereas single and double-moment schemes specify or diagnose the shape parameter, triple moment parameterizations allow for a varying shape parameter, and spectral bin microphysics schemes do not use a shape parameter at all (Ovtchinnikov and Kogan 2000; Rasmussen et al. 2002; Milbrandt and Yau 2005b; Lebo and Seinfeld 2011; Khain et al. 2015). However, these two approaches, particularly spectral bin microphysics, are too computationally intensive to run in operational settings. Double-moment microphysics schemes are increasingly being developed and/or used in operational forecasting cloud resolving models, such as in the COnsortium for Small scale MOdeling- Deutschland model run operationally by the German Deutscher Wetterdienst (COSMO-DE; Barthlott et al. 2017), the High Resolution Rapid Refresh model run operationally by the US National Oceanic and Atmospheric Administration (HRRR; Alexander et al., 2016), and the High Resolution Deterministic Prediction System run operationally by Environment and Climate Change Canada (HRDPS; Milbrandt et al., 2016). Because of the increasingly widespread use of double-moment schemes in operational numerical

modeling, the sensitivity of numerical simulations to the range of possible values that the shape parameter may be assigned *a priori* should be thoroughly examined, particularly for forecasting applications where such schemes are necessary to predict the characteristics of a wide range of cloud systems over extensive domains without prior knowledge as to what cloud systems will be formed. Furthermore, understanding the sensitivity of forecasting models to changes in the DSD width compared to other *a priori* parameters, like the selected collection efficiencies, can lead to a better understanding of forecasting model weaknesses and which factors to focus on improving.

The sensitivity to non-rain hydrometeor DSD widths has previously been examined, including Gonçalves et al. (2008) and Igel and van den Heever (2016) who examined the role of the cloud DSD width and Loftus et al. (2014) and Milbrandt and Yau (2005a) who investigated sensitivities to the hail shape parameter. Milbrandt and Yau (2005a) focused on the impact of the hail shape parameter choice on sedimentation and other processes in a one-dimensional model. While this simple framework is certainly useful for understanding basic process sensitivity, it neglects the storm-scale interactions that a full three-dimensional simulation environment provides. Furthermore, given their focus on hail rather than rain, Milbrandt and Yau (2005a) did not investigate the effects of droplet coalescence, which can be key to understanding the precipitation sensitivities in convective storms. This study aims to address this gap.

Sensitivities to rain DSD widths have already been addressed in part by Cohen and McCaul (2006), Seifert (2008), Wacker & Lüpkes (2009), Milbrandt & McTaggart-Cowan, (2010), and Naumann & Seifert (2016). Cohen & McCaul (2006) used a single-moment microphysics scheme and varied the shape parameters of many hydrometeor species simultaneously. Seifert (2008) used a single-column model to examine sensitivities of

evaporation of rain drops to rain DSD widths and proposed a new parameterization changing the rain DSD width as a function of the mean volume diameter. Wacker and Lüpkes (2009) and Milbrandt and McTaggart-Cowan (2010) focused on drop sedimentation sensitivity to rain DSD widths in a single-column model, while Naumann and Seifert (2016) examined warm rain processes only. However, none of these studies have examined the impact of the rain shape parameter in a three-dimensional fully interactive simulation with ice, or the relative importance of these changes in comparison to other critical microphysical specifications such as the collection efficiencies.

b. Collection Efficiency and Autoconversion Rates

While there are limited observations to validate rain DSDs, collection efficiencies and autoconversion rates (including here autoconversion of cloud and drizzle-sized droplets to rain droplets) have only been constrained by laboratory studies (e.g. Low & List 1982; Ochs and Beard 1984), theoretical models (e.g. Davis 1972; Jonas 1972; Klett and Davis 1973; Shafrir and Gal-Chen 1971), and direct numerical simulations (e.g. Ayala et al. 2008; Pinsky et al. 2008; Wang and Grabowski 2009). While collision efficiencies and autoconversion rates have not been directly observed, they have been demonstrated to be a source of uncertainty within microphysical parameterizations (e.g. Hsieh et al. 2009; Takuro and Toshihiko 2015).

In many of the current microphysical parameterizations that were originally based on Kessler (1969), autoconversion of cloud drops to rain drops is simply represented as some rate *A* such that:

$$A = \begin{cases} k_1[q_c - q_{c0}] & q_c > q_{c0} \\ 0 & otherwise \end{cases} \tag{2.4}$$

where A is the rate of cloud water mass conversion to rain (g kg^{-1} s^{-1}), k_1 is some specified rate constant (s^{-1} ; this cannot be directly observed), q_c is the initial amount of cloud water (g kg^{-1}),

and q_{c0} (g kg^{-1}) is some threshold value of cloud water mass above which autoconversion to rain water will occur (Kessler 1969; Liu and Daum 2004; see also microphysics schemes that use a version of this representation, e.g.: Lang et al. 2014; Morrison and Milbrandt 2010; Rogers et al. 2002) . While this is one way of representing autoconversion, some newer parameterizations use the full stochastic collection formulae and specified collection efficiencies to allow for more explicit modeling of self-collection of cloud droplets than the Kessler (1969) scheme allows (e.g. Feingold et al. 1988; Saleeby and Cotton 2004).

The collection efficiencies for various sizes and species of hydrometeors have been determined from theoretical, numerical, and laboratory experiments investigating these interactions between two droplets of various sizes. Generally, the collection efficiency of two droplets is defined as:

$$E(r_1, r_2) = E_{coll}(r_1, r_2)E_{coal}(r_1, r_2) \tag{2.5}$$

where E is the collection efficiency, r_1 is the radius of the collector drop (μm), r_2 is the radius of the collected drop (μm), E_{coll} is the collision efficiency, and E_{coal} is the coalescence efficiency. In many collection efficiency datasets, E_{coal} is set to unity, such that $E(r_1, r_2) = E_{coll}(r_1, r_2)$ (e.g. Hall 1980; Long 1974; Pinsky et al. 2001). However, this is not strictly a good assumption as (Beard and Ochs 1984) demonstrated through empirical tests that coalescence efficiency decreased below 100% for collector drop radii > 50 μm.

Two prominent gravitational collection (i.e. without turbulence impacts) efficiency datasets used in current microphysical parameterizations (e.g. Morrison and Milbrandt 2010; Saleeby and Cotton 2008; Seifert and Beheng 2001; Thompson et al. 2008) are the Hall (1980) (hereafter Hall80) and the Long (1974) (hereafter Long74) efficiencies. The Hall80 efficiency dataset is based on the collection efficiencies from several numerical and theoretical studies at

various drop sizes, and is highly discretized in its design (Davis 1972; Klett and Davis 1973; Shafrir and Gal-Chen 1971; Lin and Lee 1975; Schlamp et al. 1976; Jonas 1972). On the other hand, Long74 used similar theoretical and numerical studies (Shafrir and Gal-Chen 1971; Klett and Davis 1973), but instead of leaving the data in a discretized form, fit polynomials to the data and postulated that the collection efficiency is best described as those fit polynomials.

While the Hall80 and Long74 efficiencies are widely used, neither approach includes the effects of turbulence or of changing Reynolds numbers. Recent efforts, including (Ayala et al. 2008; Pinsky et al. 2008; Pinsky et al. 2001 [hereafter Pinsky01]; Xue et al. 2008) have demonstrated that collision efficiencies are substantially impacted by turbulence and changing Reynolds numbers, especially collision efficiencies between drops near cloud and drizzle size (i.e. $r \leq 100\mu m$). Figure 2.2 shows the collision efficiencies for four different droplet sizes ($r = 10, 25, 50,$ and 100 μm) for four different collision efficiency datasets: the Long74, Hall80, Pinsky01 (which includes effects from changing Reynolds numbers and are displayed as curves at three pressure levels), and Wang and Grabowski (2009; hereafter Wang09; which includes effects from turbulence at two levels). The different characteristics of the datasets are quickly apparent from this figure. While Long74's approach produces the smoothest collision efficiency function over most radii due to its fitted polynomial, it has two problematic ranges in drop size. First, the collision efficiencies when $r > 50\ \mu m$ are set to unity, creating a discontinuity in the collision efficiency function as the fitted function does not necessarily approach unity at $r = 50\ \mu m$. Second, when the collected drop $r < 3\ \mu m$, the fitted function values are less than 0 (in this case, those values are not plotted). The Wang09 efficiencies (with curves for turbulent dissipation rates of $\epsilon = 100$ and $400\ cm^2 s^{-3}$), which are calculated here by multiplying the turbulent enhancement factor (which ranges from 1 to 36.52) by the collision efficiency given by

the Hall80 efficiencies, produces a generally higher collision efficiency than the gravitational efficiency datasets (except for Long74 whenever $r > 50\ \mu m$ as described above) as would be expected when including the effects of turbulence. The Pinsky01 curves (denoted P01 for 1000 hPa, 750 hPa, and 500 hPa) produce similar results to the Hall80 and Wang09 efficiency datasets, with slightly smaller efficiencies in most cases. The largest differences between datasets arise when two drops of nearly the same size collide, with the Hall80 and Wang09 efficiencies showing a significantly larger collision efficiency than the other approaches, even reaching values much larger than 1 at certain radii. However, the likelihood that two drops of nearly the same size will collide in a gravitational collision kernel is near zero as their fall speeds are nearly identical, so this change is unlikely to have a large impact on model outcomes unless the turbulent fall speeds are implemented.

The work presented here attempts to better enhance our understanding of the sensitivity of convective precipitation to changes in the shape parameter for raindrops, as well as to changes in the collection efficiencies used for all liquid species. As demonstrated above, examining the shape parameter in a fully 3D simulation including ice has not previously been done. Further, to the authors' knowledge, no study comparing the results of newer collection efficiency tables to older gravitational kernels have been conducted on a fully 3D simulation of a deep convective storm including ice. While switching to a triple-moment or spectral bin microphysical parameterization will remove the need for an *a priori* shape parameter, both of these approaches to parameterization still require defining collection efficiencies and a way to represent autoconversion (either through a fixed autoconversion rate similar to (Kessler 1969) or through a collection equation, which requires collision efficiencies). Enhancing our understanding as to whether constraining the collection kernel and / or removing the shape parameter reduces the

sensitivity of the final model solution will assist in guiding developers of research and forecasting models in determining whether to develop further constraints on DSD width or to continue to develop new collision efficiency datasets.

2.2 Materials and Methods

Twelve high-resolution numerical simulations are produced to investigate the impact that changing the rain shape parameter and changing the collection efficiencies have on the thermodynamic, microphysical properties, and total accumulated precipitation of a supercell. We used the open-source Regional Atmospheric Modeling System (RAMS) version 6.1.18 to simulate the supercell storms for this study (Cotton et al., 2003; Saleeby & van den Heever, 2013). RAMS is a nonhydrostatic mesoscale model that is frequently used to simulate deep convective storms (e.g. Barth et al. 2007; Federico et al. 2014; Gaudet and Cotton 2006; Grant and van den Heever 2014; Grasso 2000; Lerach et al. 2008; Nair et al. 2013). The model was initialized using a horizontally homogeneous thermodynamic vertical profile (Figure 2.3) adapted from Gaudet et al. (2006). This sounding was selected because it produces simulations that quickly give rise to a vigorous supercell storm. The simulations were run for 150 minutes and analyzed for 130 minutes, which included the developing, mature, and dissipating phases of the supercell. For the analysis in this work, these phases are defined as follows: the developing phase of the storm is t=0 to t=38 minutes, ending at the onset of precipitation; the mature phase is defined is t=38 to t=120 minutes; and the dissipating phase starts at t=120 minutes. The dissipating phase begins at the point where the maximum updraft of the main storm is constantly decreasing and ceases when the maximum updraft of the main storm at 5 km reaches 30 m s^{-1} or lower (t=130 minutes).

The RAMS bin-emulating double-moment bulk microphysics parameterization was utilized for these simulations (Meyers et al. 1997; Saleeby and Cotton 2004; Saleeby and van den Heever 2013). This parameterization prognoses both mass and number concentration of eight hydrometeor categories: cloud water ($1.5 < r < 25\ \mu m$), drizzle ($25 < r < 50\ \mu m$), rain ($r > 50 \mu m$), pristine ice, snow, aggregates, graupel, and hail. A gamma DSD is assumed for all hydrometeor types. Sedimentation, autoconversion of cloud droplets to rain, and collection of cloud droplets by all other hydrometeor species are parameterized through the use of look-up tables representing the collection kernel described in (Tzivion et al. 1987). These tables are built from bin scheme representations of these processes that allow for drops of different sizes within a distribution to fall at different rates and to have size-dependent collection efficiencies using an *a priori* collection efficiency table (Saleeby and Cotton 2008; Feingold et al. 1998). Additionally, the RAMS parameterization outputs include detailed microphysical process rates, which are crucial to understanding the physical effects of changing the rain shape parameter.

In this work, we will test the use of four collection efficiency datasets: Hall80, Long74, Pinsky01, and Wang09 (Figure 2.2). While the Hall80, Pinsky01, and Long74 tables are gravitational efficiency datasets and do not include the effects of turbulence, the Wang09 kernel does include this effect at two levels of turbulence: $\epsilon = 100 cm^2 s^{-3}$ and $\epsilon = 400 cm^2 s^{-3}$, where ϵ is the mean viscous dissipation rate of the turbulence, and $\epsilon = 400 cm^2 s^{-3}$ is the more turbulent case. The Wang09 efficiencies are presented as an enhancement factor over gravitational efficiencies, and so for this work, the Wang09 efficiencies are the result of multiplying those efficiencies by the Hall80 efficiencies. In the remainder of this chapter, the Wang09 dataset will mean the Wang09 factors at $\epsilon = 400 cm^2 s^{-3}$ that are multiplied by the Hall80 efficiencies. Note that Wang09 includes both changes to the fall speeds and to the

collision efficiencies, but this work uses the enhancement to the efficiencies only. The implementation details of the collection efficiency datasets in RAMS are further described in Section 2.2a.

The model setup and homogeneous environmental thermodynamics of all twelve runs were identical, as described in Table 1. Six of the runs used the Long74 collection efficiencies and changed the rain shape parameter value only, using ν = 1, 2, 3, 4, 10, and 15, where ν = 1 is the same as the exponential Marshall-Palmer DSD (Marshall and Palmer 1948). This range in values was selected to provide a thorough evaluation of previously observed shape parameters in convective storms (Niu et al., 2009; Uijlenhoet et al., 2003). The simulation where ν = 15 is omitted from the results presented below as it was nearly identical to the results obtained using ν = 10. Six runs used the Hall80, Pinsky01, or Wang09 collection efficiency datasets holding a constant ν. All of these experiments are summarized in Table 2.2, which indicates the names used for all simulations presented in this work. These two shape parameters were chosen as they represent the broadest and narrowest rain DSD analyzed with the exception of the exponential Marshall-Palmer DSD. The shape parameter for cloud droplets and drizzle was set at ν = 3, and the shape parameter for all frozen hydrometeor species was set at ν = 2. These appear to be reasonable values for each species (e.g. Cohard & Pinty, 2000; Igel & van den Heever, 2017b; Lim & Hong, 2009). All six of the varying shape parameter runs were completed using the Long74 efficiencies for collision-coalescence and autoconversion. For the remainder of this work, the Long74 simulations will be designated Longν#, the Hall80 simulations will be designated Hallν#, the Pinsky01 simulations will be designated Pinskyν#, and the Wang09 simulations will be designated Wangν#, where # is the value of ν for rain in all cases.

a. Description of Collection Efficiency Dataset Implementation

None of the collection efficiency datasets were trivial to implement over all sizes in the bin-emulating component of RAMS (which range from r ≈ 1μm to r ≈ 6mm), as the Hall80, Pinsky01, and Wang09 efficiencies are tables of discrete values that do not strictly match up to the bins in the RAMS bin-emulating scheme and the Long74 dataset has negative values below r ≈ 5μm. For the Long74 dataset, all values for collection efficiencies below 0 were set to exactly 0. The Hall80 table contains 11 radii between 10 μm and 300 μm and 20 ratios of smaller drop radii to larger drop radii. Instead of discretizing on ratio, the Pinsky01 efficiency dataset has table values for each radius, producing a table of 61x61 radii between 1 μm and 250 μm. To resolve the issue of non-discrete values and values that do not encompass the entire spectrum, the following steps were taken: (1) to obtain the collision efficiencies between two drops of arbitrary radius *r1* and *r2*, the efficiencies were linearly interpolated between the provided discrete values; (2) as the radius of the collector drop (i.e. the larger drop) $r_1 \to 0$, $E \to 0$ linearly from the smallest radius available, where E is the collection efficiency; and (3) for the Hall80 and Wang09 datasets, which use radius ratio, as $\frac{r_2}{r_1} \to 0$, $E \to 0$ linearly from the smallest $\frac{r_2}{r_1}$ value available, where r_1 is the collector drop and r_2 is the collected drop. Additionally, for the Pinsky01 dataset only, as the dataset depends on pressure, the collection efficiency for an arbitrary point is linearly interpolated between the pressure values available (1000, 750, and 500 hPa). If the pressure is outside of the bounds of the given pressures, the efficiency was set to the value corresponding to the closest pressure with a value available. It should be noted that RAMS does not use these collision efficiency datasets for rain-rain collisions, instead opting to use a collision efficiency of unity for all rain self collection.

2.3. Results

The storm evolution can be seen by examining the accumulated precipitation from all simulations where $\upsilon = 2$ or $\upsilon = 10$ (Figure 2.4). All of the simulations produced a splitting supercellular thunderstorm; and further, all simulations result in similar storm development and precipitation patterns resemblant of a splitting supercell. Figure 2.4 further indicates that while the precipitation pattern appears to change with different collision efficiency datasets and holding υ constant, the total precipitation amount does not vary much. However, examining a single pair of collision efficiency dataset simulations, the total precipitation amount changes consequentially when moving from $\upsilon = 2$ to $\upsilon = 10$.

The greater sensitivity to the rain shape parameter is further confirmed by Figure 2.5 which shows the domain mean precipitation rate (mm min^{-1} km^{-2}) versus time (2.5a) and the total precipitation (kg) versus time (2.5b) for all $\upsilon = 2$ and $\upsilon = 10$ simulations. This figure demonstrates that the rain shape parameter exerts a much stronger control on the accumulated rainfall and rainfall rate than that exerted by any of the collection efficiencies investigated here. The differences in the precipitation processes with varying the collision efficiency dataset and holding DSD width constant will be examined in this section. A further examination of the changes to precipitation that occur with changing υ will be presented in Section 2.4.

Although the accumulated precipitation in all collision efficiency dataset simulations remains approximately the same (with a maximum percent change reaching 10% of total accumulated precipitation by the end of the simulation), the processes that result in the surface rainfall differ between the eight simulations. In order to examine the changes in the rain production processes, a detailed microphysical budget was prepared, showing every process within the model that creates or removes rain from the atmosphere, with the exception of

precipitation to the surface. This budget was compiled by vertically integrating each rain source and sink term and averaging them across the domain and at all times. In Figure 2.6, cloud collection (red dots) relates to cloud and drizzle collision-coalescence with rain and autoconversion of cloud and drizzle to rain; collision melting (orange dots) is defined as the melting of all ice species into rain through the collision of such ice species with rain; other melting (blue dots) is melting of ice into rain not including collision melting; ice accretion (green dots) is rain being accreted by ice; and condensation and evaporation (purple dots) are shown as the net of these two processes for rain only. Positive numbers indicate the creation or sources of rain, and negative numbers indicate the removal or sinks of rain. The cyan dots represent the sum of all processes.

Figure 2.6 indicates that while the total rain generated is more strongly controlled by the shape parameter than by the collision efficiencies (the sensitivity to shape parameter will be investigated further in Section 2.4), changing the collision efficiency dataset impacts the processes that lead to rain. In particular, collision efficiency dataset is the stronger control on cloud collection than the DSD width, with the Hall80 simulation producing materially less rain through autoconversion and cloud collection than any of the other efficiency approaches. In the following two paragraphs, we will separate the total difference in this term into its two components: autoconversion and the collection of cloud water by falling raindrops.

The changes to the autoconversion and collection of cloud water by rain are not parsed out individually in the budget, however the changes to each of these can be inferred from examining the collision efficiency differences. Figure 2.2a shows that the collision efficiencies of a cloud droplet of $r = 10\mu m$ with rain drops of r ≥ 50μm for the Hall80, Wang09, and Pinsky01 tables are nearly the same and all lower than the Long74 dataset, which assigns all of the collision

efficiencies where the collector drop has $r \geq 50\mu m$ to unity. These lower collision efficiencies for the Hall80, Wang09, and Pinsky01 tables for rain-cloud and rain-drizzle collisions result in the lower collection of cloud mass by rain than when compared with the Long simulations for both $\upsilon = 2$ and $\upsilon = 10$.

While the Long74 dataset has the most cloud-to-rain conversion, the Hall80 dataset has the least, reaching below even the Wang09 and Pinsky01 datasets. This is primarily due to a decrease in autoconversion, rather than a decrease in cloud-rain collection. This is evident by examining Figure 2.2d, which shows the collision efficiencies for a collector drop of $r = 100\mu m$ and cloud and rain droplets of other sizes. For the regions of cloud and drizzle collection by rain (i.e. $r < 50\mu m$), the Wang09 dataset has the same collision efficiency as the Hall80 dataset and Pinsky01 is either below (for $r < 4\mu m$) or near the Hall80 dataset. This indicates that the predominant change between the Hall80 and other datasets when examining cloud collection is due to a change in autoconversion that is brought on by a change in collision efficiencies in the cloud-cloud, cloud-drizzle, and drizzle-drizzle regions.

While the cloud collection term in the budget changes between all four efficiency tables, the total amount of precipitation generated, as well as the total amount that reaches the ground, stays approximately constant. This is due to the near-complete offsetting of reduced cloud collection and autoconversion by the reduced loss of rain to accretion by ice. This offsetting occurs due to the fact that there is less rain mass and therefore less available to be accreted by ice. Overall, while the processes that produce rain differ somewhat between the different collection efficiency tests, the shape parameter is a much stronger control on the rain processes and total rainfall amount than the collection efficiencies for these idealized deep convective simulations tests.

2.4. Shape Parameter Results

Figures 2.5 and 2.6 indicate that when $\nu = 10$, the total accumulated rainfall decreases substantially when compared to $\nu = 2$. To examine whether this is an aberration unique to the difference between the $\nu = 2$ and $\nu = 10$ simulations or a larger effect of the narrowing DSD, additional simulations were conducted with $\nu = 1$, 3, and 4 using the Long74 Efficiency dataset (the default collection efficiency dataset in RAMS).

To examine overall precipitation differences resulting from the utilization of different shape parameters, the 5-minute running mean of the grid-averaged precipitation rate for all Long74 simulations is shown in Figure 2.7a and the domain total accumulated precipitation over time is shown in Figure 2.7b. It can be clearly seen that throughout the developing, mature, and dissipating phases of the storm, the rainfall rate increases monotonically as the rain DSD widens (i.e., as the shape parameter decreases), producing a nearly 130% difference in final accumulated rain amount. This trend of increasing rain with wider DSD is consistent with the prior observations made by Niu et al. (2009) discussed above.

Furthermore, the rain DSD impacts the vertical profiles of rain mass and number. It is evident that as the rain DSD narrows, the raindrop mass mean diameter at heights less than ~4000 m also generally decreases (Figure 2.7c). Above 4000 m, this trend reverses due to changes in rain self-collection (discussed in Section 2.4b). A similar reversal at ~5000 m occurs in the mixing ratio, switching from narrower DSDs having larger mixing ratios above 5000m to narrower DSDs generally having smaller ratios below 5000m (Figure 2.7e), although the reversal is not as abrupt. Figure 2.7d shows that the raindrop number concentration generally increases with narrowing DSD at heights below 4500 m and decreases with narrowing DSD above that height. The DSD induced impacts on the vertical profiles of rain mass and number

concentrations produce a decrease in rain rates, and therefore also in accumulated precipitation. It appears that these impacts are caused by three predominant factors: (1) a decrease in the net rain mass production, (2) a decrease in the mean raindrop diameter and fall speed (and thus an increase of rain mixing ratio remaining in the atmosphere), and (3) changes in the ice processes as the rain DSD becomes narrower. The processes driving these factors are now examined in more detail.

a. Change in rain mass production from evaporation

In order to examine the changes in the rain mass production, a detailed microphysical budget was prepared as in Figure 2.6, showing every process within the model that creates or removes rain from the atmosphere, with the exception of precipitation to the surface. The budgets for the six Long74 simulations are shown in Figure 2.8a. It is evident from this figure that there is a monotonic decrease in the net rain production as the rain DSD narrows (as the shape parameter increases). This monotonic decrease is driven by increased evaporation (purple dots) and decreased rainfall production from collision melting (orange dots) that is not entirely offset by changes to all other melting (blue dots).

To understand why the evaporation of rain increases as the distribution narrows, it is useful to examine the condensation/evaporation equation. In this section, evaporation will be the focus, as there is more evaporation than condensation as seen in Figure 2.8a (indicated by the negative values for the Condensation and Evaporation term). When integrated over a gamma PDF, evaporation is proportional to ν even when holding number and mixing ratio constant through the following relationship:

$$\left.\frac{\partial q_r}{\partial t}\right|_{evap} \propto NM_1(S-1) = N\bar{D}\nu\left[\frac{\Gamma(\nu)}{\Gamma(\nu+3)}\right]^{\frac{1}{3}}(S-1) \tag{2.6}$$

where $\left.\frac{\partial q_r}{\partial t}\right|_{evap}$ is the local time rate of change in rain mass mixing ratio due to evaporation (kg kg^{-1} s^{-1}), N is the number concentration of raindrops (# m^{-3}), M_1 is the first moment of the DSD (mm), and $\overline{D}$ is raindrop mass mean diameter (mm) (Igel and van den Heever 2017b).

According to expression (2.6), the evaporation rate of rain mass will increase as the first moment of the DSD increases, which partially depends on the term: $\left[\frac{\Gamma(\nu)}{\Gamma(\nu+3)}\right]^{\frac{1}{3}}$. Figure 2.8b shows the relationship between ν and this quantity to demonstrate that it is directly dependent on ν. The reasons for the dependence of the first moment of the DSD on ν are not necessarily intuitive. To understand why the first moment (proportional to the integrated diameter) increases with increasing ν when holding mass and number constant, it is helpful to consider the more general physical question of whether any moment I is increased or decreased due to a change in shape parameter when number and mass (zeroth and third moment, respectively) are held constant. Very high moments will increase as ν decreases (that is as the DSD becomes broader). This is because for small ν there are more very large drops than there are for large ν (see Figure 2.1). This means, for example, that the 1000th moment will depend primarily on only the large drops as a moment I is proportional to the integration of D^I over all diameters, and $D_{small}^{1000} \ll D_{large}^{1000}$. For lower and lower moments, the relative number of drops in the center and left tail of the distribution (where smaller drops reside) begin to have a greater impact in determining whether a moment increases or decreases with ν until eventually, they matter equally as much as the relative number in the right tail, when calculating the third moment. The third moment is held constant by design and does not depend on ν. For the first and second moments, the center of the distribution, where more drops reside in DSDs with higher ν, becomes the most important.

Therefore, these moments must increase for higher ν when the number and mass are specified to be constant.

In this discussion, it is helpful to note that the sedimentation process in RAMS is represented using bin-emulating techniques, which allows for differential fall speeds based on drop sizes. This is unlike many bulk schemes in which the fallspeed of the entire droplet distribution is the same and based on a mass-weighted average for the predicted mass and a number-weighted average for the predicted number. Beyond the contribution to the increased evaporation rate directly caused by the narrowing DSD when the number and mass are held constant as discussed above, there are additional factors that impact the evaporation rate, such as the actual changes to the droplet mean diameter and the number concentration. Raindrop populations comprised of more smaller raindrops are associated with enhanced evaporation rates (even though the actual magnitude of the evaporation rates are lower per droplet for smaller drops) because they fall more slowly than larger drops, thereby increasing their residence time below cloud base and subsequent exposure to dry air. As the narrower DSDs produce a raindrop population with lower mass mean diameters below cloud base, the rain within the higher ν sensitivity tests will therefore be subjected to more evaporation because of the lower fall speeds. Furthermore, for the same liquid water content, a population comprised of more numerous smaller drops as opposed to fewer but larger drops will have a larger exposed integrated surface area which will also enhance the amount of evaporation.

The changes to the evaporation result in changes in the cold pool as exhibited by changing temperatures at the surface. Figure 2.7f shows the maximum magnitude perturbation θ_ρ (where perturbation is defined relative to the initial homogeneous environment) at the surface over time throughout the storm lifetime. Here, the density potential temperature $\theta_\rho = \theta[1 +$

$0.61r - r_l]$ where r is the water vapor mixing ratio (kg kg^{-1}), θ is potential temperature (K), and r_l is the mixing ratio of liquid water in the air (kg kg^{-1}). While Figure 2.7f indicates a generally colder cold pool with narrower DSD, this change does not impact the size of the cold pools substantially nor the overall storm structure.

b. Changes in Rain Self-Collection

Changes to collision-coalescence that result in more rain residing in the cloud will now be discussed. In broader size distributions, such as when $\nu = 1$ or 2, the disparity in drop sizes leads to a wider range in the fall speeds of the raindrops than is found in narrower size distributions. This differential sedimentation results in an increasing amount of rain self-collection as the DSDs widen. This can be seen in Figure 2.8c, which is a vertical profile of rain self-collection averaged spatially and temporally. The increased rain self-collection leads to a larger mean drop size and fewer raindrops in the broader size distribution sensitivity tests. These larger drops more readily fall out of the cloud and produce a higher instantaneous precipitation rate. Therefore, the impacts of the shape parameter on both the rain water production and the rate at which raindrops fall to the surface contribute to the decrease in the precipitation rate and accumulated precipitation with increasing ν.

c. Change in rain mass production due to ice processes

In addition to the increased evaporation with narrower size distributions, net rain production is also reduced through a decrease in the amount of ice melted into rain through collisions (Figure 2.8a). This occurs due to the changes in collision-coalescence caused by the differences in fall speeds between rain and hail. Rain fall speed will increase as the DSD widens while the hail fall speed is not directly affected by the changes in rain DSD width. With wider distributions, many more collisions result between hail and rain due to the large spread in fall

speeds across the raindrop size spectrum. For narrower DSDs, more rain drops fall at similar rates and hence are less likely to collide with falling hail particles. This is reflected in the RAMS collision-coalescence equations (Walko et al. 1995).

While the production of rain through collision melting decreases dramatically in those simulations with narrow DSDs, there is a compensating effect in rain production through more non-contact melting (although not sufficiently more to counteract the decrease in contact melting). Increased non-contact melting is primarily caused by the larger mass fraction (compared to total hydrometeor mass) of ice in the narrower DSD cases, which results from the total cloud ice mass remaining approximately the same (Figure 2.9c) while the cloud liquid mass decreases with decreasing shape parameter. Along with impacting the surface rainfall, these changes in melting also have implications for hail production—especially in the higher shape parameter cases, as the increase in ice mass results in producing more hail at the surface. More accumulated hail with narrower DSD is shown in Figures 2.9a and 2.9b, which compare the spatial distribution of all ice precipitation accumulated by the end of the simulations in the Longν2 and Longν10 cases. The majority of the contribution to the increase in hail at the surface is caused by the lack of contact melting.

Figure 2.9d shows a spatial and temporal average vertical profile of hail (calculated over all columns containing integrated condensate >1 kg m^{-2}) for all of the sensitivity simulations. The figure indicates that even while the hail mass decreases below the melting layer, the fewer hail-rain collisions that occur in association with the narrower rain DSD results in a larger hail concentration well below the melting layer in the ν10 case. While none of the simulations produce large amounts of hail at the surface, the results suggest that the amount of hail at the

surface could be highly sensitive to the selection of the *a priori* rain drop shape parameter in model simulations using double-moment microphysics schemes.

2.5. Discussions and Conclusion

In this work we have examined the sensitivity of precipitation, process rates, and storm structure to changes in (1) the collection efficiencies and (2) the *a priori* assumed rain DSD width in three-dimensional, fully interactive idealized simulations of a deep convective storm. For the experiments where the DSD width is held constant and the collection efficiency dataset changes, the changes to the dataset used result in small changes to the overall precipitation (10%). While the total precipitation amounts do not vary strongly as a function of the different collection efficiency datasets, the precipitation processes that lead to rainfall do vary. The Hall80 efficiencies in particular produce less autoconversion than the Long74, Pinsky01, and Wang09 efficiency datasets.

For those experiments in which the collection efficiency dataset is held constant and the width of the DSD was varied using the shape parameter ν, as the DSD widens (ν decreases), the mean precipitation rate and total accumulated precipitation increase (total accumulated precipitation increases up to 130%). This occurs due to a combination of three main factors: (a) decreased rain production due to increased evaporation (Section 2.4a), (b) slower raindrop fall speeds leading to longer residency time and changes in rain self-collection (Section 2.4b), and (c) decreased rain production due to decreased ice melting (Section 2.4c). Wider DSDs also result in increased hail precipitation at the surface.

Our modeling results of a decrease in precipitation with narrowing DSD are similar to the trends obtained from limited observational results, including those of Niu et al. (2009). This

research indicates that care should be taken when selecting a shape parameter, especially for those situations that rely on the accurate prediction of precipitation, realistic microphysical budgets and reasonable representations of cold pools. This result is especially troubling for forecasting models which are expected to use a single *a priori* value or empirical function for the shape parameter to forecast a wide variety of convective storm types over a wide range of conditions. The results presented here also indicate that changing ν produces a wide spread in values of forecasted rainfall, and suggest that benefit may be gained in running an ensemble with varying values of υ to improve rainfall predictions.

The research presented in this chapter suggests that more effort should be put into removing the sensitivity of precipitation predictions to shape parameter rather than improving the collection kernels and their associated collection efficiencies for storms dominated by rain production from melting. While changing the shape parameter resulted in a much larger change to overall precipitation, the collision efficiency dataset used was a much stronger control on cloud collection (including autoconversion and cloud accreted by rain) than the DSD width. Further work should be done with warm clouds and mixed-phase clouds that are not as strongly dynamically driven to understand this sensitivity in more detail.

Issues with the shape parameter could be avoided completely with further development of microphysical parameterizations that do not rely on a specified *a priori* shape parameter. Some progress has been made through diagnosing size-shape parameter relationships (e.g. Cao et al. 2008), but this work has not been extensively validated with in-cloud observations or at a variety of locations. Some triple-moment schemes which prognose the shape parameter have been developed (e.g. Loftus and Cotton 2014; Milbrandt and Yau 2005), however, triple-moment schemes are rarely used in research or forecasting applications, with operational centers

especially opting for less time-consuming single or double moment schemes. Spectral bin microphysics schemes do not rely on an *a priori* assumed DSD, but their computational intensity restricts their use in research and currently prohibits their use in forecasting applications entirely.

This work should be expanded to include simulations of more types of convective storms and precipitating clouds using triple-moment schemes, spectral bin schemes, and various diagnosed size-shape relationships. Comparisons of these results with the double-moment results presented here would facilitate additional analysis of the shape parameters predicted by such parameterizations, as well as the sensitivity of various types of convective storms to changes in their shape parameter. As these new schemes are developed, their sensitivities to the collision efficiency dataset should be examined.

2.6. Tables and Figures

Table 2.1: Model Setup Information

Model Configuration	Setting
Grid	Δx=250m, 1000x800 grid points (250 km x 200 km); Δz=25m at the surface; stretched to 300m over 92 vertical levels at a stretch ratio of 1.1
Initial Conditions	Horizontally Homogenous initial sounding modified from (Gaudet et al. 2006), shown in Figure 3
Initialization	Horizontal convergence zone (Loftus, Weber, & Doswell, 2008; Schumacher, 2009); initiated as an oval in the southwestern portion of the grid, with short and long axis lengths of 10 km and 20 km, respectively and vertical length of 1.2 km. The convergence was linearly increased to a magnitude of 5×10^{-3} s^{-1} at 10 minutes, after which the momentum forcing was terminated.
Radiation	None
Microphysics	RAMS 2 moment bin-emulating bulk scheme (Saleeby and van den Heever 2013; Saleeby and Cotton 2004; Walko et al. 1995); described in the text.
Time	Simulations run for 2.5 hours; analyzed for 130 minutes only. Δt = 0.25s
Boundaries	Lateral boundaries: open radiative. Top boundary: Rayleigh friction absorbing layer in the top 1.8 km. Bottom boundary: free slip.

Table 2.2: The Experiments conducted in collection efficiencies (columns) and rain shape parameters (rows) along with the experiment name.

Rain Shape Parameter (ν)	Long74 Collection Efficiencies	Hall80 Collection Efficiencies	Pinsky01 Collection Efficiencies	Wang09 Collection Efficiencies
1	Longν1	n/a	n/a	n/a
2	Longν2	Hallν2	Pinskyν2	Wangν2
3	Longν3	n/a	n/a	n/a
4	Longν4	n/a	n/a	n/a
10	Longν10	Hallν10	Pinskyν10	Wangν10

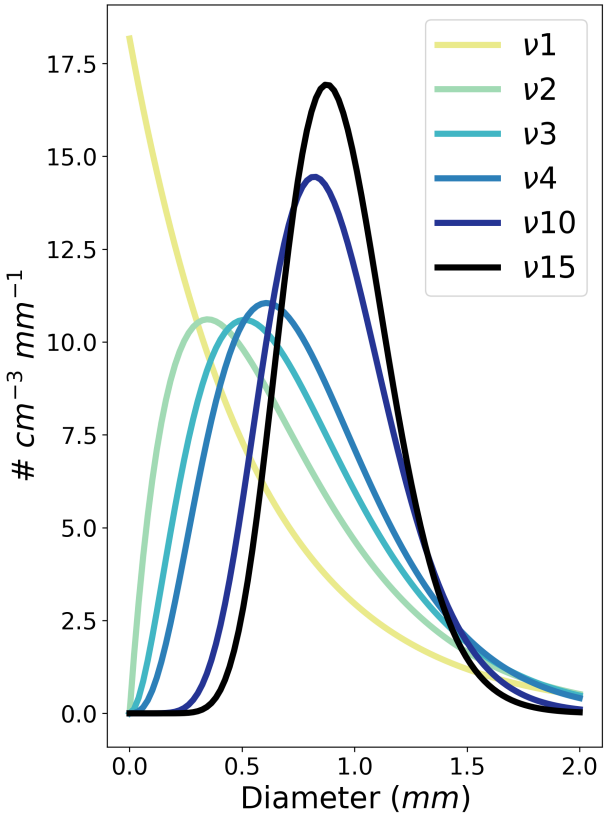

Figure 2.1: Initial rain DSDs for each of the sensitivity simulations conducted. All of the DSDs are represented by gamma distributions with a constant mass mean diameter of 1.0 mm and number concentration of 10 cc^{-1}. The lines are labeled *ν*#, where # is the value of the shape parameter shown by each line.

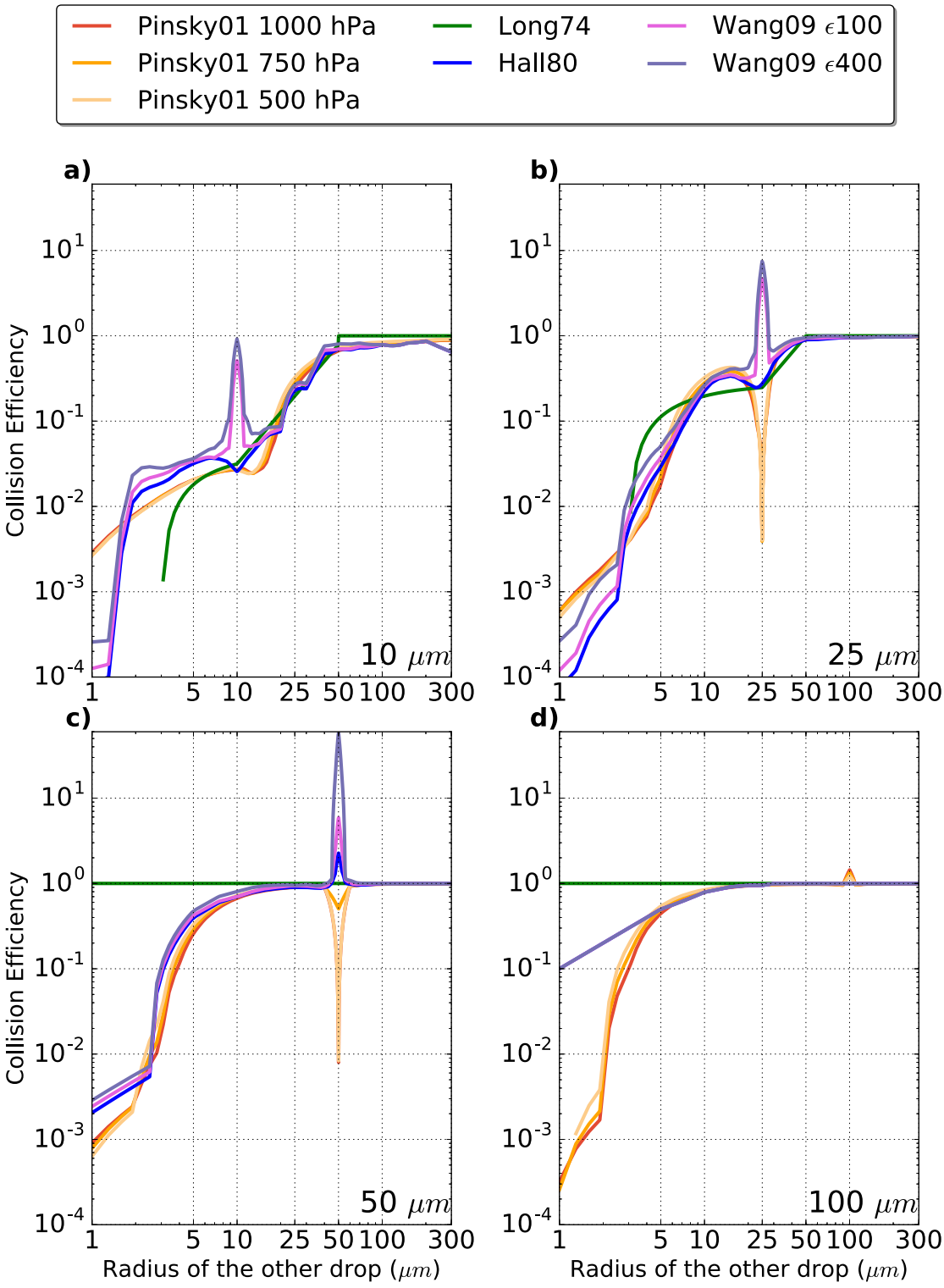

Figure 2.2: Collection efficiencies from Hall80, Long74, Pinsky01 at 1000, 750, and 500 hPa, and Wang09 at $\epsilon = 100\ and\ 400\ cm^2 s^{-3}$ for one drop of radii a) 10 μm, b) 25 μm, c) 50 μm, and d) 100 μm and another drop as described on the abscissa.

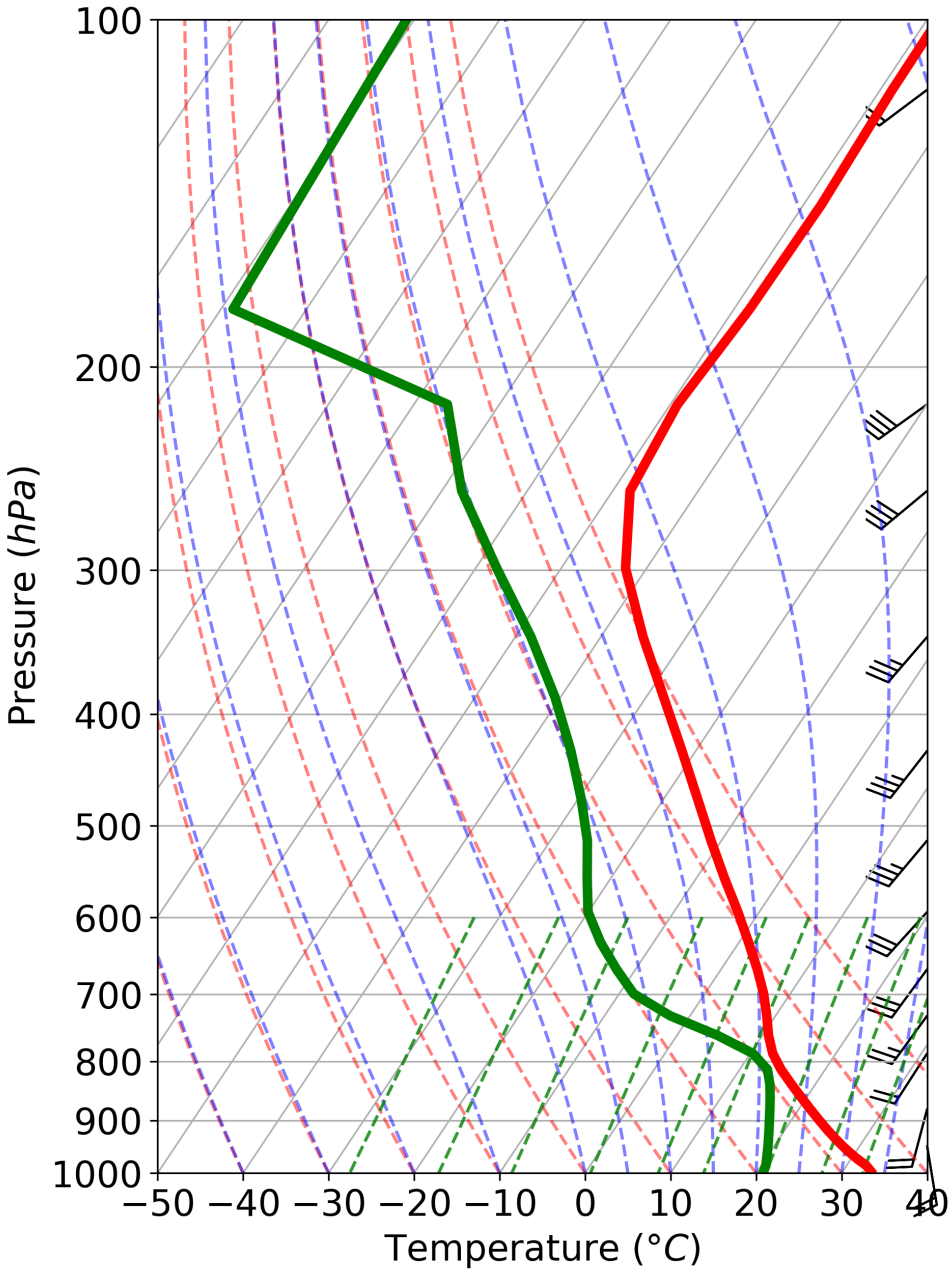

Figure 2.3: The sounding (adapted from (Gaudet et al. 2006)) used for the horizontally homogenous initialization for the model in all simulations. The red line denotes temperature (°C) and the green line denotes dew point (°C).

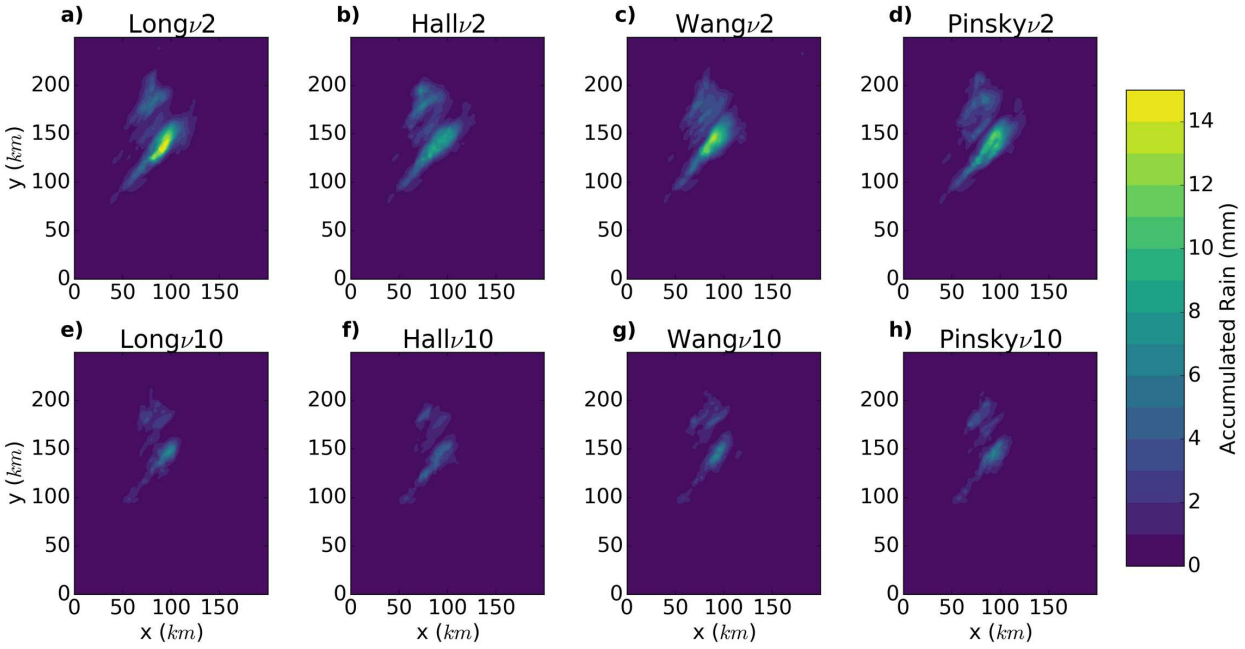

Figure 2.4: Surface accumulated rainfall (mm, shaded) after 130 minutes for all eight simulations where $\nu = 2$ (top; a-d) and $\nu = 10$ (bottom; e-h).

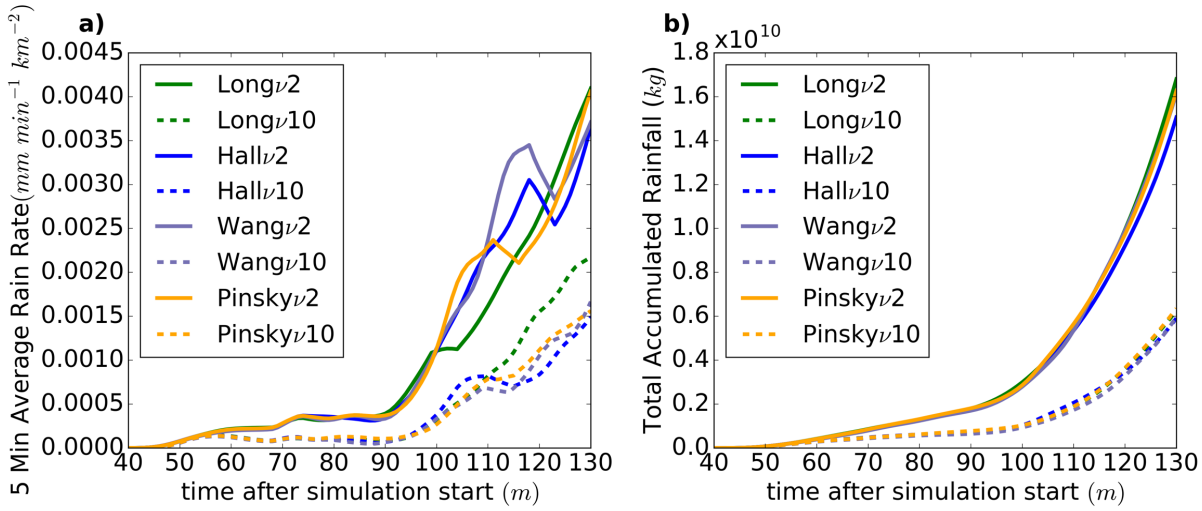

Figure 2.5: (a): Five minute average of grid-mean rain rate (mm minute^{-1} km^{-2}) as a function of time after the simulation start for all $\upsilon = 2$ and 10 simulations (b): The same as in (a) but for total grid accumulated rainfall (kg)

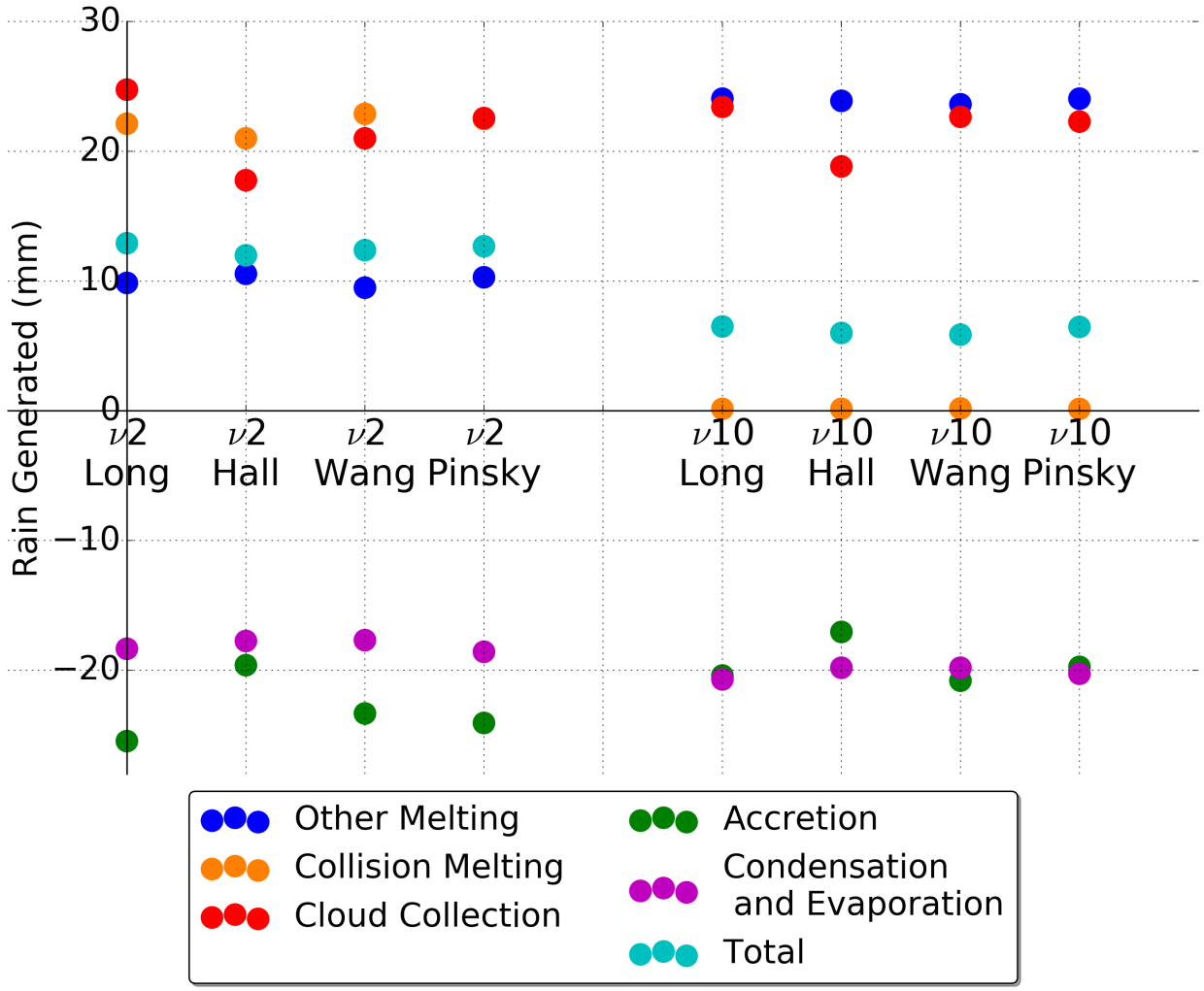

Figure 2.6: Domain and time integrated rain amount (mm) produced or removed by each microphysical process for all eight simulations where $\nu = 2$ and $\nu = 10$. Cloud collection (red dots) relates to cloud and drizzle collision-coalescence with rain and autoconversion of cloud and drizzle to rain; collision melting (orange dots) is defined as the melting of all ice species into rain through the collision of such ice species with the liquid species; other melting (blue dots) is all melting of ice into rain not counting collision melting; ice accretion (green dots) is rain being accreted by ice; and condensation and evaporation (purple dots) are shown as the net of these two processes for rain only. Positive numbers indicate the creation or sources of rain, and negative numbers indicate the removal or sinks of rain. The total (cyan dots) is the sum of all processes. Note that for the Pinskyν2 case, Collision Melting and Cloud Collection are almost equal which makes the Collision Melting dot nearly non-visible.

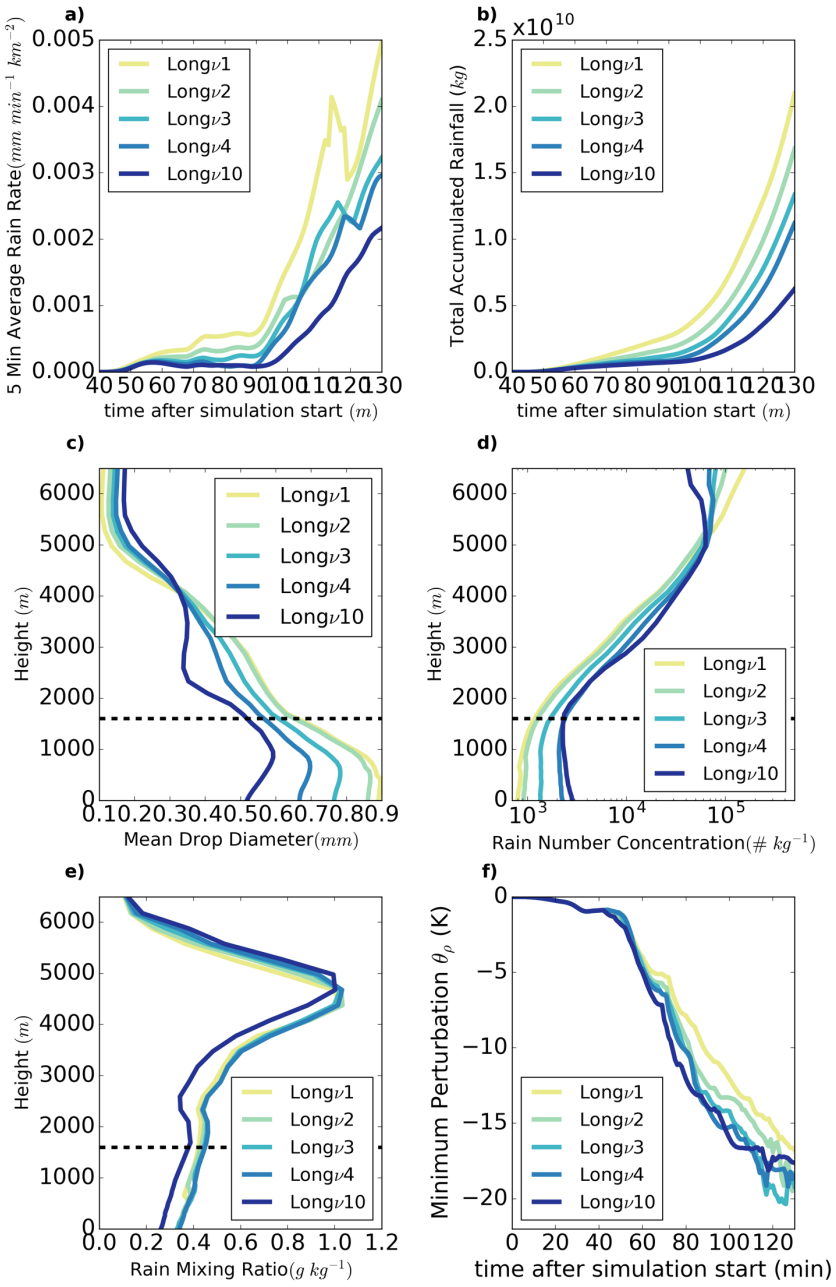

Figure 2.7: a) Five minute average of grid-mean rain rate (mm minute^{-1} km^{-2}) as a function of time after the simulation start. Precipitation did not begin accumulating at the surface until 40 minutes after initialization. b) Total sum accumulated rainfall (kg) as a function of time for all simulations. Mean vertical profiles of c) raindrop mass mean diameter, d) raindrop number concentration, and e) rain mixing ratio averaged over rainy columns (defined as all columns with integrated rain mixing ratio >0.1 g m^{-2}; note that panel (d) uses a log scale on the abscissa) from 40 to 130 minutes after initialization. In (b)–(d), the cloud base (defined as the average lowest point with cloud mixing ratio > 0.1 g kg^{-1}) is denoted by the black dashed line. f) Total integrated ice over time (kg)

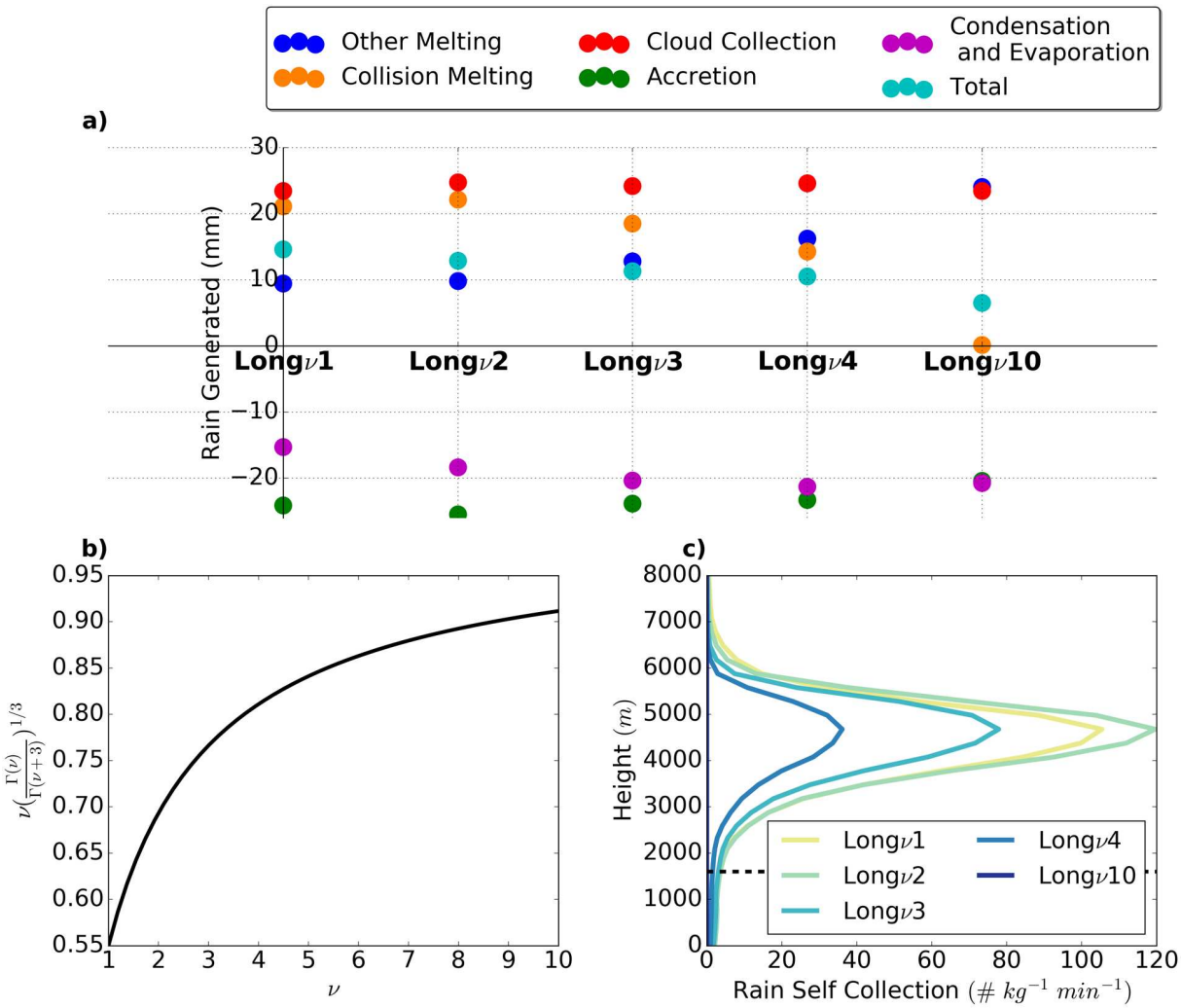

Figure 2.8: a) shows Domain and time integrated rain amount (mm) produced or removed by each microphysical process, with colors the same as in Figure 6. b) shows ν vs. $(\frac{\Gamma(\nu)}{\Gamma(\nu+3)})^{1/3}$ as used in the condensation/evaporation equation. c) shows the temporal and spatial mean vertical profiles of the number of raindrops self-collected per minute ($\#\,kg^{-1}\,min^{-1}$) averaged over rainy points, where rainy points are defined as points containing a rain mixing ratio >0.1 g kg^{-1}. Cloud base (as in Figure 2.7) is denoted by the black dashed line.

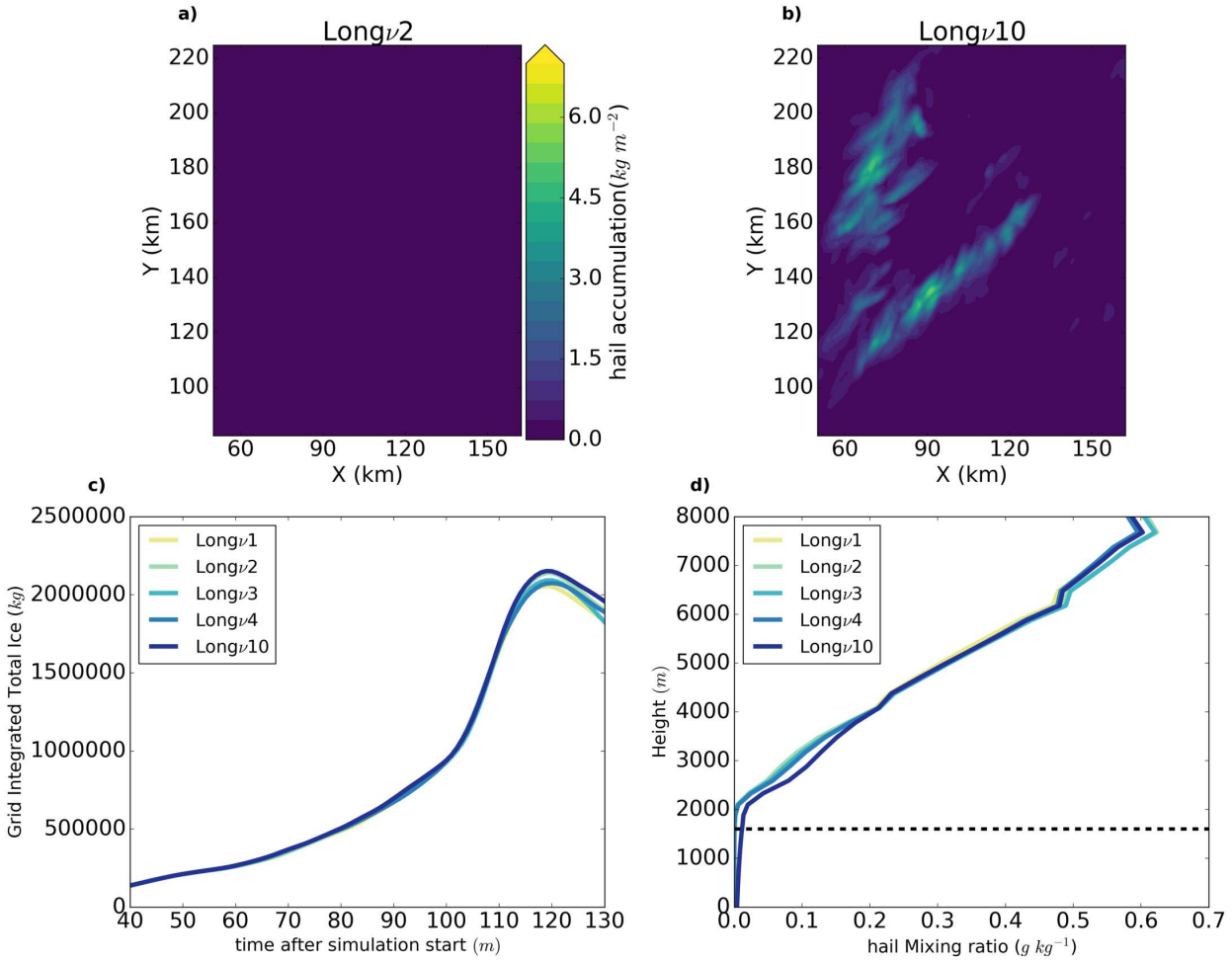

Figure 2.9: Panels a) and b) show accumulated hail precipitation at the ground (kg m^{-2}) at 130 minutes for Longν2 (a; note that this panel should be dark as the maximum value is 0.0003 kg m^{-2}) and Longν10 (b). The color bar for panels a and b lies between them. Panel c shows the grid integrated total ice (kg) over time. Panel d shows the horizontal mean hail vertical profile averaged over columns with an integrated total condensate value >1 kg m^{-2}.

CHAPTER 3: ENVIRONMENTAL CONTROLS ON SUPERCELLULAR TORNADOGENESIS

3.1. Introduction

Tornadoes are some of the most deadly and destructive atmospheric phenomena. In the United States alone, tornadoes are responsible for nearly 150 deaths and $700 million in property damage on average annually (Brooks 2013; Simmons et al. 2013). 90% of the tornado deaths in the US and most of the strongest (EF3 and higher) tornadoes are produced by supercells (Markowski and Richardson 2009; Brotzge et al. 2013). Improving lead times and reducing false alarm incidences is critical to reducing deaths and injuries from tornadoes (Simmons and Sutter 2008). However, approximately 75% of the tornado warnings in the US are false alarms and the average warning lead time for tornadoes is only approximately 10 minutes (Simmons and Sutter 2005, 2008, Brotzge et al. 2011, 2013). Reducing the false alarm ratio and increasing the lead time of tornado warnings requires better understanding of the process of tornadogenesis (TG) and the environments that spawn supercellular tornadoes (Markowski and Richardson 2009). However, current observations of supercellular environments are too spatially and temporally limited to distinguish all tornadic supercells (hereafter TS) and nontornadic supercells (hereafter NTS). Therefore, improving tornado warnings will require new observational platforms with instruments that can observe these environmental conditions. This work aims to (1): examine how the dynamic and microphysical processes are modified within the storm as the environmental conditions are perturbed and what causes either tornadogenesis or the failure of tornadogenesis (hereafter TG) in the perturbed environments and (2): improve our understanding

of the instrument sensitivity that is required to distinguish between the environmental conditions that will produce NTS and those that will produce TS.

Distinguishing between TS and NTS remains a challenging problem (Markowski and Richardson 2009). Even when observing already-formed supercells with radar and *in situ* instrumentation, previous studies have found that the structure and characteristics of TS and NTS appear similar. Markowski et al. (2011) showed that TS and NTS both have significant mid-level rotation of the mesocyclone. Kumjian and Ryzhkov (2008) demonstrated that outside of a tornado debris signature (which by definition will only occur once a tornado has touched down and caused damage), there is not a clear distinction on dual-polarimetric radar between TS and NTS. Van Den Broeke (2016) further refined the work of Kumjian and Ryzhkov and demonstrated that there is one significant difference between the TS and NTS evident in polarimetric radar: the presence of a cyclically appearing hailfall region at the lowest radar elevation level. Van Den Broeke speculated that this cycle could be related to the presence of TG. While the presence of a cyclical hailfall cycle is a possible metric to distinguish between TS and NTS through radar, identifying that a supercell is tornadic can only be done after development of the supercell and its hailfall region, which may not substantially increase lead times. Many others have also found the difficulty in distinguishing TS from NTS with observations (e.g. Trapp 1999; Wakimoto and Cai 2000; Klees et al. 2016).

Modeling results have further shown the difficulty in distinguishing between TS and NTS. Coffer and Parker (2016) demonstrated that one distinguishing factor between TS and NTS in their simulations using composite tornadic and nontornadic VORTEX2 soundings was whether the surface vertical vorticity maxima was co-located underneath the low-level updraft. While this feature could be a useful distinguishing factor between TS and NTS, updraft velocities are

currently extremely difficult to observe operationally and this methodology necessarily requires a near-surface circulation to have already developed. Markowski and Richardson (2013) examined idealized dry simulations with an imposed heat source and sink and found that the simulations that used the medium strength heat sink produced the strongest TG. This suggests, in a realistic storm that includes hydrometeors and cooling due to evaporation of those hydrometeors, that the cold pool may be a control on whether tornadogenesis occurs, and if it does, on the strength of the tornado. The Markowski and Richardson (2013) work therefore indicates that cold pool strength could be a discriminator between TS and NTS. While this can be observed before a tornado touches down and decisions could be made by forecasters based on this information in real-time, the cold pool will once again only develop once the storm is mature, thus restricting the lead-time increase. Therefore, it seems that in order to determine whether a supercell in a given location will be tornadic or nontornadic before it forms, thereby increasing lead times of tornado warnings, the environmental conditions governing TS and NTS formation must be examined.

It is well understood that the environmental conditions, including temperature, humidity, and wind shear, will determine the convective storm type and lifecycle of the storms that form (Weisman and Klemp 1982; Rotunno et al. 1988; McCaul and Weisman 2001; Cohen and McCaul 2006). However, as this parameter space is large, the hazards that will occur when a convective storm forms in a specific set of environmental conditions is still an unsolved problem. When examining supercell tornadogenesis, previous work that has examined environmental conditions has typically either investigated proximity soundings (from ground-based radiosondes, ground-based remote sensing instruments, spaceborne observations, or modeled environments) or through modeling convective storms. However, to the authors' knowledge, no

previous study has examined the measurement accuracy required of instrumentation to successfully discriminate between the environmental conditions of TS and NTS. This study aims to provide insights into this question.

Some of the first studies on the environmental conditions of TS and NTS were done using ground-based radiosonde data as proximity soundings. Brooks et al. (1994) examined fifteen years of radiosonde observations from both the Oklahoma City National Weather Service operational sounding site and National Severe Storms Laboratory field campaigns. They divided these soundings between those that were in proximity to TS versus those in proximity to NTS by examining whether or not a low-level mesocyclone appeared in radar. They found that a useful discriminator was the ratio between the maximum amount of water vapor and the helicity normalized by the minimum wind speed. However, these results are limited by the restricted spatial area of study and because the presence of a low-level mesocyclone does not necessarily indicate presence of a tornado. Others have investigated ground-launched radiosonde-based proximity soundings including Rasmussen and Blanchard (1998a) and Doswell and Evans (2003). In most cases they found that low and mid-level wind shear, thermodynamic instability (including parameters such as CAPE), and the moisture content of the atmosphere (including parameters such as the LCL) are useful parameters to discriminate between TS and NTS environments.

While these studies that have examined ground-launched radiosonde proximity soundings have provided insights into the environmental conditions that distinguish TS from NTS, they tend to be spatially and temporally limited. Recent work using ground-based remote sensing data and gridded data from models and reanalyses has been done to attempt to bridge the spatial and temporal gap. Wagner et al. (2008) used several ground-based Atmospheric Emitted Radiance

Interferometer (AERI) and wind profiling instruments that retrieve thermodynamic and wind shear conditions at approximately 10 minute intervals to examine the temporal evolution of the environment before TS and NTS. They found that CAPE peaks at different times before the storm. However, this study was restricted to four sites of AERI deployments in one location, limiting its generalizability to other regions. Another approach to bridging the spatial and temporal gap has been to use model assimilated data or reanalysis data (e.g. Brooks et al. 2003; Thompson et al. 2003; Brooks 2009). This approach improves both the horizontal spatial and temporal resolution of the proximity soundings analyzed. Using the increased spatiotemporal resolution of a reanalysis dataset, Brooks et al. (2003) created environmental thresholds that they determined could distinguish between tornadic, severe thunderstorm, and nonsevere environments. These thresholds used CAPE, mid-level lapse rate, and wind shear. However, using reanalysis datasets or model data for discrimination between TS and NTS environments has limitations as reanalysis data are not available in real-time and forecast model data may not correctly represent the current environmental conditions.

Studies that examine observations and reanalysis datasets to determine the environmental conditions that distinguish TS from NTS cannot also examine the processes that cause tornadogenesis and how they change with changing environmental conditions. Coffer and Parker (2018) addresses this issue by systematically varying the thermodynamic conditions and vertical wind profile in an idealized, high resolution simulation of a supercell between composite TS and NTS soundings from VORTEX2. They found that the low level wind shear was a much better discriminator than thermodynamics on whether a tornado forms and was a stronger control on tornadic strength in their simulations. They attributed the strong role that wind shear plays to decreasing crosswise horizontal vorticity caused by increasing the low-level wind shear and

therefore low-level helicity. However, their work did not examine the role of specific thermodynamic parameters (e.g. CAPE, LCL, EL) as the thermodynamic profiles were only changed from a TS composite profile to a NTS composite profile.

A different method to resolving the spatial and temporal gap problem presented by proximity sounding studies was presented in Kalmus et al. (2018; hereafter K18). They used the Atmospheric InfaRed Sounder (AIRS) onboard the NASA Aqua satellite. Previous proximity sounding studies over a large area have relied on the operational sounding network, where soundings can be spaced by hundreds of kilometers. Using the AIRS instrument for proximity soundings significantly increases the spatial resolution of the soundings available to the resolution provided by the AIRS instrument, currently 45 km (Maddy and Barnet 2008). Further, the AIRS instrument has a much higher vertical resolution than forecast models and reanalysis data, with vertical grid spacing of 250 m compared to most forecast model and reanalysis data which can have vertical spacings as coarse as 1 km or more (Maddy and Barnet 2008). The sounding product is also available to forecasters in realtime and has global coverage, unlike soundings which are restricted to populated land areas. One drawback to this methodology is that the AIRS instrument does not directly observe winds; however, K18 were able to examine the environmental winds in TS and NTS through a novel backtrace methodology paired with modeled winds. Using this methodology, K18 found that shear magnitude, low-level humidity, storm relative helicity, and LCL were significant discriminators between TS and NTS. Further, K18 produced average values of various thermodynamic and shear parameters for TS, supercells producing large hail, and severe straight-line wind events.

All of these approaches provide observational evidence toward discriminating between TS and NTS and indicate that factors that could distinguish TS and NTS include thermodynamic

parameters (such as CAPE), moisture parameters (including the location of the LCL), and wind shear parameters (e.g. helicity and low-level wind shear). This work builds on the work done by K18 by determining the sensitivity needed to distinguish between these events in realtime and by examining the storm processes that change as environmental parameters are perturbed. The potential for space-based platforms that can add value in operational settings when distinguishing between TS and NTS is significant (K18). This is due to their enhanced spatial resolution and potential for high temporal resolution (with satellite constellations). However, it is critical to examine the sensitivity required of instrumentation to distinguish between TS and NTS environments before designing future satellite platforms. We do not present exact values of environmental conditions that indicate a tipping point between TS and NTS—readers are directed to the work of Coffer and Parker (2018) and others for this. Rather, the focus of this research is to examine the how large the difference is between TS and NTS environments. Determining the difference between these environments will then show how sensitive instruments, especially space-based instruments, need to be to vertical thermodynamic and wind profiles in order to add value when forecasting TS and NTS.

3.2. Methodology

a. Initial Sounding

In order to understand the sensitivity of TS to environmental conditions and the mechanisms within that lead to TG, a suite of numerical model simulations was run that perturb the homogenous initial conditions of a control case (hereafter CTL). Slowly perturbing the initial conditions over a suitable interval of an environment of a TS until TG fails to occur will allow for examination of the processes that change with changing environmental conditions, thereby

addressing the first goal. The simulations also provide insight on how sensitive instruments must be to environmental conditions, and thus addressing our second goal.

The initial homogeneous environmental conditions were based on the thermodynamic profile from Grasso (2000) and are shown in black in Figure 3.1. This sounding has produced TS in previous numerical simulation work (Gaudet et al. 2006; Lerach et al. 2008; Lerach and Cotton 2011) and rapidly leads to the development of a robust supercell, which is useful when conducting a large suite of numerically intensive simulations. For the wind profile, a quarter circle hodograph previously shown to produce supercellular storms was used (Weisman and Rotunno 2000; Dennis and Kumjian 2017).

Given that proximity sounding studies, including K18, have shown that CAPE and the cloud base (typically collocated with the LCL) and both proximity sounding studies and modeling studies, including Coffer and Parker (2016, 2018) have indicated that low level wind shear are potential discriminators between TS and NTS, this study will focus on these three parameters. For this work, CAPE will be defined as the surface-based CAPE, with the parcel starting at the lowest height available in the sounding. The LCL was calculated using a parcel that begins at the surface with Romps (2017)'s exact LCL calculation. The wind shear used was the 0-1 km wind shear as low level wind shear has been shown to be a strong discriminator between TS and NTS (e.g. Coffer and Parker 2016; K18).

b. Sounding Perturbations

To investigate the effects that different environmental conditions have on tornadogenesis within supercells, the CAPE, LCL, and low-level wind shear were perturbed independently while holding all other integrated quantities constant where possible. To determine the magnitude of the perturbations to apply in order to distinguish between TS and NTS, the results from K18

were used. The research presented in K18 examines all storm reports recorded in the US National Center for Environmental Information from 2003-2016 to calculate their averages, making these perturbations robust. For the perturbations in this work, the difference between the K18 Tornado EF4+ and HAIL categories was used, resulting in an initial perturbation in CAPE of approximately 300 J kg^{-1}, an initial perturbation in LCL of 100m, and an initial perturbation in 0-1 km wind shear of 3 m s^{-1}, which will be discussed in detail below. These perturbations allow for a baseline estimate of the environmental condition sensitivity between TS and NTS for our simulations. Three sets of simulations were then performed that perturb the CAPE, the LCL, and the 0-1 km wind shear independently. To the authors' knowledge, this is the first study that examines tornadic environmental conditions by perturbing the CAPE and LCL independently and holding all other variables constant.

c. CAPE Experiments

To change the CAPE without changing other thermodynamic or moisture parameters (e.g. the equilibrium level [EL] or LCL), the mid-level temperature was perturbed to be warmer using a height-weighted gaussian function with a maximum perturbation such that the desired perturbation in CAPE was achieved. The temperature perturbations were made from 750 hPa to 300 hPa, which allowed for the LCL and EL to be kept constant. The different CAPE perturbation simulations, labeled CAPE# where # is an approximate value for the CAPE in J kg^{-1}, and their various thermodynamic parameters are listed in Table 3.1. Table 3.1 also shows the magnitude of the temperature perturbation used to perturb the CAPE. This shows that the change in 300 J kg^{-1} in CAPE only required a mean temperature change of 0.5 K. As also shown in Table 3.1, all four CAPE simulations have a significant tornado parameter much greater than 1, which is considered the value at which storms will be strongly tornadic (Thompson et al.

2002). The thermodynamic profiles used in the CAPE experiments are shown in shades of red on the Skew-T Ln-P plot in Figure 3.1. The surface based CIN for all CAPE experiments was held constant at 0 J kg^{-1}. The wind profile used for all CAPE perturbation simulations was the CTL wind profile.

d. LCL Experiments

When changing the LCL, the low-level water vapor mixing ratio was perturbed using a one-sided gaussian function from 1000 hPa to 850 hPa, with the maximum perturbation at the lowest level of the thermodynamic profile. As elevating the LCL without changing the temperature profile will necessarily lower the CAPE, the temperature from 725 hPa to 200 hPa was negatively perturbed such that the CAPE of each of the LCL perturbation simulations was within 1 J kg^{-1} of the CTL case. While changing the temperature profile will hold CAPE constant, the change to the lower level moisture will change the total integrated water vapor in the column, something that was allowed to occur in these simulations. Although our starting perturbation in LCL in this work, as informed by K18, is a 100m change in the LCL height, only the simulation where the LCL is 200m is presented here, as the simulation where the LCL is raised by 100m produces a storm that is was nearly identical to the CTL case. The parameters of the LCL perturbation simulations, labeled LCL# where # is the approximate LCL height in meters, are listed in Table 3.2. and are shown in teal in Figure 3.1. Table 3.2 shows the water vapor perturbation at the surface necessary to raise the LCL by 200 m, indicating that a 10% perturbation of water vapor at the surface was necessary to raise the LCL by 200m. Further, as in the CAPE experiments, the STP for the LCL1700 case is greater than 1, which is a STP that is considered sufficient for tornadic supercells. The winds from the CTL environmental conditions are used for the LCL perturbation simulations, similar to the CAPE perturbation simulations. As

the LCL is increased as the CAPE is held constant, we can begin to determine whether the LCL height is a valuable metric in tornadogenesis. Further, the sensitivity that an instrument would need to have to lower-level humidity and temperature in order to distinguish between tornadic and nontornadic LCL heights can be found.

e. Wind Shear Experiments

To perturb the low level wind shear, the initial parameters of the function that produced the quarter-circle hodograph as described in Dennis and Kumjian (2017) were changed to produce the shear required. The CTL case was run with a wind shear of 25 m s^{-1} as this is a reasonable wind shear for TG (e.g. Coffer and Parker 2018). The sensitivity experiments were then negatively perturbed by 3 m s^{-1}, the starting point as described in Section 3.2b, until tornadogenesis ceased. The parameters for all shear simulations are described in Table 3.3, where they are labeled Shear# where # is the approximate 0-1 km wind shear in m s^{-1}. The different wind profiles used are also shown in the hodograph in Figure 3.1. The CTL thermodynamic profile was used for all wind shear experiments (shown in black in the Skew-T Ln-P in Figure 3.1). Reducing the shear while holding the thermodynamic profile constant will provide insights into what the sensitivity to lower-level winds would need to be to distinguish between TS and NTS producing environments. Further, although previous studies have examined tornadic sensitivity to lower-level wind shear in models, including that of Coffer and Parker (2018), this study examines wind shear perturbations in the context of comparison against thermodynamic perturbations.

f. Model Setup Details and Tornado Definition

The open-source Regional Atmospheric Modeling System (RAMS) version 6.2.08 was used to perform the numerical model simulations for this study (Cotton et al. 2003b; Saleeby and van

den Heever 2013). RAMS is a nonhydrostatic mesoscale model that is frequently used to simulate deep convective storms (e.g. Barth et al. 2007; Nair et al. 2013; Federico et al. 2014; Grant and van den Heever 2014) including TG (e.g. Gaudet et al. 2006; Lerach et al. 2008; Lerach and Cotton 2011). The model parameters specific to these experiments are listed in Table 3.4. Highlights include a constant surface roughness, a convergence zone initialization, no coriolis force, and a 250 x 225 x 20 km model domain with horizontal grid spacing of 125m and a stretched vertical grid with 10m grid spacing at the surface stretched to 100m. The high resolution enables simulation of tornado like vortices as have been observed in previous studies of similar resolution (e.g. Gaudet et al. 2006; Lerach and Cotton 2011; Markowski and Richardson 2013; Coffer and Parker 2016, 2018).

For the simulation to be considered tornadic, we require vertical vorticity (ζ) at the lowest above-ground model level greater than 0.1 s^{-1} and co-located horizontal wind speed greater than 29 m s^{-1} (the minimum wind speed for an EF-0 tornado), which are similar thresholds that have been used in previous literature (e.g. Gaudet et al. 2006; Lerach et al. 2008). As we are defining our tornado based in part on the vertical vorticity at the surface, it is useful to examine the vertical vorticity tendency equation in order to understand the source of surface ζ. The tendency of ζ with time, when making the Boussinesq approximation, is expressed as:

$$\frac{\partial \zeta}{\partial t} = -\vec{v} \cdot \vec{\nabla}(\zeta + f) + \vec{\omega} \cdot \vec{\nabla} w + f \frac{\delta w}{\delta z} + \hat{k} \cdot \vec{\nabla} \times \vec{F} \qquad (3.1)$$

where ζ is the vertical vorticity (s^{-1}), t is time (s), $\vec{v}$ is the three dimensional wind velocity vector (m s^{-1}), f is the Coriolis force (0 in the simulations presented in this work), $\vec{\omega}$ is the three dimensional vorticity vector (s^{-1}), w is the vertical wind speed (m s^{-1}), z is height (m), and $\vec{F}$ is the three dimensional friction variable (m s^{-2}). Within expression (3.1), $-\vec{v} \cdot \vec{\nabla}(\zeta + f)$ is typically referred to as the advection term, $\vec{\omega} \cdot \vec{\nabla} w$ is referred to as the tilting/stretching term,

$f\frac{\delta w}{\delta z}$ is the Coriolis force term, and $\hat{k} \cdot \vec{\nabla} \times \vec{F}$ is the viscous effects term. The only two sources of ζ in the simulations presented here are the tilting/stretching term and the viscous effects term. This is because while advection can be a local source/sink, it cannot create nor destroy grid integrated ζ and the Coriolis term will be 0 as the Coriolis force is disabled in the simulations presented here.

3.3. Results

a. The Control Simulation

Before proceeding to discuss the sensitivity to environmental conditions that distinguish TS from NTS, the control simulation (hereafter CTL) will be analyzed to determine whether the initial sounding produced a TS and to understand the characteristics of the storm and the strength of the tornado, if one is produced. Figure 3.2 shows both a 3-D view of the CTL simulation (3.2a) and a plan view time series (3.2b-e) of the evolution of the storm. The 3-D view, which shows a white isosurface of total condensate (excluding rain which has been omitted for visual clarity but does not change the appearance of the storm structure) and a red isosurface of all points matching our definition of a tornado (described in Section 3.2d), indicates that the CTL simulation produces a vigorous supercell with developed convective and anvil regions. The identified tornado reaches the ground, which indicates that the supercellular storm produced with the CTL environmental conditions is tornadic. Further, the time series (Figure 3.2b-e) shows that the vigorous supercell quickly splits into right-moving and left-moving storms with their own independent updrafts, as would be expected for this idealized quarter-circle hodograph (Weisman and Rotunno 2000). The two condensate contours demonstrate that the storm develops a large anvil, extending over the main condensate region. The condensate region in the midlevels shows evidence of a splitting supercell, although the separation in condensate is less clear than the

separation in updrafts at this level. For the remainder of this work, we will focus on the right-moving storm as the right-moving storm is the more vigorous storm in all cases, and it is this storm that produces the tornado in all tornadic cases.

Figure 3.3a shows the track of the tornado and the evolution of the low and mid-level updrafts for the right moving storm for the CTL case. To show the track of the tornado, the tornado intensity, and the tornado width, the tornado track product shown here is the maximum wind speed for each grid point over all times that met the tornadic threshold. It should be noted that the output interval for all simulations was 30 seconds due to computational limits and the tornado tracks were not interpolated in space or time. This occasionally results in gaps in the contoured tornado tracks in this product, as demonstrated by the CTL simulation in Figure 3.3a even though the simulation produces a tornado that is not interrupted as shown in Table 3.1. The low (red contour; 20 m s^{-1}) and mid (gold contour; 25 m s^{-1}) level updrafts in this figure are drawn every 10 minutes beginning at t=30 minutes. Further, Table 3.1 shows the maximum tornado horizontal wind speed and the tornado duration for the CTL simulation, indicating that the CTL simulation produced a long-lived tornado that reached EF-2 strength.

b. CAPE Perturbation Experiments

In this section, results from the simulations that only perturb the CAPE will be examined. Figure 3.3 shows tornado tracks and the evolution of the low and mid-level updrafts for the right-moving storm for all CAPE cases. The times where a tornado was identified for the CTL case and all of the associated perturbed CAPE cases are noted in Table 3.1, along with the maximum horizontal wind speed of the tornado and its EF rating. Figure 3.3 and Table 3.1 indicate that the CTL and CAPE4200 cases produced a strong tornado, with the CAPE4200 simulations producing a slightly stronger and wider tornado than in the CTL case. The processes causing the

increase in tornadic intensity when reducing cape from the CTL to the CAPE4200 experiment will be investigated below. While the CAPE3900 simulation does produce a tornado for 1 minute, the maximum wind speed of the tornado in this case is barely above the EF-0 threshold imposed by our tornadic definition (as seen in Table 3.1). The CAPE3600 simulation does not produce a tornado. Thus, there is a 300 J kg^{-1} range in CAPE between CAPE3900 and CAPE3600 which results in cessation of TG in the supercell. These results therefore indicate that, in order for an instrument to be able to distinguish between an environment that will produce TS from one that will produce only NTS, it must be able to capture CAPE to an accuracy of at least 300 J kg^{-1}, which corresponds to an average change in temperature of approximately 0.5K throughout the column.

The processes that result in tornadogenesis (or lack thereof) with changing CAPE will now be investigated. Figure 3.3 shows the mid (4.5 km) and lower level (1 km) updrafts at 25 m s^{-1} and 20 m s^{-1} respectively at t=30, 40, and 50 minutes. Figure 3.3 indicates that as CAPE decreases, the size of the region of strongest updrafts in the mid-levels decreases, as would be expected. Figure 3.4 shows the 1 km updraft field (filled contours), 4.5 km updraft (gold contour; at 25 m s^{-1} only), and the location of the tornado (if applicable; green dot) at 33.5 minutes after simulation initialization, the first instance of a tornado in the CAPE4200 simulation. It is evident that all four simulations produce the characteristic horseshoe-shaped lower-level updraft, emblematic of a vigorous supercellular storm with a collocated mesocyclone (Lemon and Doswell 1979; Byko et al. 2009; Grant and van den Heever 2014). It has been shown in previous literature that the region of downdrafts located in the center of the lower-level updraft region is a likely location of tornadogenesis, a result that is repeated in this case for the CTL and CAPE4200 storms (Markowski et al. 2011).

It is reasonable at this point to wonder why the CAPE3600 simulation fails to produce a tornado. All four CAPE simulations produce a horseshoe-shaped low-level updraft with the mid-level updraft either overlaid or nearby, which has been noted as a distinguishing factor between TS and NTS (Coffer and Parker 2016). Each simulation has a similar magnitude of horizontal vorticity available to be tilted into vertical vorticity in the lower levels at the time of tornadogenesis for the CAPE4200 simulation (not shown), and sufficient updraft strength, shape, and area to tilt and stretch the horizontal vorticity. Further, the surface roughness characteristics were identical for all simulations, reducing significant impacts from differences in the frictional vorticity generation term. One possible distinguishing factor between the TS and NTS is in the large difference between the four storms' cold pools. Figure 3.5 shows the perturbation density potential temperature at 34 minutes, where $\theta_\rho' = \theta_\rho - \theta_{\rho,env}$, $\theta_{\rho,env}$ is the initial homogenous θ_ρ, and $\theta_\rho = \theta(1 + 0.61r - r_L)$, where θ is the potential temperature, r is the mixing ratio of water vapor, and r_L is the mixing ratio of liquid water. As θ_ρ is a measure of density, negative values of θ_ρ' indicate regions of denser, more negatively buoyant air. Overlaid on Figure 3.5 are streamlines of near-surface horizontal winds (grey) and low and mid-level updrafts (as in Figure 3.3). This figure demonstrates that as CAPE decreases, the cold pool gets colder, and more negatively buoyant air is transported into the inflow and updraft region.

The reason for an increase in cold pool strength with decreasing CAPE is not necessarily intuitive. As CAPE is reduced, the onset of precipitation at the surface in these simulations is earlier as the lower CAPE values produce a weaker updraft and a storm that begins to precipitate sooner. Therefore, at this relatively early time in the storm's development, the weaker CAPE simulations have a stronger cold pool in the rear flank downdraft region than the storms in higher-CAPE environments due to the earlier onset in precipitation. This means that at the time

of tornadogenesis the CTL case has a very weak cold pool, therefore limiting the amount of negatively buoyant air that is transported into the updraft region. At the same time in the lower CAPE experiments the cold pool gets stronger, and therefore more negatively buoyant air is transported into the updraft region. For the CAPE4200 case, this results in a strengthened tornado, but for the CAPE3900 and CAPE3600 cases which have stronger cold pools, the transport of strongly negatively buoyant air into the updraft reduces the updraft strength and eventually results in a NTS.

The result from the CAPE perturbations appears to be in keeping with the work done in a highly idealized dry framework by Markowski and Richardson (2013). As in their work, TG in the four CAPE simulation storms appears to be modulated by the strength of the cold pool, with the moderate strength cold pool in the CAPE4200 simulations producing the strongest tornado. High temporal resolution trajectories would be necessary to confirm this hypothesis, but were too computationally expensive to conduct.

In these experiments, a difference of 300 J kg^{-1} of CAPE resulted in the failure of tornadogenesis between the CAPE3900 and CAPE3600 cases, indicating that instruments seeking to distinguish between TS and NTS environments must be able to capture CAPE to within 300 J kg^{-1}. Further, a difference of 300 J kg^{-1} in CAPE also resulted in a change of tornadic strength from a damaging EF-3 to a weak EF-0 between the CAPE4200 and CAPE3900 simulations. This indicates further that instruments that can retrieve temperature to within 0.5 K in the vertical profile, the temperature accuracy necessary to calculate CAPE to within that threshold, may be able to provide insights on tornadic strength.

c. LCL Perturbation Experiments

While the suite of experiments that perturb the CAPE provide insights into the accuracy that an instrument would need in terms of temperature retrievals in order to distinguish between TS and NTS environments, our methodology does not perturb the moisture when perturbing CAPE. This section now examines the accuracy that a sensor would need when retrieving moisture to distinguish between TS and NTS environments. We will focus on the low-level moisture on these cases through perturbing the LCL as the effects of perturbing mid-level moisture on supercells has been examined by Grant and van den Heever (2014) and others. The different LCL thermodynamic profile that forms the LCL perturbation experiment can be seen in teal on Figure 3.1 and is described further in Table 3.2. CAPE is held constant in these experiments.

Figure 3.6 shows the integrated tornado tracks and updraft evolution, similar to Figure 3.3, for the CTL (LCL height of 1597 m) and LCL1700 (LCL height of 1797 m) cases. This figure indicates that when changing the LCL, but holding CAPE constant, that the tornado gets slightly weaker and does not last as long. Figure 3.3 also indicates that, as the LCL is raised, the area of the strongest mid-level updrafts increased. However, both the CTL and LCL1700 cases still produce a tornado of similar strength, with the LCL1700 case having a slightly weaker tornado. The processes that cause the higher LCL environmental conditions to produce a TS will be investigated further. However, it is important to first address why the LCL was not continuously raised until tornadogenesis ceased, but was only raised 200 m in these experiments. In order to examine the LCL height independently, the CAPE and equilibrium level were kept constant by reducing the environmental temperature in the midlevels. If the LCL were to be perturbed higher, the temperature perturbation necessary for the CAPE and equilibrium level to

remain constant would result in a statically unstable layer in the environmental sounding, which would quickly mix out in the atmosphere.

The changes to the storm structure and tornadogenesis when the LCL is raised will now be examined. Figure 3.7a-b shows the lower-level updrafts at the time of tornadogenesis (31.5 minutes after initialization) for both the CTL and LCL1700 cases at 1 km (similar to Figure 3.4). The updraft structure at 1 km and 5 km represented in Figure 3.7a-b indicates that both the low and mid-level updraft change as the LCL is raised. However, examining a constant height cannot be done in this case as the LCL has been raised by 200m. Figure 3.7c-d shows the low level updraft 200m above Figure 3.7a-b for both the LCL1700 and CTL cases. These figures indicate that even when shifting our horizontal cross-section by the amount of the LCL increase, that the updraft structure is still different between the LCL1700 and CTL cases. At both 1 km and 1.2 km, the updraft is horseshoe-shaped and strong. Although the LCL1700 case has a prominent updraft region that does not dissipate earlier than the updraft in the CTL storm (demonstrated in Figure 3.6), the tornado is still shorter-lived and weaker in the LCL1700 case than the CTL case. This suggests that updraft strength is not the only contributor to the earlier cessation of the tornado in the LCL1700 case.

One possibility, as in the CAPE simulations, is that the tornado strength is controlled by the buoyancy of the air in the RFD. Figure 3.8, as in Figure 3.5 (although with a shifted color bar) shows θ_ρ' at 31.5 minutes after initialization and 5 minutes later. In the CTL case, the development of the weak cold pool can be seen, especially at the later time. However, in the LCL1700 case, a positive θ_ρ' is shown in the RFD region. This is an unusual finding as the RFD is usually a region of rainfall with an associated area of cooler, more dense air that generates and drives the cold pool. However, in this case, the RFD transports higher θ_ρ air. Rainfall in the

downdraft starts to evaporate at a higher elevation because of the lower environmental humidity in the boundary layer in the LCL1700 case. This is because the condensate in the downdraft evaporates before reaching the ground, thereby eliminating the contribution of lower-level evaporative cooling in the thermodynamics of the downdraft. The air in the downdraft therefore starts to warm near the surface due to compressional warming and the entrainment of higher θ_ρ air from above. This region of positively buoyant air in the inflow region of the storm in the LCL1700 case does not appear to hinder the early development of the tornado. This is likely due to the fact that this higher θ_ρ' does not appear in this region until 29 minutes after initialization. The transport of higher θ_ρ' air from the RFD reduces the temperature contrast between the updraft and downdraft, which decreases the amount of horizontal vorticity generated until the tornado ceases. This is similar to the CAPE results and is also keeping in line with Markowski and Richardson (2013) who indicated that a weaker cold sink will result in a weaker tornado.

Although the LCL was not perturbed sufficiently to cease tornadogenesis, these simulations do indicate that an instrument may be able to distinguish between the strength of the tornado produced by TS if it is able to capture the LCL to within 200 meters. Achieving this LCL accuracy would require an instrument that is able to measure surface water vapor pressure to within 2.3 hPa. In this case, the tornado intensity was weakly controlled by the LCL height, with a higher LCL height producing a slightly weaker, shorter lived tornado than that in an environment with a lower LCL height. Others have also found that the LCL is a weak discriminator between TS and NTS (Rasmussen and Blanchard 1998b; Thompson et al. 2004). As the LCL height is correlated with CAPE, it is possible that the LCL height as observed in K18 and other studies is simply a proxy for CAPE, reinforcing the results found in the CAPE experiments.

d. Shear Perturbation Experiments

In this section, changes to the storm and the associated tornadogenesis that occurs as the lower level wind shear is reduced will now be discussed. Figure 3.9 shows the tornado tracks and low and mid-level updrafts for the three Shear perturbation experiments. From this figure it is apparent that the tornado is weaker when the lower-level wind shear is reduced by 3 m s^{-1}, the magnitude discussed in K18. When further reducing the wind shear, tornadogenesis does not occur as is evident from the Shear22 results. These simulations therefore suggest that an instrument would need to be able to differentiate wind shear to an accuracy of at least 3 m s^{-1} in 0-1 km wind shear in order to distinguish between TS and NTS environments, and is in keeping with the findings of K18.

In order to determine why reducing the shear ceases tornadogenesis, the lower-level updraft field will be examined at the time that a tornado is first identified in the Shear25 simulation, the case with the weakest tornado of the shear simulations. At this time, while the CTL storm has a strong updraft wrapped around a weaker region of downdrafts, the Shear25 and Shear22 cases produce a progressively weaker lower-level updraft, albeit with a similar shape to that of the CTL case. The decrease in updraft speed with decreasing wind shear is expected and has been reported on previously in the literature (e.g. Weisman and Klemp 1982). Although the reduction in updraft speed will necessarily reduce the magnitude of the tilting/stretching term in expression 3.1, this does not provide a full reason for why reducing the wind shear in these cases does not produce a tornado.

When examining the CAPE and LCL experiments, the changes to the tornado appear to be primarily due to modulation of the cold pool strength. However, in the Shear experiments, the cold pool strengths are nearly identical (not shown), thus eliminating that process as a reason for

the change in tornadic strength. However, as would be expected when reducing the vertical wind shear, the horizontal components of the vorticity decrease as the wind shear decreases. Figure 3.11 shows, for all Shear cases, the value of $\overrightarrow{V_H} \cdot \overrightarrow{\omega_H}$ (m s^{-2}, in shaded contours) at approximately 400 m above ground. This figure indicates that the amount of horizontal vorticity transported into the updraft region, both positive and negative, is much larger in the cases with higher vertical shear (CTL). This transport is reduced as the vertical wind shear is reduced. This indicates that, even for the same updraft velocities, there would be less vertical vorticity generated through tilting of horizontal vorticity as there is less horizontal vorticity available to transport. In this case, it thus appears that tornadogenesis does not occur due to a combination of weaker low-level updrafts and reduced horizontal vorticity in the weaker wind shear cases.

The results from this section indicate that the wind shear is a strong control on whether a supercell would become tornadic. Similar results have been previously observed (e.g. Markowski and Richardson 2009; Coffer and Parker 2016, 2018). An instrument that may be able to provide value in distinguishing between TS and NTS environments would need to observe the 0-1 km wind shear to within 3 m s^{-1}.

3.4. Conclusions

The primary goals of this study were to (1): examine how the dynamic and microphysical processes are modified within the storm as the environmental conditions are perturbed and what causes TS or NTS to be produced and (2): improve our understanding of the instrument sensitivity that is required to distinguish between TS and NTS environments. To examine this, seven high resolution numerical simulations were performed in which CAPE, LCL, and shear were progressively varied. The magnitude of the perturbations were based on differences between strong tornadic storms and hail producing storms found in Kalmus et al. (2018). The

control simulation was initialized with environmental conditions emblematic of a tornadic supercell (Section 3.3a). A strong, splitting supercell with an EF-2 tornado was produced in this simulation.

To determine how accurate an instrument would need to be to capture the differences in CAPE between environmental conditions that will produce TS from those that will produce only NTS and to examine how the supercell changed as the environment was perturbed, the CAPE was systematically perturbed. The perturbation experiments indicated that an instrument that could retrieve temperature to within 0.5 K, corresponding to a change in CAPE of 300 J kg^{-1}, could distinguish between both TS and NTS and between damaging TS and weakly-damaging TS. The mechanism that modulated tornado strength in these simulations appears to be related to the strength of the cold pool. The results of these simulations are in support of the idealized results described by Markowski and Richardson (2013) and increase the robustness of their results as the simulations here present a much more realistic storm that includes condensate than was presented by Markowski and Richardson (2013), which were highly idealized dry simulations. After examining the sensitivity required in CAPE, perturbations to the control environmental conditions in the LCL were examined. It was found that an instrument would not need a particularly high sensitivity to the LCL to discriminate between TS and NTS environments, with our experiment indicating that even a 200m raise in the LCL, which is associated with a change in the lower level moisture of about 10% when keeping CAPE constant, would still result in a tornado, albeit a weaker tornado. Finally, sensitivity to low-level wind shear was examined. The sensitivity experiments showed that differences in 0-1 km vertical wind shear of 3 m s^{-1} separated TS from NTS. This result is in keeping with the statistical study of

K18. The result demonstrates that if an instrument is able to retrieve 0-1 km wind shear to that accuracy, it could add value in distinguishing between TS and NTS environments.

If a platform could add value to TS nowcasting by retrieving CAPE to within 300 J kg^{-1} and 0-1 km wind shear to within 3 m s^{-1}, as our work demonstrates, it is prudent to examine existing instruments to understand where these measurement targets are already being met and where development of proposed new platforms may help. Currently, only ground-based measurements can meet both of these criteria, with instruments such as radiosondes and ground-based remote sensing instruments being the only instruments capable of measuring the wind shear. However, the infrastructure requirements and cost of these platforms make them difficult to deploy worldwide at a sufficient horizontal resolution, and with the exception of field campaigns are strictly limited to land. The advent of space-based thermodynamic profiling, such as the Atmospheric InfraRed Sounder (AIRS) on the Aqua satellite, can provide global coverage at a much higher horizontal spatial resolution (approximately 45 km) than ground-based instruments (ground-launched soundings are spaced hundreds of km apart in the US), although they can only retrieve thermodynamic profiles and not wind profiles. However, this work indicates that they still may be significantly useful for tornadogenesis forecasting if they are able to retrieve CAPE to within 300 J kg^{-1}, requiring a temperature accuracy of ~0.5 K.

Fortunately, several instruments currently in orbit are able to provide temperature profiles that have an accuracy to within 0.5K. However, these platforms are typically polar-orbiting and can therefore only provide observations twice per day. On the other hand, as our work and other work has shown that lower-level wind shear is an important predictor on tornadogenesis, these satellites or other associated platforms would also need to observe winds in the lower levels, something that is difficult to do from a space-based platform. Some work has demonstrated skill

in space-based observations of wind (Bessho et al. 2006), but little work has examined how accurate this is in the lowest levels of the atmosphere, particularly over land. Our work indicates that if satellite lower-level wind retrievals are improved that this, coupled with their current ability to retrieve the thermodynamic profile globally, would mean that space-based platforms could add significant value in discriminating between TS and NTS environments.

While our study has suggested several accuracy thresholds that instruments may need to meet in order to add value when observing environments to distinguish between TS and NTS production, there are limitations to this study and hence we suggest the following areas as future research. Homogeneous environments have been widely used to produce simulations that demonstrate supercell processes (e.g. Gaudet et al. 2006; Lerach and Cotton 2011; Markowski and Richardson 2013; Grant and van den Heever 2014; Coffer and Parker 2016), however real-world environments are seldom, if ever, homogenous. This study also utilized a single idealized sounding and perturbed its CAPE, LCL, and low-level wind shear. While this allowed for a consistent control case to compare the environmental perturbations with, it also limits the conclusions that this work can make given that it is based on one set of initial environmental conditions. Future work should consider more soundings and could incorporate an ensemble approach similar to Coffer and Parker (2016) to further evaluate the ranges determined here over a wider range of environmental conditions. Despite these limitations, this study does present accuracy ranges required for platforms to add value when observing TS and NTS environments.

3.5. Tables and Figures

Table 3.1: Parameters and tornado information for the CAPE simulations. The calculations for Significant Tornado Parameter use Helicity values calculated with (Bunkers et al. 2000) right-moving storm motion

Parameter	CTL	CAPE4200	CAPE3900	CAPE3600
SBCAPE (J/Kg)	4517	4217	3917	3617
Fixed Layer STP	2.34	2.18	2.03	1.87
Maximum Temperature perturbation (K)	N/A	-2.43	-4.85	-7.31
Maximum temperature perturbation (%)	N/A	-0.9%	-1.9%	-2.8%
Mean Temperature Perturbation (K)	N/A	-0.50	-1.05	1.58
Mean Temperature Perturbation (%)	N/A	-0.2%	-0.4%	-0.6%
Times with tornado (minutes after initialization)	31.5-35.5; 37-56	33.5-53.5	38-39	N/A
Tornado Maximum Wind Speed (m s^{-1}) and EF Rating	54.7 (EF-2)	72.2 (EF-3)	34.2 (EF-0)	N/A

Table 3.2: Parameters and tornado information for the LCL simulations. The LCL here was calculated with the (Romps 2017) exact LCL formulation.

Parameter	CTL	LCL1700
LCL (m)	1597	1797
SBCAPE (J/Kg)	4517	4517
Fixed Layer STP	2.34	1.17
Maximum Water Vapor perturbation (hPa)	N/A	2.33
Maximum Water Vapor perturbation (%)	N/A	9.5%
Mean Temperature Perturbation (K)	N/A	1.37
Mean Temperature Perturbation (%)	N/A	0.53%
Times with tornado (minutes after initialization)	31.5-35.5; 37-56	31.5-40.5; 42.5-47
Tornado Maximum Wind Speed (m s^{-1}) and EF Rating	54.7 (EF-2)	49.0 (EF-1)

Table 3.3: Parameters for the Shear simulations. The helicity described here is a 0-1 km helicity using the (Bunkers et al. 2000) right moving storm motion.

Parameter	CTL	Shear25	Shear22
0-1 km Wind Shear (m s^{-1})	28.35	25.35	22.35
0-1 km Helicity (m^2 s^{-2})	192.91	166.50	139.0
Fixed Layer STP	2.34	2.02	1.69
Times with tornado (minutes after initialization)	31.5-35.5; 37-56	37-41	N/A
Tornado Maximum Wind Speed (m s^{-1}) and EF Rating	54.7 (EF-2)	52.3 (EF-2)	N/A

Table 3.4: Model Parameters

Parameter	Value
Grid spacing	$\Delta x = 125$ m; Δz stretched from 10 m to 100 m at a stretch ratio of 1.075
Grid	2000 x 1800 x 225 grid points (250 x 225 x 20 km)
Boundary Conditions	Horizontal: periodic; bottom: horizontally homogenous surface roughness with roughness length of 3 cm. Top: Rayleigh damping layer through 600m.
Radiation	None
Simulated time	60 minutes; $\Delta t = 0.5s$
Microphysics	Fully double-moment RAMS microphysics that includes three liquid and five ice hydrometeor species. (Saleeby and Cotton 2008; Saleeby and van den Heever 2013)
Initialization	Convergence zone as in (Loftus et al. 2008; Schumacher 2009). 15 km radius with maximum convergence $5 \times 10^{-3}\ s^{-1}$ extending from the surface to 4.5 km for 10 minutes, increasing to the maximum convergence linearly over 10 minutes.
Surface Roughness	Constant roughness length of 3 cm

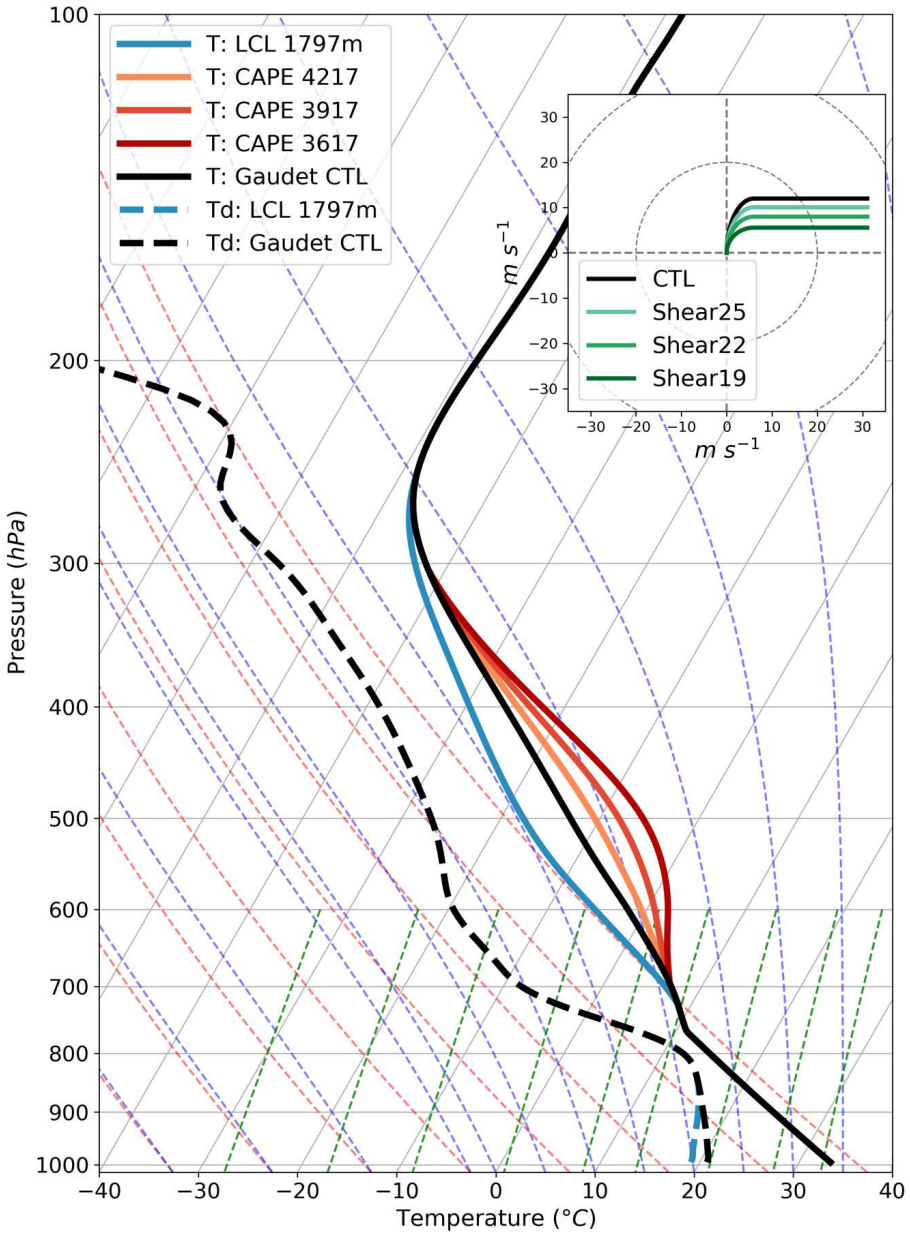

Figure 3.1. A skew-T ln-P representation of the initial homogenous initial thermodynamics used for all simulations. Temperature for the simulations are represented by the solid lines, dew point is represented by the dashed lines, with the CTL thermodynamic profile used for all Shear simulations. The inset plot is a hodograph representing the initial vertical wind profiles for all simulations, with the CTL wind profile used for all LCL and CAPE simulations.

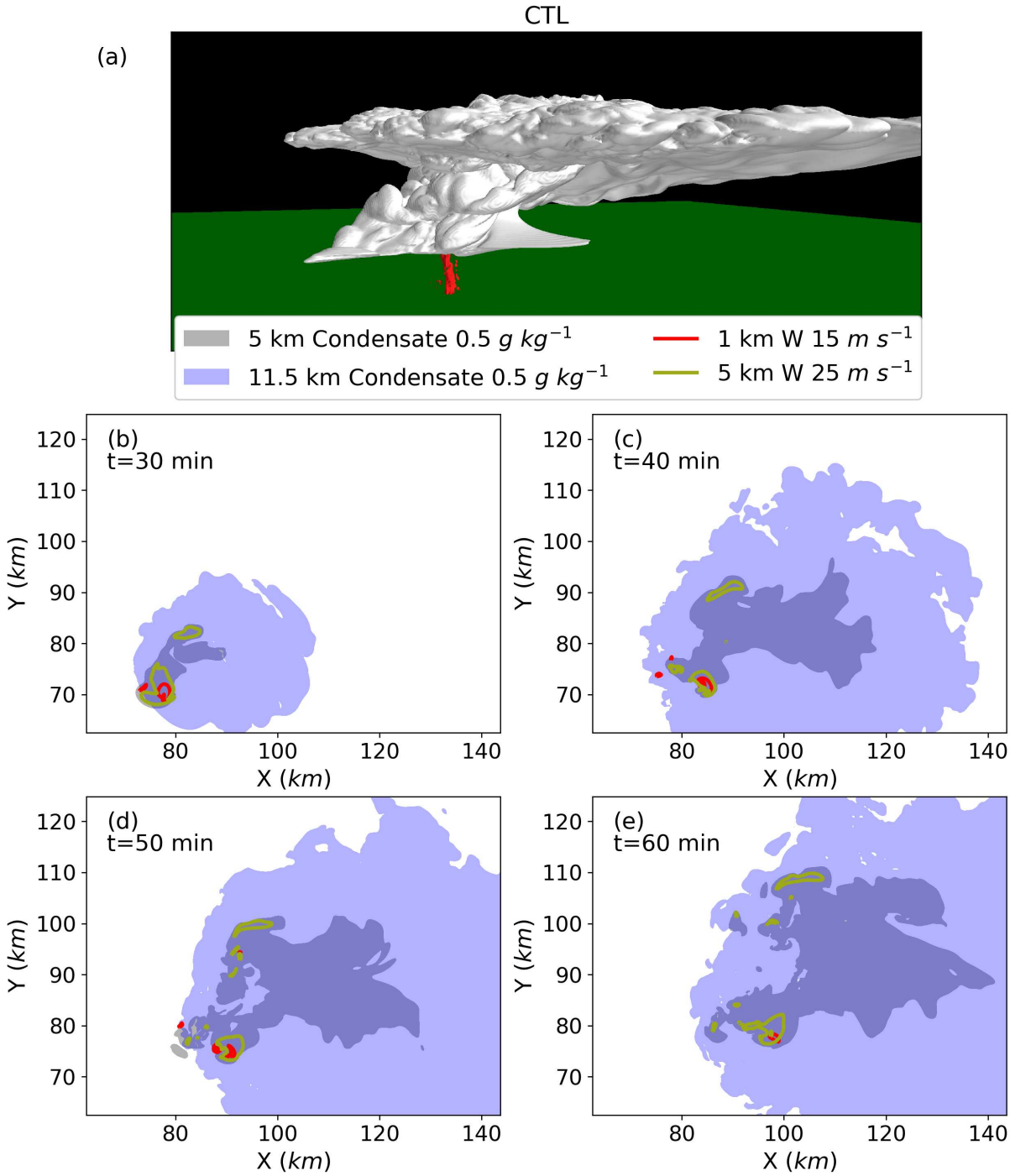

Figure 3.2. (a) 3-D plot of control simulation at 40 minutes after initialization. The white isosurface of 1 g/kg total condensate (excluding rain for visual clarity), and the red isosurface is an isosurface of 0.1 s^{-1} ζ. (b-e) timeseries of total condensate at 5 km (0.5 g kg^{-1}, grey/purple), 11.5 km (0.5 g kg^{-1} , light purple), 1 km W (15 m/s, red outline), and 5 km W (25 m/s, gold outline)

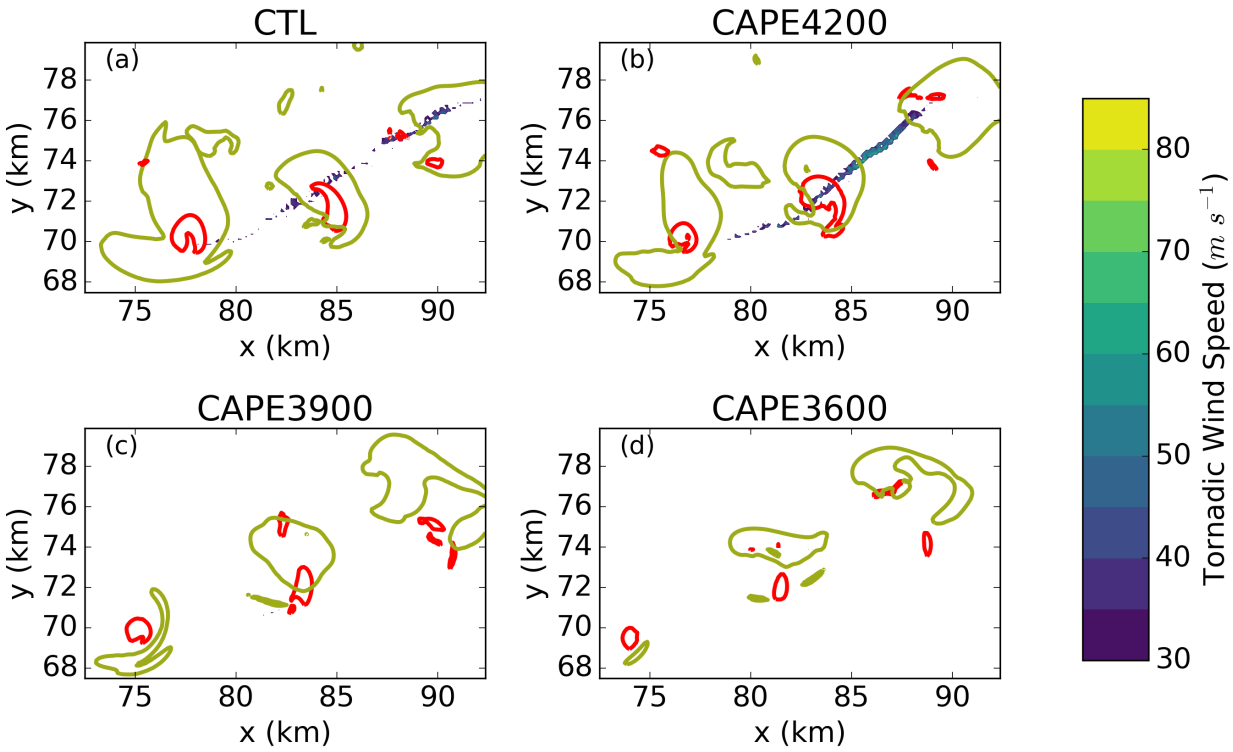

Figure 3.3. Tornado tracks and updrafts for all four simulations (the CTL case has CAPE of 4517 J kg^{-1}). The filled contour in all panels is the wind speed where the winds are collocated with an identified tornado as described in the text. The winds are plotted in 30s increments. Contour lines in all panels are updrafts at 10 minute increments. Brown lines are updrafts at 4.5 km at 30 m/s and red lines are updrafts at 1 km at 20 m/s.

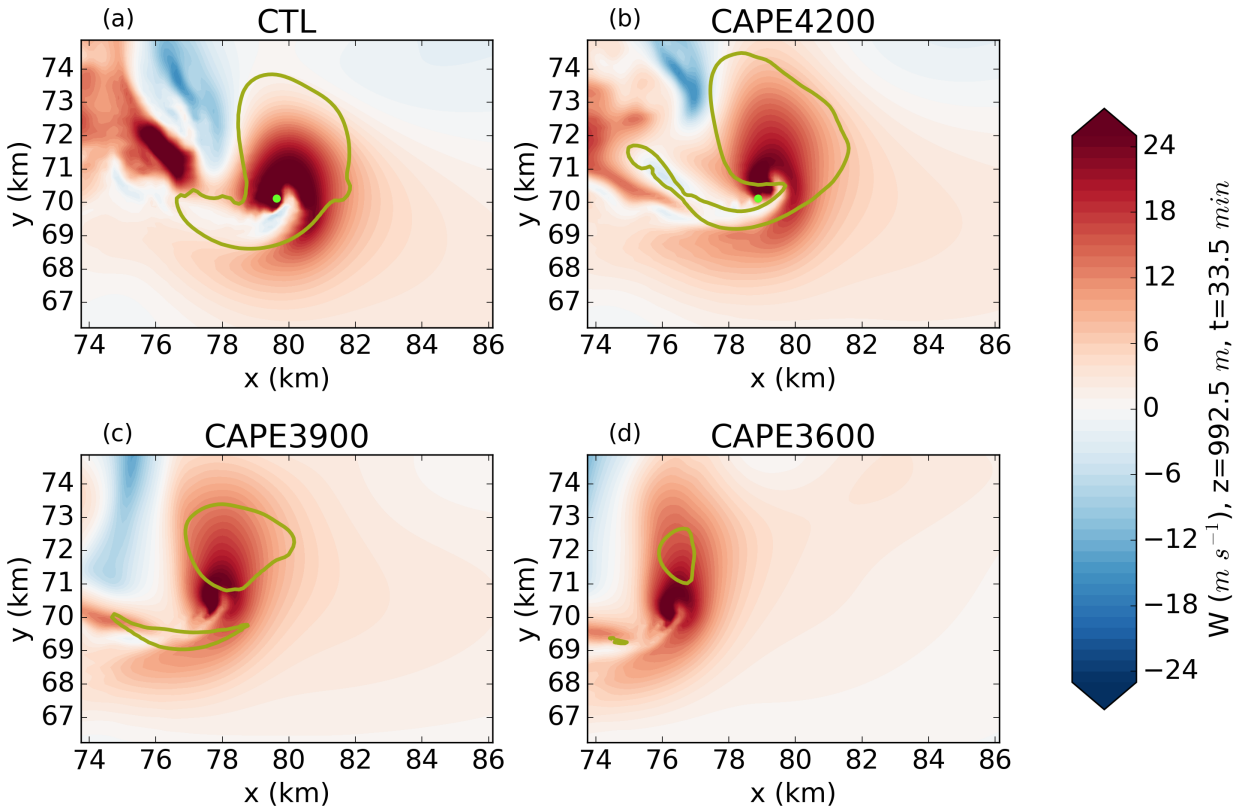

Figure 3.4. 1 km vertical velocity (m s^{-1}; shaded), 4.5 km updraft (25 m s^{-1} only; gold contour), and the location of the maximum ζ for simulations that have a tornado (green dot) at $t = 34\ mins$ for the CTL simulation and all three CAPE perturbation simulations.

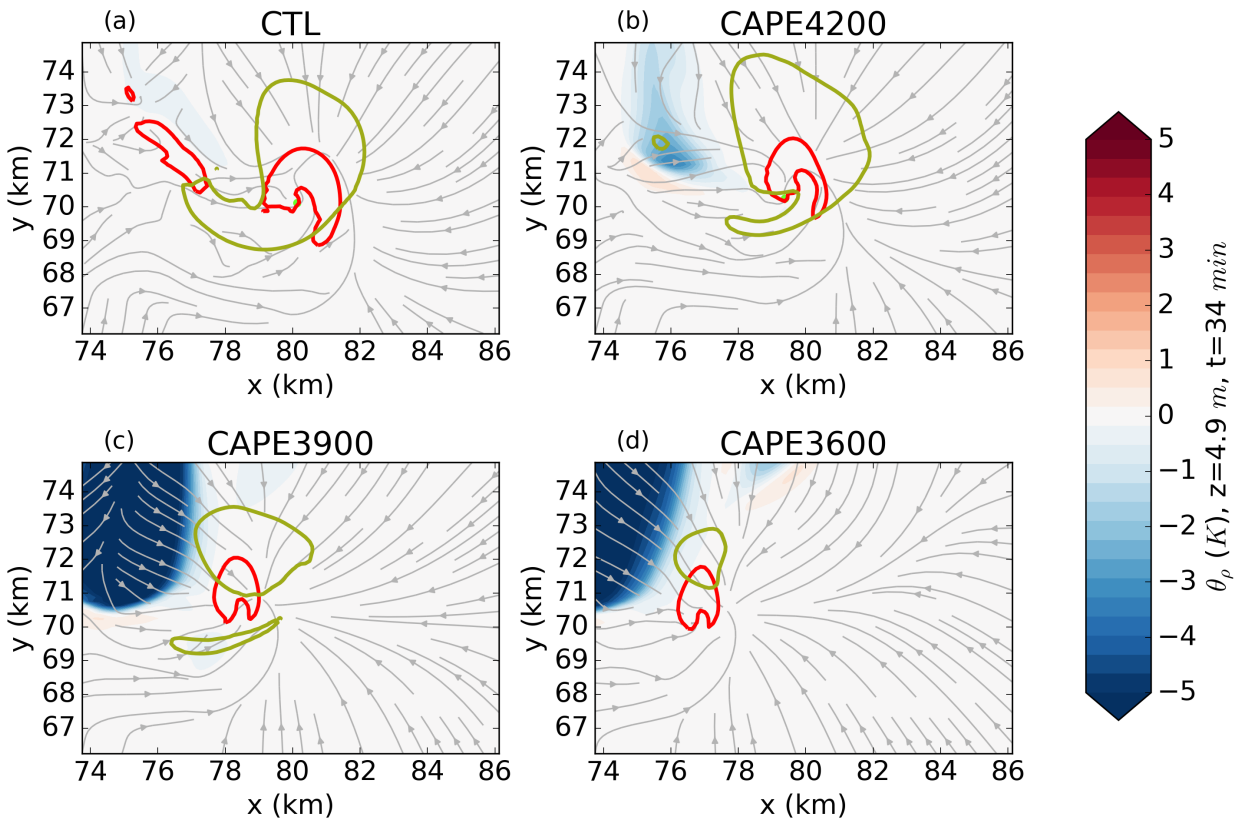

Figure 3.5. Perturbation (from initial conditions) θ_ρ at 5 m above the surface (as described in text, K), 4.5 km updraft contoured at 25 m s^{-1} (gold), 1 km updraft contoured at 20 m s^{-1} (red), and surface wind streamlines for the CTL case and all three CAPE perturbation simulations

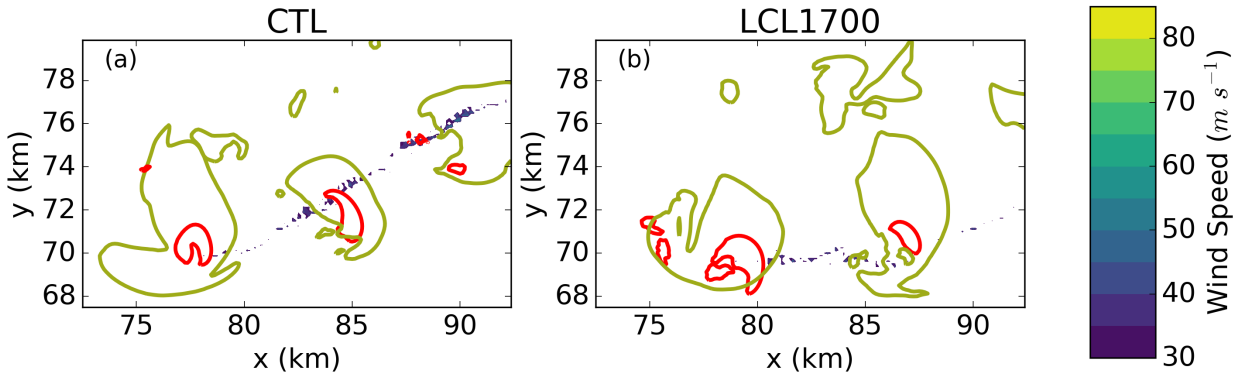

Figure 3.6. As in Figure 3.3, but for the CTL (LCL height of 1597 m) and LCL1700 (LCL height of 1797 m) case.

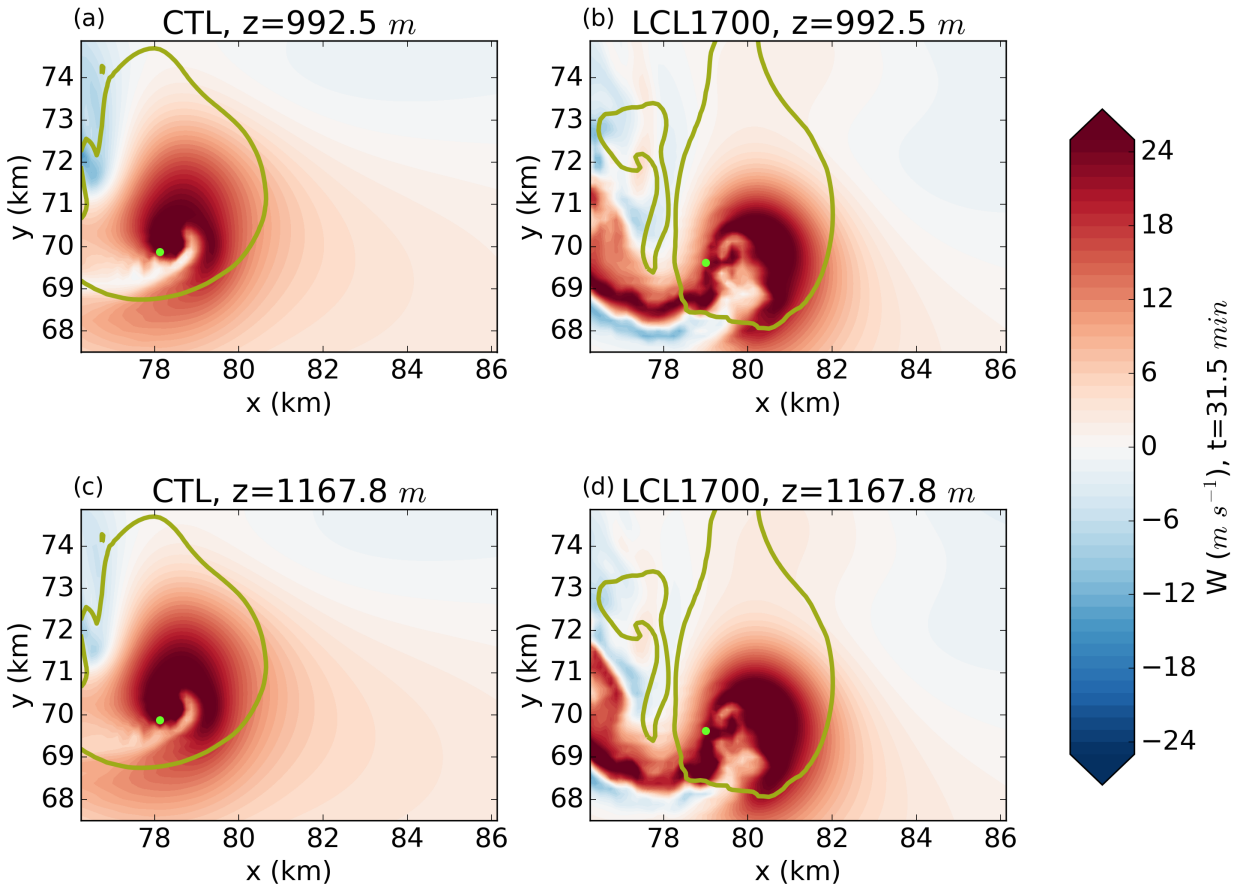

Figure 3.7. As in Figure 3.4 for the CTL (left) and LCL1700 (right) cases. The top two panels show vertical velocity at 1 km, the bottom two at 1.2 km.

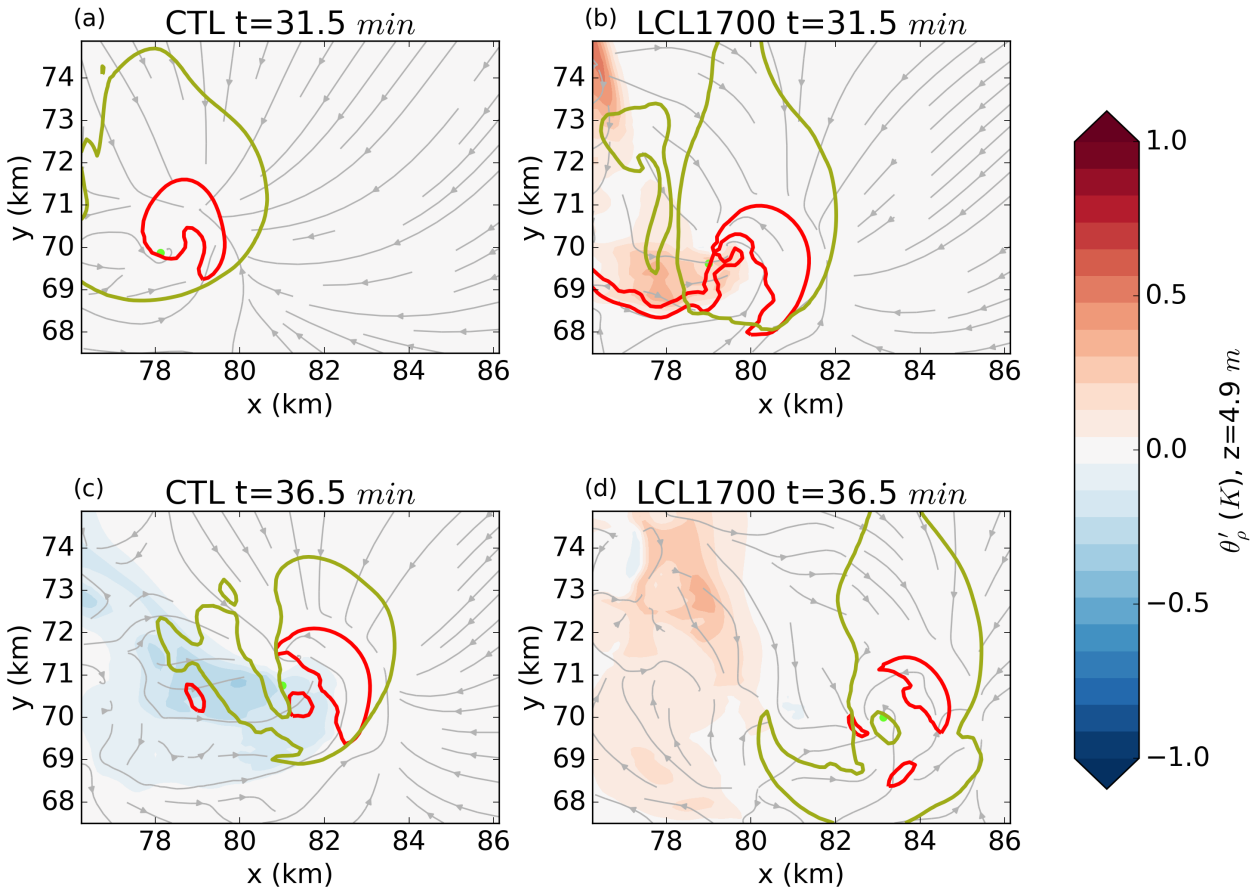

Figure 3.8. As in Figure 3.5 for the CTL (left) and LCL1700 (right) cases. The top two panels show θ'_ρ at 31.5 minutes after initialization, the bottom two panels show θ'_ρ at 36.5 minutes after initialization.

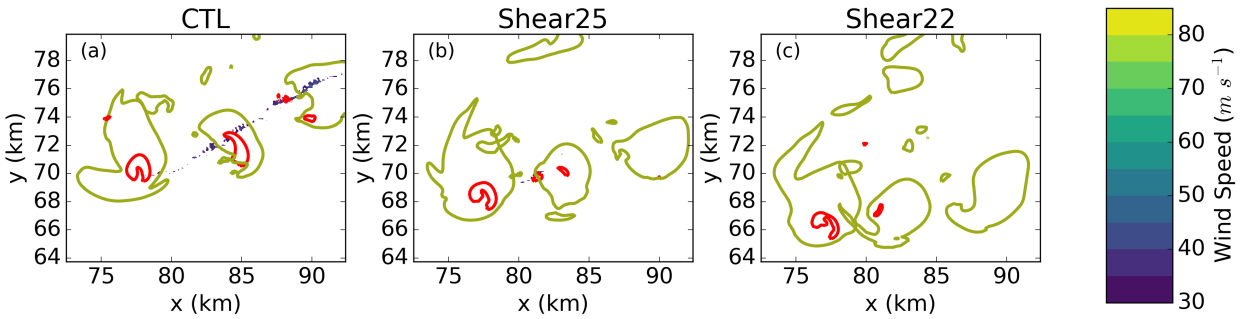

Figure 3.9. As in Figure 3.3 for the CTL case (0-1 km wind shear of 28 m s^{-1}) and Shear perturbation cases.

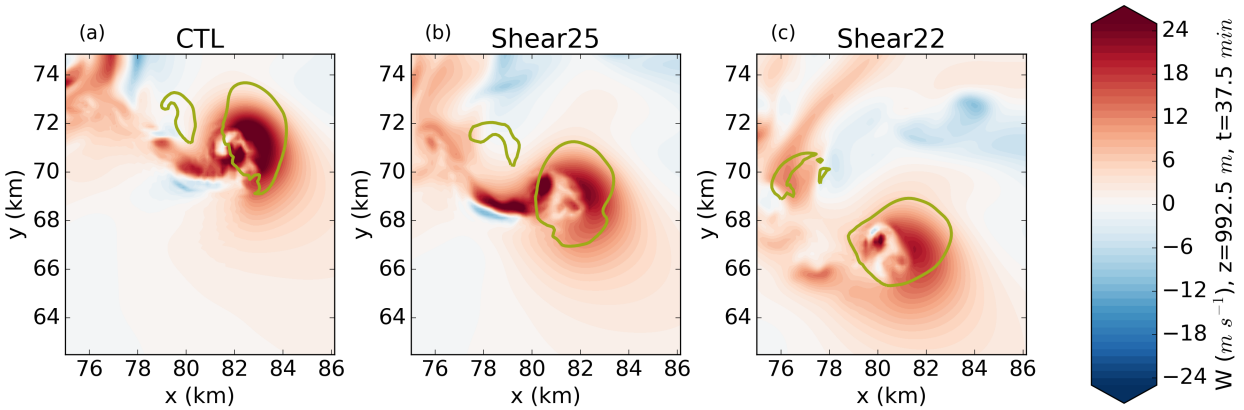

Figure 3.10. As in Figure 3.4 for the CTL case and Shear perturbation cases.

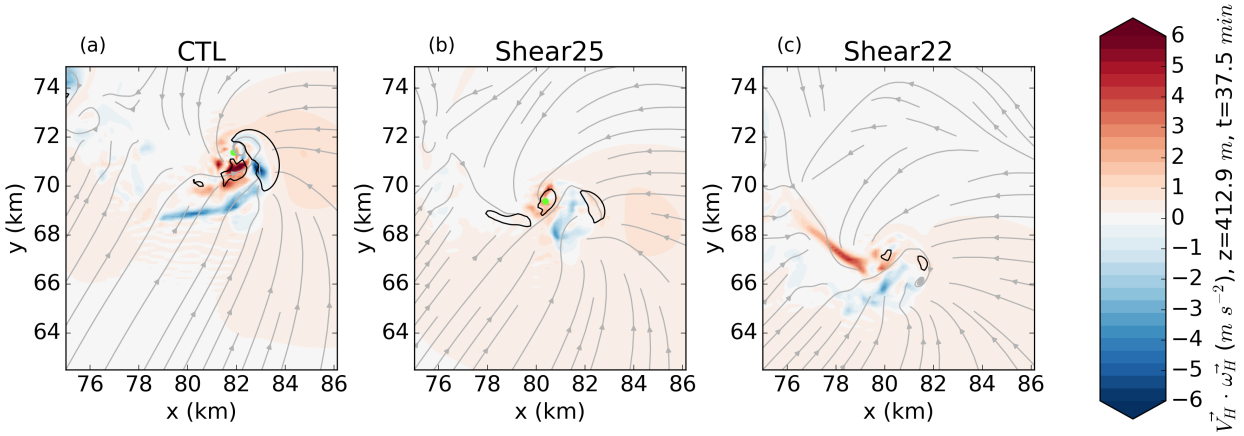

Figure 3.11. $\overrightarrow{V_H} \cdot \overrightarrow{\omega_H}$ (m s^{-2}, in shaded contours) at approximately 400 m above ground, where $\overrightarrow{V_H}$ is the horizontal wind vector and $\overrightarrow{\omega_H}$ is the horizontal vorticity vector, the winds at that level (grey streamlines), the updraft at 1 km (black outline, 20 m s^{-1}), and the location of the maximum vertical vorticity within the tornadic region (green dot) for the CTL case (left panel) and the two Shear perturbation cases (center and right panels).

CHAPTER 4: CONCLUSIONS

4.1. Summary of studies

Supercell thunderstorms have been observed and acknowledged for decades as strong storms that produce deadly and destructive hazards. However, our ability to forecast these hazards falls short due to both a lack of understanding of the processes that generate the hazards and a lack of observations of the environments that produce the storms. The overall goal of the research presented in this thesis has been to improve both process-level understanding and forecasts of these hazards associated with supercells. Improvements to the prediction of rainfall were examined in Chapter 2 by investigating the sensitivity of rainfall and rainfall processes to changes in (1) the shape parameter of the raindrop size distribution and (2) the collision efficiency of rain and cloud particles. Improvements to tornadogenesis forecasts were examined in Chapter 3 through examining supercell tornadogenesis sensitivity to environmental conditions, as well as the processes that lead to tornadogenesis within supercells.

The research presented in Chapter 2 indicated that forecast precipitation within supercell thunderstorms was strongly dependent on the *a priori* width of the raindrop size distribution and weakly dependent on the liquid collision efficiency dataset used. As the drop size distribution narrowed (which occurs when the shape parameter increases), the total rainfall that was produced decreased by up to 130% due to a) decreased rain production due to increased evaporation, b) slower raindrop fall speeds leading to longer residency time and changes in rain self-collection, and c) decreased rain production due to decreased ice melting. Wider DSDs were also found to result in increased hail precipitation at the surface. On the other hand, changing the collision efficiency dataset used did not change total rainfall substantially within the simulated supercell,

but it did change the processes that result in rain production, including changing the amount of rainfall produced by autoconversion of cloud and drizzle drops into rain. The results in Chapter 2 indicate that rainfall forecasts in supercells could potentially be improved, maybe significantly, by switching to a triple moment or bin representation of the microphysics, which do not rely on a fixed DSD width. This finding is particularly important for improving forecasts of flooding, as the substantial differences in predicted accumulated rainfall could differentiate whether a flood will occur or not.

The research presented in Chapter 3 investigated the processes that change in tornadic and nontornadic supercells when the initial environmental conditions are perturbed and examined why some supercells failed to produce tornadoes. Three sets of experiments were presented in Chapter 3, which modulated the CAPE, LCL, and low level wind shear of an initial control case. The results demonstrated that when reducing CAPE and low level wind shear, the environment can change from one that will support tornadic supercells to one that will only support nontornadic supercells. The results when modulating the LCL were more mixed, indicating only that as the LCL is raised, tornado strength decreases. When examining the processes in the Chapter 3 experiments, it appears that cold pool strength may have a strong modulating effect on tornadogenesis and tornado strength as first described in Markowski and Richardson (2013). This implies that tornado warnings could be improved by better and more frequent observations of cold pools and better understanding of cold pool processes. Although cold pool strength in this work was an influencing factor on tornadogenesis in the CAPE experiments and to a lesser degree in the LCL experiments, it did not explain the modulation of tornado strength with changing wind shear. Reducing the wind shear both reduces the updrafts and the horizontal

vorticity, reducing the amount of vertical vorticity that is able to be generated and therefore reducing the strength of the tornado.

Using the CAPE, LCL, and low level wind shear experiments presented in Chapter 3, it was determined that observational instrumentation could potentially add value in distinguishing between environments that will produce tornadic supercells from environments that will produce nontornadic supercells. However, any potential instrumentation would have to meet several accuracy thresholds to distinguish between tornadic and nontornadic environments. The experiments shown in Chapter 3 indicated that an instrument would need to observe CAPE to an accuracy of 300 J kg^{-1} and lower level wind shear to an accuracy of 3 m s^{-1} to distinguish between tornadic and nontornadic environments. Although current satellite platforms are able to observe CAPE to the required accuracy, no current satellites are able to observe low-level winds reliably. However, this research implies that with a sufficiently accurate retrieval platform that can obtain both thermodynamic and wind profiles, lead times for tornadogenesis forecasting can be improved.

In summary, this thesis has presented two major forecasting problems with supercells and has demonstrated possible solutions to address them. Rainfall forecasts within supercells could be greatly improved by improvements to models that reduce the number of *a priori* parameters selected, specifically removing the dependence on an *a priori* drop size distribution width. Supercell tornado forecasts could be improved by deploying more sufficiently accurate platforms that measure the environments that the supercells form in. Currently, existing platforms lack the ability to observe low-level winds at high spatial and temporal resolution. Developing instrumentation that is able to retrieve low-level wind shear at high accuracy and spatiotemporal resolution would be beneficial in tornado forecasting.

4.2. Future Work

In addition to the immediate improvements that can be made to supercell forecasting discussed in Chapters 2 and 3, this research raises many research questions for future work, some of which are listed below:

- How sensitive are other types of precipitation-generating systems to the rain drop size distribution width and the liquid collision efficiencies?
- How sensitive are precipitation and precipitation processes to the liquid collision efficiencies in bin microphysics schemes (which do not require a shape parameter)?
- Will predicting three moments of the rain drop size distribution alone improve rainfall forecasts or will rainfall forecasts be highly sensitive to other *a priori* parameters?
- Is it possible to diagnose a third moment of the rain drop size distribution from other predicted variables in a way that improves supercellular rain forecasts?
- How does tornadogenesis within supercells respond to different shapes of the temperature perturbation?
- Does the height of cloud base impact tornadogenesis substantially at all if moisture is kept the same in the boundary layer?

One of the important outcomes of the studies in this thesis is to acknowledge that while our understanding of supercells and the dynamic and microphysical processes that happen within them has improved in the 70 years since the Thunderstorm Project, more research still must be conducted on these storm systems. Given the danger of the hazards spawned by supercells, from tornadoes to floods to severe hail, it is important to continue to improve our understanding of severe thunderstorms through improved observations and more complex numerical models.

Improving our observations of supercells has been a theme of several recent field projects, including the 2016-2017 Colorado State University Convective Cloud Outflows and UpDrafts Experiment (C^3LOUD-Ex). The primary goals of C^3LOUD-Ex were to observe the updraft velocities and cold pools produced by convective storms, including supercells. As indicated in Chapter 3, both the updraft velocities and cold pool strengths play a role in modulating tornadogenesis. C^3LOUD-Ex has a rich dataset of *in situ* observations near supercells, including at least one weakly tornadic supercell. With detailed analysis, the C^3LOUD-Ex dataset could begin to answer some of the dynamical questions presented above. However, the C^3LOUD-Ex field campaign lacked detailed microphysical observations, as have many other supercell-focused campaigns, owing in part to the difficulty of getting instruments inside supercell thunderstorms. Some field campaigns have attempted to observe the microphysical development of strong convective storms above the surface using *in situ* instrumentation, however, these data are spatially and temporally limited and are further limited by the accuracy of aircraft-based instruments. Novel instrumentation, such as small Unmanned Aerial Systems (sUAS; also known as drones) can help to bridge this gap as they can fly into supercells without danger to any humans onboard. However, a number of technical and regulatory hurdles must be overcome to deploy instrumented sUAS into a supercell that will withstand the violent motions and large hail found within the storm.

While more observations will help to improve our understanding of supercellular structure, current instruments are unable to directly observe the microphysical and dynamic processes within the storms and thus present an incomplete picture of the storms. More advanced numerical models running at even finer resolutions than the two studies presented here will begin to provide better insight into small-scale supercellular processes. However, the results of higher

resolution simulations would still be subject to the assumptions about microphysical processes that are made, necessitating an approach that blends models and observations. Increasing our understanding of supercell processes and the small-scale microphysical and dynamical structure of supercells will improve forecasts by allowing for better developments of models and observational tools. Although full understanding of supercell structure and processes will require future observations and numerical models, the research presented in this thesis represents a step toward improving both process-level understanding and forecasting.

REFERENCES

Adams-Selin, R. D., S. C. van den Heever, and R. H. Johnson, 2012: Impact of Graupel Parameterization Schemes on Idealized Bow Echo Simulations. *Mon. Weather Rev.*, **141**, 1241–1262, doi:10.1175/MWR-D-12-00064.1. https://doi.org/10.1175/MWR-D-12-00064.1.

Adirosi, E., L. Baldini, F. Lombardo, F. Russo, F. Napolitano, E. Volpi, and A. Tokay, 2015: Comparison of different fittings of drop spectra for rainfall retrievals. *Adv. Water Resour.*, **83**, 55–67, doi:10.1016/j.advwatres.2015.05.009. http://www.sciencedirect.com/science/article/pii/S0309170815001025 (Accessed December 9, 2015).

——, E. Volpi, F. Lombardo, and L. Baldini, 2016: Raindrop size distribution: Fitting performance of common theoretical models. *Adv. Water Resour.*, **96**, 290–305, doi:10.1016/j.advwatres.2016.07.010.

Alexander, C., and Coauthors, 2016: The hourly updated US High-Resolution Rapid Refresh (HRRR) storm-scale forecast model. *Geophys. Res.Abst.*, **18**.

Ayala, O., B. Rosa, L.-P. Wang, and W. W. Grabowski, 2008: Effects of turbulence on the geometric collision rate of sedimenting droplets. Part 1. Results from direct numerical simulation. *New J. Phys.*, **10**, 75015, doi:10.1088/1367-2630/10/7/075015. http://stacks.iop.org/1367-2630/10/i=7/a=075015?key=crossref.d6de518161539b6bf42b1d7f7f4abeba (Accessed May 15, 2018).

Barth, M. C., and Coauthors, 2007: Cloud-scale model intercomparison of chemical constituent transport in deep convection. *Atmos. Chem. Phys.*, **7**, 4709–4731, doi:10.5194/acp-7-4709-2007. http://www.atmos-chem-phys.net/7/4709/2007/.

Barthlott, C., B. Mühr, and C. Hoose, 2017: Sensitivity of the 2014 Pentecost storms over Germany to different model grids and microphysics schemes. *Q. J. R. Meteorol. Soc.*, **143**, 1485–1503, doi:10.1002/qj.3019. https://doi.org/10.1002/qj.3019.

Beard, K. V., and H. T. Ochs, 1984: Collection and coalescence efficiencies for accretion. *J. Geophys. Res.*, **89**, 7165, doi:10.1029/JD089iD05p07165. http://doi.wiley.com/10.1029/JD089iD05p07165 (Accessed May 31, 2018).

Bessho, K., M. DeMaria, and J. A. Knaff, 2006: Tropical Cyclone Wind Retrievals from the Advanced Microwave Sounding Unit: Application to Surface Wind Analysis. *J. Appl. Meteorol. Climatol.*, **45**, 399–415, doi:10.1175/JAM2352.1. http://journals.ametsoc.org/doi/abs/10.1175/JAM2352.1 (Accessed September 4, 2018).

Bringi, V. N., C. R. Williams, M. Thurai, and P. T. May, 2009: Using Dual-Polarized Radar and Dual-Frequency Profiler for DSD Characterization: A Case Study from Darwin, Australia.

J. Atmos. Ocean. Technol., **26**, 2107–2122, doi:10.1175/2009JTECHA1258.1. http://dx.doi.org/10.1175/2009JTECHA1258.1.

Van Den Broeke, M. S., 2016: Polarimetric Variability of Classic Supercell Storms as a Function of Environment. *J. Appl. Meteorol. Climatol.*, **55**, 1907–1925, doi:10.1175/JAMC-D-15-0346.1. https://doi.org/10.1175/JAMC-D-15-0346.1.

Brooks, H. E., 2009: Proximity soundings for severe convection for Europe and the United States from reanalysis data. *Atmos. Res.*, **93**, 546–553, doi:10.1016/J.ATMOSRES.2008.10.005. https://www.sciencedirect.com/science/article/pii/S0169809508002858 (Accessed August 23, 2018).

Brooks, H. E., 2013: US ANNUAL TORNADO DEATH TOLLS, 1875-PRESENT. *NSSL Blog*,. https://blog.nssl.noaa.gov/nsslnews/2009/03/us-annual-tornado-death-tolls-1875-present/.

Brooks, H. E., C. A. Doswell III, and J. Cooper, 1994: On the Environments of Tornadic and Nontornadic Mesocyclones. *Weather Forecast.*, **9**, 606–618, doi:10.1175/1520-0434(1994)009<0606:OTEOTA>2.0.CO;2. http://journals.ametsoc.org/doi/abs/10.1175/1520-0434%281994%29009%3C0606%3AOTEOTA%3E2.0.CO%3B2 (Accessed August 2, 2018).

Brooks, H. E., J. W. Lee, and J. P. Craven, 2003: The spatial distribution of severe thunderstorm and tornado environments from global reanalysis data. *Atmos. Res.*, **67**–**68**, 73–94, doi:10.1016/S0169-8095(03)00045-0. https://www.sciencedirect.com/science/article/pii/S0169809503000450 (Accessed August 23, 2018).

Brotzge, J., S. Erickson, and H. Brooks, 2011: A 5-yr Climatology of Tornado False Alarms. *Weather Forecast.*, **26**, 534–544, doi:10.1175/WAF-D-10-05004.1. http://journals.ametsoc.org/doi/abs/10.1175/WAF-D-10-05004.1 (Accessed August 7, 2018).

Brotzge, J. A., S. E. Nelson, R. L. Thompson, B. T. Smith, J. A. Brotzge, S. E. Nelson, R. L. Thompson, and B. T. Smith, 2013: Tornado Probability of Detection and Lead Time as a Function of Convective Mode and Environmental Parameters. *Weather Forecast.*, **28**, 1261–1276, doi:10.1175/WAF-D-12-00119.1. http://journals.ametsoc.org/doi/abs/10.1175/WAF-D-12-00119.1 (Accessed August 4, 2017).

Brown, B. R., M. M. Bell, and A. J. Frambach, 2016: Validation of simulated hurricane drop size distributions using polarimetric radar. *Geophys. Res. Lett.*, **43**, 910–917, doi:10.1002/2015GL067278. http://doi.wiley.com/10.1002/2015GL067278 (Accessed May 16, 2018).

Browning, K. A., 1964: Airflow and Precipitation Trajectories Within Severe Local Storms Which Travel to the Right of the Winds. *J. Atmos. Sci.*, **21**, 634–639, doi:10.1175/1520-0469(1964)021<0634:AAPTWS>2.0.CO;2.

http://journals.ametsoc.org/doi/abs/10.1175/1520-0469%281964%29021%3C0634%3AAAPTWS%3E2.0.CO%3B2 (Accessed September 4, 2018).

Bryan, G. H., and H. Morrison, 2012: Sensitivity of a Simulated Squall Line to Horizontal Resolution and Parameterization of Microphysics. *Mon. Weather Rev.*, **140**, 202–225, doi:10.1175/MWR-D-11-00046.1. http://journals.ametsoc.org/doi/abs/10.1175/MWR-D-11-00046.1 (Accessed June 19, 2018).

Bunkers, M. J., and Coauthors, 2000: Predicting Supercell Motion Using a New Hodograph Technique. *Weather Forecast.*, **15**, 61–79, doi:10.1175/1520-0434(2000)015<0061:PSMUAN>2.0.CO;2. http://journals.ametsoc.org/doi/abs/10.1175/1520-0434%282000%29015%3C0061%3APSMUAN%3E2.0.CO%3B2 (Accessed August 24, 2018).

Byers, H. R., and R. R. Braham, 1948: THUNDERSTORM STRUCTURE AND CIRCULATION. *J. Meteorol.*, **5**, 71–86, doi:10.1175/1520-0469(1948)005<0071:TSAC>2.0.CO;2. http://journals.ametsoc.org/doi/abs/10.1175/1520-0469%281948%29005%3C0071%3ATSAC%3E2.0.CO%3B2 (Accessed August 28, 2018).

Byko, Z., P. Markowski, Y. Richardson, J. Wurman, and E. Adlerman, 2009: Descending Reflectivity Cores in Supercell Thunderstorms Observed by Mobile Radars and in a High-Resolution Numerical Simulation. *Weather Forecast.*, **24**, 155–186, doi:10.1175/2008WAF2222116.1. http://journals.ametsoc.org/doi/abs/10.1175/2008WAF2222116.1 (Accessed September 12, 2018).

Cao, Q., G. Zhang, E. Brandes, T. Schuur, A. Ryzhkov, and K. Ikeda, 2008: Analysis of Video Disdrometer and Polarimetric Radar Data to Characterize Rain Microphysics in Oklahoma. *J. Appl. Meteorol. Climatol.*, **47**, 2238–2255, doi:10.1175/2008JAMC1732.1. http://dx.doi.org/10.1175/2008JAMC1732.1.

Coffer, B. E., and M. D. Parker, 2016: Simulated Supercells in Nontornadic and Tornadic VORTEX2 Environments. *Mon. Weather Rev.*, **145**, 149–180, doi:10.1175/MWR-D-16-0226.1. https://doi.org/10.1175/MWR-D-16-0226.1.

Coffer, B. E., and M. D. Parker, 2018: Is There a "Tipping Point" between Simulated Nontornadic and Tornadic Supercells in VORTEX2 Environments? *Mon. Weather Rev.*, **146**, 2667–2693, doi:10.1175/MWR-D-18-0050.1. http://journals.ametsoc.org/doi/10.1175/MWR-D-18-0050.1 (Accessed August 6, 2018).

Cohard, J.-M., and J.-P. Pinty, 2000: A comprehensive two-moment warm microphysical bulk scheme. I: Description and tests. *Q. J. R. Meteorol. Soc.*, **126**, 1815–1842, doi:10.1002/qj.49712656613. http://doi.wiley.com/10.1002/qj.49712656613 (Accessed September 2, 2016).

Cohen, C., and E. W. McCaul, 2006: The Sensitivity of Simulated Convective Storms to

Variations in Prescribed Single-Moment Microphysics Parameters that Describe Particle Distributions, Sizes, and Numbers. *Mon. Weather Rev.*, **134**, 2547–2565, doi:10.1175/MWR3195.1. http://dx.doi.org/10.1175/MWR3195.1.

Cotton, W. R., and Coauthors, 2003a: RAMS 2001: Current status and future directions. *Meteorol. Atmos. Phys.*, **82**, 5–29, doi:10.1007/s00703-001-0584-9. http://www.springerlink.com/Index/10.1007/s00703-001-0584-9.

Cotton, W. R., and Coauthors, 2003b: RAMS 2001: Current status and future directions. *Meteorol. Atmos. Phys.*, **82**, 5–29, doi:10.1007/s00703-001-0584-9. http://193.144.100.163/meteorologia/DOCS/BIBLIOGRAFIA/METATMPHYS-cottonrams.pdf.

Ćurić, M., D. Janc, and K. Veljović, 2010: Dependence of accumulated precipitation on cloud drop size distribution. *Theor. Appl. Climatol.*, **102**, 471–481, doi:10.1007/s00704-010-0332-5. http://dx.doi.org/10.1007/s00704-010-0332-5.

Davies-Jones, R., 2015: A review of supercell and tornado dynamics. *Atmos. Res.*, **158**–**159**, 274–291, doi:10.1016/j.atmosres.2014.04.007. http://www.sciencedirect.com/science/article/pii/S0169809514001756 (Accessed August 19, 2015).

Davis, M. H., 1972: Collisions of Small Cloud Droplets: Gas Kinetic Effects. *J. Atmos. Sci.*, **29**, 911–915, doi:10.1175/1520-0469(1972)029<0911:COSCDG>2.0.CO;2. https://doi.org/10.1175/1520-0469(1972)029%3C0911:COSCDG%3E2.0.CO.

Dennis, E. J., and M. R. Kumjian, 2017: The Impact of Vertical Wind Shear on Hail Growth in Simulated Supercells. *J. Atmos. Sci.*, **74**, 641–663, doi:10.1175/JAS-D-16-0066.1. http://journals.ametsoc.org/doi/10.1175/JAS-D-16-0066.1 (Accessed August 6, 2018).

Dolan, B., B. Fuchs, S. A. Rutledge, E. A. Barnes, and E. J. Thompson, 2018: Primary Modes of Global Drop Size Distributions. *J. Atmos. Sci.*, **75**, 1453–1476, doi:10.1175/JAS-D-17-0242.1. http://journals.ametsoc.org/doi/10.1175/JAS-D-17-0242.1 (Accessed October 16, 2018).

Doswell, C. A., and J. S. Evans, 2003: Proximity sounding analysis for derechos and supercells: an assessment of similarities and differences. *Atmos. Res.*, **67**–**68**, 117–133, doi:10.1016/S0169-8095(03)00047-4. https://www.sciencedirect.com/science/article/pii/S0169809503000474 (Accessed August 2, 2018).

Federico, S., E. Avolio, M. Petracca, G. Panegrossi, P. Sanò, D. Casella, and S. Dietrich, 2014: Simulating lightning into the RAMS model: implementation and preliminary results. *Nat. Hazards Earth Syst. Sci.*, **14**, 2933–2950, doi:10.5194/nhess-14-2933-2014. http://www.nat-hazards-earth-syst-sci.net/14/2933/2014/.

Feingold, G., S. Tzivion (Tzitzvashvili), and Z. Leviv, 1988: Evolution of Raindrop Spectra. Part I: Solution to the Stochastic Collection/Breakup Equation Using the Method of Moments. *J.*

Atmos. Sci., **45**, 3387–3399, doi:10.1175/1520-0469(1988)045<3387:EORSPI>2.0.CO;2. https://doi.org/10.1175/1520-0469(1988)045%3C3387:EORSPI%3E2.0.CO.

——, R. L. Walko, B. Stevens, and W. R. Cotton, 1998: Simulations of marine stratocumulus using a new microphysical parameterization scheme. *Atmos. Res.*, **47**–**48**, 505–528, doi:10.1016/S0169-8095(98)00058-1. https://www.sciencedirect.com/science/article/pii/S0169809598000581 (Accessed July 17, 2018).

Freud, E., D. Rosenfeld, M. O. Andreae, A. A. Costa, and P. Artaxo, 2008: Robust relations between CCN and the vertical evolution of cloud drop size distribution in deep convective clouds. *Atmos. Chem. Phys.*, **8**, 1661–1675, doi:10.5194/acp-8-1661-2008. http://www.atmos-chem-phys.net/8/1661/2008/.

Friedrich, K., E. a. Kalina, J. Aikins, M. Steiner, D. Gochis, P. a. Kucera, K. Ikeda, and J. Sun, 2015: Raindrop size distribution and rain characteristics during the 2013 Great Colorado Flood. *J. Hydrometeorol.*, 150526130654002, doi:10.1175/JHM-D-14-0184.1. http://journals.ametsoc.org/doi/abs/10.1175/JHM-D-14-0184.1.

Gaudet, B. J., and W. R. Cotton, 2006: Low-Level Mesocyclonic Concentration by Nonaxisymmetric Transport. Part I: Supercell and Mesocyclone Evolution. *J. Atmos. Sci.*, **63**, 1113–1133, doi:10.1175/JAS3685.1. http://dx.doi.org/10.1175/JAS3685.1.

——, ——, and M. T. Montgomery, 2006: Low-Level Mesocyclonic Concentration by Nonaxisymmetric Transport. Part II: Vorticity Dynamics. *J. Atmos. Sci.*, **63**, 1134–1150, doi:10.1175/JAS3579.1. http://dx.doi.org/10.1175/JAS3579.1.

Gilmore, M. S., J. M. Straka, and E. N. Rasmussen, 2004a: Precipitation and Evolution Sensitivity in Simulated Deep Convective Storms: Comparisons between Liquid-Only and Simple Ice and Liquid Phase Microphysics*. *Mon. Weather Rev.*, **132**, 1897–1916, doi:10.1175/1520-0493(2004)132<1897:PAESIS>2.0.CO;2. http://journals.ametsoc.org/doi/abs/10.1175/1520-0493%282004%29132%3C1897%3APAESIS%3E2.0.CO%3B2 (Accessed June 19, 2018).

Gilmore, M. S., J. M. Straka, and E. N. Rasmussen, 2004b: Precipitation Uncertainty Due to Variations in Precipitation Particle Parameters within a Simple Microphysics Scheme. *Mon. Weather Rev.*, **132**, 2610–2627, doi:10.1175/MWR2810.1. http://dx.doi.org/10.1175/MWR2810.1.

Gonçalves, F. L. T., J. A. Martins, and M. A. Silva Dias, 2008: Shape parameter analysis using cloud spectra and gamma functions in the numerical modeling RAMS during LBA Project at Amazonian region, Brazil. *Atmos. Res.*, **89**, 1–11, doi:10.1016/j.atmosres.2007.12.005.

Grant, L. D., and S. C. van den Heever, 2014: Microphysical and Dynamical Characteristics of Low-Precipitation and Classic Supercells. *J. Atmos. Sci.*, **71**, 2604–2624, doi:10.1175/JAS-D-13-0261.1. http://dx.doi.org/10.1175/JAS-D-13-0261.1.

Grasso, L. D., 2000: The Dissipation of a Left-Moving Cell in a Severe Storm Environment.

Mon. Weather Rev., **128**, 2797–2815, doi:10.1175/1520-0493(2000)128<2797:TDOALM>2.0.CO;2. http://dx.doi.org/10.1175/1520-0493(2000)128%3C2797:TDOALM%3E2.0.CO.

Grubišić, V., R. K. Vellore, and A. W. Huggins, 2005: Quantitative Precipitation Forecasting of Wintertime Storms in the Sierra Nevada: Sensitivity to the Microphysical Parameterization and Horizontal Resolution. *Mon. Weather Rev.*, **133**, 2834–2859, doi:10.1175/MWR3004.1. http://journals.ametsoc.org/doi/abs/10.1175/MWR3004.1 (Accessed June 19, 2018).

Hall, W. D., 1980: A Detailed Microphysical Model Within a Two-Dimensional Dynamic Framework: Model Description and Preliminary Results. *J. Atmos. Sci.*, **37**, 2486–2507, doi:10.1175/1520-0469(1980)037<2486:ADMMWA>2.0.CO;2. https://doi.org/10.1175/1520-0469(1980)037%3C2486:ADMMWA%3E2.0.CO.

Heymsfield, A. J., A. Bansemer, M. R. Poellot, and N. Wood, 2015: Observations of Ice Microphysics through the Melting Layer. *J. Atmos. Sci.*, **72**, 2902–2928, doi:10.1175/JAS-D-14-0363.1. http://dx.doi.org/10.1175/JAS-D-14-0363.1.

Hsieh, W. C., H. Jonsson, L.-P. Wang, R. C. Flagan, J. H. Seinfeld, A. Nenes, and G. Buzorius, 2009: On the representation of droplet coalescence and autoconversion: Evaluation using ambient cloud droplet size distributions. https://calhoun.nps.edu/handle/10945/42257.

Igel, A. L., and S. C. van den Heever, 2016: The importance of the cloud droplet size distributions in shallow cumulus clouds. Part II: Macrophysical and optical properties. *J. Atmos. Sci.*,.

——, and ——, 2017a: The Importance of the Shape of Cloud Droplet Size Distributions in Shallow Cumulus Clouds. Part II: Bulk Microphysics Simulations. *J. Atmos. Sci.*, **74**, 259–273, doi:10.1175/JAS-D-15-0383.1.

——, and ——, 2017b: The Importance of the Shape of Cloud Droplet Size Distributions in Shallow Cumulus Clouds. Part I: Bin Microphysics Simulations. *J. Atmos. Sci.*, **74**, 249–258, doi:10.1175/JAS-D-15-0382.1. http://dx.doi.org/10.1175/JAS-D-15-0382.1.

——, M. R. Igel, and S. C. van den Heever, 2014: Make It a Double? Sobering Results from Simulations Using Single-Moment Microphysics Schemes. *J. Atmos. Sci.*, **72**, 910–925, doi:10.1175/JAS-D-14-0107.1. http://dx.doi.org/10.1175/JAS-D-14-0107.1.

Jonas, P. R., 1972: The collision efficiency of small drops. *Q. J. R. Meteorol. Soc.*, **98**, 681–683, doi:10.1002/qj.49709841717. https://doi.org/10.1002/qj.49709841717.

Kessler, E., 1969: On the Distribution and Continuity of Water Substance in Atmospheric Circulations BT - On the Distribution and Continuity of Water Substance in Atmospheric Circulations. E. Kessler, Ed., American Meteorological Society, Boston, MA, 1–84 https://doi.org/10.1007/978-1-935704-36-2_1.

Khain, A. P., and Coauthors, 2015: Representation of microphysical processes in cloud-resolving models: Spectral (bin) microphysics versus bulk parameterization. *Rev. Geophys.*, **53**, 247–

322, doi:10.1002/2014RG000468. http://doi.wiley.com/10.1002/2014RG000468 (Accessed August 10, 2017).

Klees, A. M., Y. P. Richardson, P. M. Markowski, C. Weiss, J. M. Wurman, and K. K. Kosiba, 2016: Comparison of the Tornadic and Nontornadic Supercells Intercepted by VORTEX2 on 10 June 2010. *Mon. Weather Rev.*, **144**, 3201–3231, doi:10.1175/MWR-D-15-0345.1. http://journals.ametsoc.org/doi/10.1175/MWR-D-15-0345.1 (Accessed August 7, 2018).

Klett, J. D., and M. H. Davis, 1973: Theoretical Collision Efficiencies of Cloud Droplets at Small Reynolds Numbers. *J. Atmos. Sci.*, **30**, 107–117, doi:10.1175/1520-0469(1973)030<0107:TCEOCD>2.0.CO;2. https://doi.org/10.1175/1520-0469(1973)030%3C0107:TCEOCD%3E2.0.CO.

Kumjian, M. R., and A. V Ryzhkov, 2008: Polarimetric Signatures in Supercell Thunderstorms. *J. Appl. Meteorol. Climatol.*, **47**, 1940–1961, doi:10.1175/2007JAMC1874.1. https://doi.org/10.1175/2007JAMC1874.1.

Lang, S. E., and Coauthors, 2014: Benefits of a Fourth Ice Class in the Simulated Radar Reflectivities of Convective Systems Using a Bulk Microphysics Scheme. *J. Atmos. Sci.*, **71**, 3583–3612, doi:10.1175/JAS-D-13-0330.1. http://journals.ametsoc.org/doi/abs/10.1175/JAS-D-13-0330.1 (Accessed May 16, 2018).

Lebo, Z. J., and J. H. Seinfeld, 2011: Theoretical basis for convective invigoration due to increased aerosol concentration. *Atmos. Chem. Phys.*, **11**, 5407–5429, doi:10.5194/acp-11-5407-2011. http://www.atmos-chem-phys.net/11/5407/2011/.

Lemon, L. R., and C. A. Doswell, 1979: Severe Thunderstorm Evolution and Mesocyclone Structure as Related to Tornadogenesis. *Mon. Weather Rev.*, **107**, 1184–1197, doi:10.1175/1520-0493(1979)107<1184:STEAMS>2.0.CO;2. http://journals.ametsoc.org/doi/abs/10.1175/1520-0493%281979%29107%3C1184%3ASTEAMS%3E2.0.CO%3B2 (Accessed September 6, 2018).

Lerach, D. G., and W. R. Cotton, 2011: Comparing Aerosol and Low-Level Moisture Influences on Supercell Tornadogenesis: Three-Dimensional Idealized Simulations. *J. Atmos. Sci.*, **69**, 969–987, doi:10.1175/JAS-D-11-043.1. http://dx.doi.org/10.1175/JAS-D-11-043.1.

——, B. J. Gaudet, and W. R. Cotton, 2008: Idealized simulations of aerosol influences on tornadogenesis. *Geophys. Res. Lett.*, **35**, n/a-n/a, doi:10.1029/2008GL035617. http://dx.doi.org/10.1029/2008GL035617.

Lim, K.-S. S., and S.-Y. Hong, 2009: Development of an Effective Double-Moment Cloud Microphysics Scheme with Prognostic Cloud Condensation Nuclei (CCN) for Weather and Climate Models. *Mon. Weather Rev.*, **138**, 1587–1612, doi:10.1175/2009MWR2968.1. http://dx.doi.org/10.1175/2009MWR2968.1.

Lin, C. L., and S. C. Lee, 1975: Collision Efficiency of Water Drops in the Atmosphere. *J. Atmos. Sci.*, **32**, 1412–1418, doi:10.1175/1520-0469(1975)032<1412:CEOWDI>2.0.CO;2.

https://doi.org/10.1175/1520-0469(1975)032%3C1412:CEOWDI%3E2.0.CO.

Liu, Y., and P. H. Daum, 2004: Parameterization of the Autoconversion Process.Part I: Analytical Formulation of the Kessler-Type Parameterizations. *J. Atmos. Sci.*, **61**, 1539–1548, doi:10.1175/1520-0469(2004)061<1539:POTAPI>2.0.CO;2. http://journals.ametsoc.org/doi/abs/10.1175/1520-0469%282004%29061%3C1539%3APOTAPI%3E2.0.CO%3B2 (Accessed July 16, 2018).

Loftus, A. M., and W. R. Cotton, 2014: A triple-moment hail bulk microphysics scheme. Part II: Verification and comparison with two-moment bulk microphysics. *Atmos. Res.*, **150**, 97–128, doi:10.1016/j.atmosres.2014.07.016. http://www.sciencedirect.com/science/article/pii/S0169809514002798 (Accessed November 12, 2015).

Loftus, A. M., D. B. Weber, and C. A. Doswell, 2008: Parameterized Mesoscale Forcing Mechanisms for Initiating Numerically Simulated Isolated Multicellular Convection. *Mon. Weather Rev.*, **136**, 2408–2421, doi:10.1175/2007MWR2133.1. http://dx.doi.org/10.1175/2007MWR2133.1.

Loftus, A. M., W. R. Cotton, and G. G. Carrió, 2014: A triple-moment hail bulk microphysics scheme. Part I: Description and initial evaluation. *Atmos. Res.*, **149**, 35–57, doi:10.1016/j.atmosres.2014.05.013. http://www.sciencedirect.com/science/article/pii/S0169809514002142 (Accessed November 12, 2015).

Long, A. B., 1974: Solutions to the Droplet Collection Equation for Polynomial Kernels. *J. Atmos. Sci.*, **31**, 1040–1052, doi:10.1175/1520-0469(1974)031<1040:STTDCE>2.0.CO;2. https://doi.org/10.1175/1520-0469(1974)031%3C1040:STTDCE%3E2.0.CO.

Low, T. B., and R. List, 1982: Collision, Coalescence and Breakup of Raindrops. Part I: Experimentally Established Coalescence Efficiencies and Fragment Size Distributions in Breakup. *J. Atmos. Sci.*, **39**, 1591–1606, doi:10.1175/1520-0469(1982)039<1591:CCABOR>2.0.CO;2. https://doi.org/10.1175/1520-0469(1982)039%3C1591:CCABOR%3E2.0.CO.

Maddy, E. S., and C. D. Barnet, 2008: Vertical Resolution Estimates in Version 5 of AIRS Operational Retrievals. *IEEE Trans. Geosci. Remote Sens.*, **46**, 2375–2384, doi:10.1109/TGRS.2008.917498. http://ieeexplore.ieee.org/document/4578827/ (Accessed September 12, 2018).

Markowski, P. M., and Y. P. Richardson, 2009: Tornadogenesis: Our current understanding, forecasting considerations, and questions to guide future research. *Atmos. Res.*, **93**, 3–10, doi:10.1016/j.atmosres.2008.09.015. http://www.sciencedirect.com/science/article/pii/S016980950800255X (Accessed September 24, 2015).

Markowski, P. M., and Y. P. Richardson, 2013: The Influence of Environmental Low-Level Shear and Cold Pools on Tornadogenesis: Insights from Idealized Simulations. *J. Atmos.*

Sci., **71**, 243–275, doi:10.1175/JAS-D-13-0159.1. http://dx.doi.org/10.1175/JAS-D-13-0159.1.

——, Y. Richardson, M. Majcen, J. Marquis, and J. Wurman, 2011: Characteristics of the wind field in three nontornadic low-level mesocyclones observed by the Doppler on Wheels radars. *E-Journal Sev. Storms Meteorol.*, **6**.

Marshall, J. S., and W. M. K. Palmer, 1948: The Distribution of Raindrops with Size. *J. Meteorol.*, **5**, 165–166, doi:10.1175/1520-0469(1948)005<0165:TDORWS>2.0.CO;2. http://dx.doi.org/10.1175/1520-0469(1948)005%3C0165:TDORWS%3E2.0.CO.

McCaul, E. W., and M. L. Weisman, 2001: The Sensitivity of Simulated Supercell Structure and Intensity to Variations in the Shapes of Environmental Buoyancy and Shear Profiles. *Mon. Weather Rev.*, **129**, 664–687, doi:10.1175/1520-0493(2001)129<0664:TSOSSS>2.0.CO;2. http://journals.ametsoc.org/doi/abs/10.1175/1520-0493%282001%29129%3C0664%3ATSOSSS%3E2.0.CO%3B2 (Accessed August 20, 2018).

Meyers, M. P., R. L. Walko, J. Y. Harrington, and W. R. Cotton, 1997: New RAMS cloud microphysics parameterization. Part II: The two-moment scheme. *Atmos. Res.*, **45**, 3–39, doi:10.1016/S0169-8095(97)00018-5. http://linkinghub.elsevier.com/retrieve/pii/S0169809597000185 (Accessed August 18, 2016).

Milbrandt, J. A., and M. K. Yau, 2005a: A Multimoment Bulk Microphysics Parameterization. Part I: Analysis of the Role of the Spectral Shape Parameter. *J. Atmos. Sci.*, **62**, 3051–3064, doi:10.1175/JAS3534.1. http://dx.doi.org/10.1175/JAS3534.1.

——, and ——, 2005b: A Multimoment Bulk Microphysics Parameterization. Part II: A Proposed Three-Moment Closure and Scheme Description. *J. Atmos. Sci.*, **62**, 3065–3081, doi:10.1175/JAS3535.1. http://dx.doi.org/10.1175/JAS3535.1.

——, and ——, 2006: A Multimoment Bulk Microphysics Parameterization. Part IV: Sensitivity Experiments. *J. Atmos. Sci.*, **63**, 3137–3159, doi:10.1175/JAS3817.1. http://dx.doi.org/10.1175/JAS3817.1.

——, and R. McTaggart-Cowan, 2010: Sedimentation-Induced Errors in Bulk Microphysics Schemes. *J. Atmos. Sci.*, **67**, 3931–3948, doi:10.1175/2010JAS3541.1. https://doi.org/10.1175/2010JAS3541.1.

Milbrandt, J. A., S. Bélair, M. Faucher, M. Vallée, M. L. Carrera, and A. Glazer, 2016: The Pan-Canadian High Resolution (2.5 km) Deterministic Prediction System. *Weather Forecast.*, **31**, 1791–1816, doi:10.1175/WAF-D-16-0035.1. https://doi.org/10.1175/WAF-D-16-0035.1.

Morrison, H., and J. Milbrandt, 2010: Comparison of Two-Moment Bulk Microphysics Schemes in Idealized Supercell Thunderstorm Simulations. *Mon. Weather Rev.*, **139**, 1103–1130, doi:10.1175/2010MWR3433.1. http://dx.doi.org/10.1175/2010MWR3433.1.

——, and J. A. Milbrandt, 2015: Parameterization of Cloud Microphysics Based on the Prediction of Bulk Ice Particle Properties. Part I: Scheme Description and Idealized Tests. *J. Atmos. Sci.*, **72**, 287–311, doi:10.1175/JAS-D-14-0065.1. http://journals.ametsoc.org/doi/10.1175/JAS-D-14-0065.1 (Accessed July 17, 2018).

——, W. W. Grabowski, H. Morrison, and W. W. Grabowski, 2007: Comparison of Bulk and Bin Warm-Rain Microphysics Models Using a Kinematic Framework. *J. Atmos. Sci.*, **64**, 2839–2861, doi:10.1175/JAS3980. http://journals.ametsoc.org/doi/abs/10.1175/JAS3980 (Accessed July 17, 2018).

Morrison, H., G. Thompson, and V. Tatarskii, 2009: Impact of Cloud Microphysics on the Development of Trailing Stratiform Precipitation in a Simulated Squall Line: Comparison of One- and Two-Moment Schemes. *Mon. Weather Rev.*, **137**, 991–1007, doi:10.1175/2008MWR2556.1. http://dx.doi.org/10.1175/2008MWR2556.1.

Nair, U. S., Y. Wu, C. D. Holmes, A. Ter Schure, G. Kallos, and J. T. Walters, 2013: Cloud-resolving simulations of mercury scavenging and deposition in thunderstorms. *Atmos. Chem. Phys.*, **13**, 10143–10157, doi:10.5194/acp-13-10143-2013. http://www.atmos-chem-phys.net/13/10143/2013/.

Naumann, A. K., and A. Seifert, 2016: Evolution of the Shape of the Raindrop Size Distribution in Simulated Shallow Cumulus. *J. Atmos. Sci.*, **73**, 2279–2297, doi:10.1175/JAS-D-15-0263.1. https://doi.org/10.1175/JAS-D-15-0263.1.

Niu, S., X. Jia, J. Sang, X. Liu, C. Lu, and Y. Liu, 2009: Distributions of Raindrop Sizes and Fall Velocities in a Semiarid Plateau Climate: Convective versus Stratiform Rains. *J. Appl. Meteorol. Climatol.*, **49**, 632–645, doi:10.1175/2009JAMC2208.1. http://dx.doi.org/10.1175/2009JAMC2208.1.

Ochs, H. T., and K. V Beard, 1984: Laboratory Measurements of Collection Efficiencies for Accretion. *J. Atmos. Sci.*, **41**, 863–867, doi:10.1175/1520-0469(1984)041<0863:LMOCEF>2.0.CO;2. https://doi.org/10.1175/1520-0469(1984)041%3C0863:LMOCEF%3E2.0.CO.

Ovtchinnikov, M., and Y. L. Kogan, 2000: An Investigation of Ice Production Mechanisms in Small Cumuliform Clouds Using a 3D Model with Explicit Microphysics. Part I: Model Description. *J. Atmos. Sci.*, **57**, 2989–3003, doi:10.1175/1520-0469(2000)057<2989:AIOIPM>2.0.CO;2. http://dx.doi.org/10.1175/1520-0469(2000)057%3C2989:AIOIPM%3E2.0.CO.

Pinsky, M., A. Khain, and M. Shapiro, 2001a: Collision Efficiency of Drops in a Wide Range of Reynolds Numbers: Effects of Pressure on Spectrum Evolution. *J. Atmos. Sci.*, **58**, 742–764, doi:10.1175/1520-0469(2001)058<0742:CEODIA>2.0.CO;2. https://doi.org/10.1175/1520-0469(2001)058%3C0742:CEODIA%3E2.0.CO.

Pinsky, M., A. Khain, M. Shapiro, M. Pinsky, A. Khain, and M. Shapiro, 2001b: Collision Efficiency of Drops in a Wide Range of Reynolds Numbers: Effects of Pressure on Spectrum Evolution. *J. Atmos. Sci.*, **58**, 742–764, doi:10.1175/1520-

0469(2001)058<0742:CEODIA>2.0.CO;2. http://journals.ametsoc.org/doi/abs/10.1175/1520-0469%282001%29058%3C0742%3ACEODIA%3E2.0.CO%3B2 (Accessed May 15, 2018).

Pinsky, M., A. Khain, and H. Krugliak, 2008: Collisions of Cloud Droplets in a Turbulent Flow. Part V: Application of Detailed Tables of Turbulent Collision Rate Enhancement to Simulation of Droplet Spectra Evolution. *J. Atmos. Sci.*, **65**, 357–374, doi:10.1175/2007JAS2358.1. https://doi.org/10.1175/2007JAS2358.1.

Rasmussen, E. N., and D. O. Blanchard, 1998a: A Baseline Climatology of Sounding-Derived Supercell andTornado Forecast Parameters. *Weather Forecast.*, **13**, 1148–1164, doi:10.1175/1520-0434(1998)013<1148:ABCOSD>2.0.CO;2. http://dx.doi.org/10.1175/1520-0434(1998)013%3C1148:ABCOSD%3E2.0.CO.

Rasmussen, E. N., and D. O. Blanchard, 1998b: A Baseline Climatology of Sounding-Derived Supercell andTornado Forecast Parameters. *Weather Forecast.*, **13**, 1148–1164, doi:10.1175/1520-0434(1998)013<1148:ABCOSD>2.0.CO;2. http://journals.ametsoc.org/doi/abs/10.1175/1520-0434%281998%29013%3C1148%3AABCOSD%3E2.0.CO%3B2 (Accessed August 2, 2018).

Rasmussen, R. M., I. Geresdi, G. Thompson, K. Manning, and E. Karplus, 2002: Freezing Drizzle Formation in Stably Stratified Layer Clouds: The Role of Radiative Cooling of Cloud Droplets, Cloud Condensation Nuclei, and Ice Initiation. *J. Atmos. Sci.*, **59**, 837–860, doi:10.1175/1520-0469(2002)059<0837:FDFISS>2.0.CO;2. http://dx.doi.org/10.1175/1520-0469(2002)059%3C0837:FDFISS%3E2.0.CO.

Rogers, E., T. Black, B. Ferrier, Y. Lin, D. Parrish, and G. DiMego, 2002: Changes to the NCEP Meso Eta Analysis and Forecast System: Increase in resolution, new cloud microphysics, modified precipitation assimilation, modified 3DVAR analysis. http://www.emc.ncep.noaa.gov/mmb/mmbpll/eta12tpb/.

Romps, D. M., 2017: Exact Expression for the Lifting Condensation Level. *J. Atmos. Sci.*, **74**, 3891–3900, doi:10.1175/JAS-D-17-0102.1. http://journals.ametsoc.org/doi/10.1175/JAS-D-17-0102.1 (Accessed August 6, 2018).

Rotunno, R., J. B. Klemp, and M. L. Weisman, 1988: A Theory for Strong, Long-Lived Squall Lines. *J. Atmos. Sci.*, **45**, 463–485, doi:10.1175/1520-0469(1988)045<0463:ATFSLL>2.0.CO;2. http://journals.ametsoc.org/doi/abs/10.1175/1520-0469%281988%29045%3C0463%3AATFSLL%3E2.0.CO%3B2 (Accessed September 11, 2018).

Saleeby, S. M., and W. R. Cotton, 2004: A Large-Droplet Mode and Prognostic Number Concentration of Cloud Droplets in the Colorado State University Regional Atmospheric Modeling System (RAMS). Part I: Module Descriptions and Supercell Test Simulations. *J. Appl. Meteorol.*, **43**, 182–195, doi:10.1175/1520-

0450(2004)043<0182:ALMAPN>2.0.CO;2. http://dx.doi.org/10.1175/1520-0450(2004)043%3C0182:ALMAPN%3E2.0.CO.

——, and ——, 2008: A Binned Approach to Cloud-Droplet Riming Implemented in a Bulk Microphysics Model. *J. Appl. Meteorol. Climatol.*, **47**, 694–703, doi:10.1175/2007JAMC1664.1. http://dx.doi.org/10.1175/2007JAMC1664.1.

——, and S. C. van den Heever, 2013: Developments in the CSU-RAMS Aerosol Model: Emissions, Nucleation, Regeneration, Deposition, and Radiation. *J. Appl. Meteorol. Climatol.*, **52**, 2601–2622, doi:10.1175/JAMC-D-12-0312.1. http://dx.doi.org/10.1175/JAMC-D-12-0312.1.

Schlamp, R. J., S. N. Grover, H. R. Pruppacher, and A. E. Hamielec, 1976: A Numerical Investigation of the Effect of Electric Charges and Vertical External Electric Fields on the Collision Efficiency of Cloud Drops. *J. Atmos. Sci.*, **33**, 1747–1755, doi:10.1175/1520-0469(1976)033<1747:ANIOTE>2.0.CO;2. https://doi.org/10.1175/1520-0469(1976)033%3C1747:ANIOTE%3E2.0.CO.

Schumacher, R. S., 2009: Mechanisms for Quasi-Stationary Behavior in Simulated Heavy-Rain-Producing Convective Systems. *J. Atmos. Sci.*, **66**, 1543–1568, doi:10.1175/2008JAS2856.1. http://dx.doi.org/10.1175/2008JAS2856.1.

Seifert, A., 2008: On the Parameterization of Evaporation of Raindrops as Simulated by a One-Dimensional Rainshaft Model. *J. Atmos. Sci.*, **65**, 3608–3619, doi:10.1175/2008JAS2586.1. https://doi.org/10.1175/2008JAS2586.1.

——, and K. D. Beheng, 2001: A double-moment parameterization for simulating autoconversion, accretion and selfcollection. *Atmos. Res.*, **59**–**60**, 265–281, doi:10.1016/S0169-8095(01)00126-0. https://www.sciencedirect.com/science/article/pii/S0169809501001260 (Accessed July 17, 2018).

Shafrir, U., and T. Gal-Chen, 1971: A Numerical Study of Collision Efficiencies and Coalescence Parameters for Droplet Pairs with Radii up to 300 Microns. *J. Atmos. Sci.*, **28**, 741–751, doi:10.1175/1520-0469(1971)028<0741:ANSOCE>2.0.CO;2. https://doi.org/10.1175/1520-0469(1971)028%3C0741:ANSOCE%3E2.0.CO.

Simmons, K. M., and D. Sutter, 2005: WSR-88D Radar, Tornado Warnings, and Tornado Casualties. *Weather Forecast.*, **20**, 301–310, doi:10.1175/WAF857.1. http://journals.ametsoc.org/doi/abs/10.1175/WAF857.1 (Accessed September 5, 2018).

——, and ——, 2008: Tornado Warnings, Lead Times, and Tornado Casualties: An Empirical Investigation. *Weather Forecast.*, **23**, 246–258, doi:10.1175/2007WAF2006027.1. http://journals.ametsoc.org/doi/abs/10.1175/2007WAF2006027.1 (Accessed August 7, 2018).

Simmons, K. M., D. Sutter, and R. Pielke, 2013: Normalized tornado damage in the United States: 1950–2011. *Environ. Hazards*, **12**, 132–147, doi:10.1080/17477891.2012.738642.

https://doi.org/10.1080/17477891.2012.738642.

Smith, J. A., M. L. Baeck, Y. Zhang, and C. A. . Doswell, 2001: Extreme Rainfall and Flooding from Supercell Thunderstorms. *J. Hydrometeorol.*, **2**, 469–489, doi:10.1175/1525-7541(2001)002<0469:ERAFFS>2.0.CO;2. http://journals.ametsoc.org/doi/abs/10.1175/1525-7541%282001%29002%3C0469%3AERAFFS%3E2.0.CO%3B2 (Accessed September 6, 2018).

Snook, N., and M. Xue, 2008: Effects of microphysical drop size distribution on tornadogenesis in supercell thunderstorms. *Geophys. Res. Lett.*, **35**, L24803, doi:10.1029/2008GL035866. http://doi.wiley.com/10.1029/2008GL035866 (Accessed January 5, 2016).

Takuro, M., and T. Toshihiko, 2015: Evaluation of autoconversion schemes in a single model framework with satellite observations. *J. Geophys. Res. Atmos.*, **120**, 9570–9590, doi:10.1002/2015JD023818. https://doi.org/10.1002/2015JD023818.

Thompson, G., R. M. Rasmussen, and K. Manning, 2004: Explicit Forecasts of Winter Precipitation Using an Improved Bulk Microphysics Scheme. Part I: Description and Sensitivity Analysis. *Mon. Weather Rev.*, **132**, 519–542, doi:10.1175/1520-0493(2004)132<0519:EFOWPU>2.0.CO;2. http://dx.doi.org/10.1175/1520-0493(2004)132%3C0519:EFOWPU%3E2.0.CO.

——, P. R. Field, R. M. Rasmussen, and W. D. Hall, 2008: Explicit Forecasts of Winter Precipitation Using an Improved Bulk Microphysics Scheme. Part II: Implementation of a New Snow Parameterization. *Mon. Weather Rev.*, **136**, 5095–5115, doi:10.1175/2008MWR2387.1. http://dx.doi.org/10.1175/2008MWR2387.1.

Thompson, R. L., R. Edwards, and J. A. Hart, 2002: Evaluation and Interpretation of the Supercell Composite and Significant Tornado Parameters at the Storm Prediction Center. *Conference on Severe Local Storms*, J3.2 https://ams.confex.com/ams/SLS_WAF_NWP/techprogram/paper_46942.htm.

——, ——, ——, K. L. Elmore, and P. Markowski, 2003: Close Proximity Soundings within Supercell Environments Obtained from the Rapid Update Cycle. *Weather Forecast.*, **18**, 1243–1261, doi:10.1175/1520-0434(2003)018<1243:CPSWSE>2.0.CO;2. http://journals.ametsoc.org/doi/abs/10.1175/1520-0434%282003%29018%3C1243%3ACPSWSE%3E2.0.CO%3B2 (Accessed August 23, 2018).

Trapp, R. J., 1999: Observations of Nontornadic Low-Level Mesocyclones and Attendant Tornadogenesis Failure during VORTEX. *Mon. Weather Rev.*, **127**, 1693–1705, doi:10.1175/1520-0493(1999)127<1693:OONLLM>2.0.CO;2. http://journals.ametsoc.org/doi/abs/10.1175/1520-0493%281999%29127%3C1693%3AOONLLM%3E2.0.CO%3B2 (Accessed August 7, 2018).

Tzivion (Tzitzvashvili), S., G. Feingold, and Z. Levin, 1987: An Efficient Numerical Solution to

the Stochastic Collection Equation. *J. Atmos. Sci.*, **44**, 3139–3149, doi:10.1175/1520-0469(1987)044<3139:AENSTT>2.0.CO;2. https://doi.org/10.1175/1520-0469(1987)044%3C3139:AENSTT%3E2.0.CO.

Uijlenhoet, R., M. Steiner, and J. A. Smith, 2003: Variability of Raindrop Size Distributions in a Squall Line and Implications for Radar Rainfall Estimation. *J. Hydrometeorol.*, **4**, 43–61, doi:10.1175/1525-7541(2003)004<0043:VORSDI>2.0.CO;2. http://dx.doi.org/10.1175/1525-7541(2003)004%3C0043:VORSDI%3E2.0.CO.

van den Heever, S. C., and W. R. Cotton, 2004: The impact of hail size on simulated supercell storms. *J. Atmos. Sci.*, **61**, 1596–1609.

Varble, A., and Coauthors, 2014: Evaluation of cloud-resolving and limited area model intercomparison simulations using TWP-ICE observations: 1. Deep convective updraft properties. *J. Geophys. Res. Atmos.*, **119**, 13,891-13,918, doi:10.1002/2013JD021371. http://doi.wiley.com/10.1002/2013JD021371 (Accessed July 17, 2018).

Wacker, U., and C. Lüpkes, 2009: On the selection of prognostic moments in parametrization schemes for drop sedimentation. *Tellus A*, **61**, 498–511, doi:10.1111/j.1600-0870.2009.00405.x. http://dx.doi.org/10.1111/j.1600-0870.2009.00405.x.

Wagner, T. J., W. F. Feltz, and S. A. Ackerman, 2008: The Temporal Evolution of Convective Indices in Storm-Producing Environments. *Weather Forecast.*, **23**, 786–794, doi:10.1175/2008WAF2007046.1. http://journals.ametsoc.org/doi/abs/10.1175/2008WAF2007046.1 (Accessed August 20, 2018).

Wakimoto, R. M., and H. Cai, 2000: Analysis of a Nontornadic Storm during VORTEX 95. *Mon. Weather Rev.*, **128**, 565–592, doi:10.1175/1520-0493(2000)128<0565:AOANSD>2.0.CO;2. http://journals.ametsoc.org/doi/abs/10.1175/1520-0493%282000%29128%3C0565%3AAOANSD%3E2.0.CO%3B2 (Accessed August 7, 2018).

Walko, R. L., W. R. Cotton, M. P. Meyers, and J. Y. Harrington, 1995: New RAMS cloud microphysics parameterization part I: the single-moment scheme. *Atmos. Res.*, **38**, 29–62.

Wang, L.-P., and W. W. Grabowski, 2009: The role of air turbulence in warm rain initiation. *Atmos. Sci. Lett.*, **10**, 1–8, doi:10.1002/asl.210. http://doi.wiley.com/10.1002/asl.210 (Accessed May 15, 2018).

Weisman, M. L., and J. B. Klemp, 1982: The Dependence of Numerically Simulated Convective Storms on Vertical Wind Shear and Buoyancy. *Mon. Weather Rev.*, **110**, 504–520, doi:10.1175/1520-0493(1982)110<0504:TDONSC>2.0.CO;2. http://dx.doi.org/10.1175/1520-0493(1982)110%253C0504:TDONSC%253E2.0.CO.

Weisman, M. L., and R. Rotunno, 2000: The Use of Vertical Wind Shear versus Helicity in Interpreting Supercell Dynamics. *J. Atmos. Sci.*, **57**, 1452–1472, doi:10.1175/1520-

0469(2000)057<1452:TUOVWS>2.0.CO;2. http://journals.ametsoc.org/doi/abs/10.1175/1520-0469%282000%29057%3C1452%3ATUOVWS%3E2.0.CO%3B2 (Accessed August 6, 2018).

Xue, Y., L.-P. Wang, W. W. Grabowski, Y. Xue, L.-P. Wang, and W. W. Grabowski, 2008: Growth of Cloud Droplets by Turbulent Collision–Coalescence. *J. Atmos. Sci.*, **65**, 331–356, doi:10.1175/2007JAS2406.1. http://journals.ametsoc.org/doi/abs/10.1175/2007JAS2406.1 (Accessed May 15, 2018).

Yuter, S. E., and R. A. Houze, 1997: Measurements of Raindrop Size Distributions over the Pacific Warm Pool and Implications for Z–R Relations. *J. Appl. Meteorol.*, **36**, 847–867, doi:10.1175/1520-0450(1997)036<0847:MORSDO>2.0.CO;2. http://dx.doi.org/10.1175/1520-0450(1997)036%3C0847:MORSDO%3E2.0.CO.

Zhang, G., J. Vivekanandan, and E. Brandes, 2001: A method for estimating rain rate and drop size distribution from polarimetric radar measurements. *IEEE Trans. Geosci. Remote Sens.*, **39**, 830–841, doi:10.1109/36.917906. http://ieeexplore.ieee.org/document/917906/ (Accessed July 23, 2018).